

Structure & Kinematics of Early-Type Galaxies from Integral-Field Spectroscopy

Michele Cappellari

Sub-department of Astrophysics, Department of Physics, University of Oxford,
Denys Wilkinson Building, Keble Road, Oxford OX1 3RH

Annu. Rev. Astron. Astrophys. 2016.
54:1–67

This article's doi:
[10.1146/annurev-astro-082214-122432](https://doi.org/10.1146/annurev-astro-082214-122432)

Copyright © 2016 by Annual Reviews.
All rights reserved

Keywords

galaxies: elliptical and lenticular, cD – galaxies: evolution – galaxies: formation – galaxies: structure – galaxies: kinematics and dynamics

Abstract

Observations of galaxy isophotes, long-slit kinematics and high-resolution photometry suggested a possible **dichotomy** between two distinct classes of E galaxies. But these methods are expensive for large galaxy samples. Instead, integral-field spectroscopic can efficiently recognize the shape, dynamics and stellar population of complete samples of early-type galaxies (ETGs). These studies showed that the two main classes, the fast and slow rotators, can be separated using stellar kinematics. We showed there is a dichotomy in the dynamics of the two classes. The slow rotators are weakly triaxial and dominate above $M_{\text{crit}} \approx 2 \times 10^{11} M_{\odot}$. Below M_{crit} , the structure of fast rotators parallels that of spiral galaxies. There is a smooth sequence along which, the metals content, the enhancement in α -elements, and the “weight” of the stellar initial mass function, all increase with the *central* mass density slope, or bulge mass fraction, while the molecular gas fraction correspondingly decreases. The properties of ETGs on galaxy scaling relations, and in particular the (M_*, R_e) diagram, and their dependence on environment, indicate two main independent channels for galaxy evolution. **Fast rotators** ETGs start as star forming disks and **evolve through a channel dominated by gas accretion, bulge growth and quenching.** While slow rotators assemble near the center of massive halos via intense star formation at high redshift, and remain as such for the rest of their evolution via a channel dominated by **gas poor mergers.** This is consistent with independent studies of the galaxies redshift evolution.

1. INTRODUCTION

Our knowledge of the structure of galaxies in general, and of early-type galaxies (ETGs: ellipticals Es and S0s) in particular, has evolved in parallel with the technological advances in the instrumentation used to study them. Galaxy photographic plates formed the basis of the classic and still widely popular galaxy morphological classification scheme by [Hubble \(1926\)](#). From the late 50s rotation curves were obtained from ionized gas emission in external spiral galaxies (e.g. [Burbidge et al. 1959](#)). This revealed flat rotation curves out to large radii ([Rubin & Ford 1970](#)), subsequently strengthened by radio determinations ([Bosma 1978](#)), indicating dark matter surrounding the galaxies (see [Courteau et al. 2014](#), for a review). Dark matter is one of the pillars of the current paradigm of how galaxies form ([White & Rees 1978; Blumenthal et al. 1984](#)).

E: Elliptical galaxy.
Displays elliptical
isophotes on the sky

S0: Has an outer
disk like spiral
galaxies but smooth
appearance, without
spiral arms

In the 70s long-slit spectrographs were used to measure stellar rotation in elliptical galaxies. This revealed that the massive Es tend to rotate slowly, while less massive ones and galaxy bulges appeared to rotate faster ([Section 3.5.1](#)). In the 80s photometry of Es using CCD detectors showed that faint ellipticals can have disky isophotes, suggesting the presence of stellar disks embedded in dominant stellar spheroids ([Section 2.3](#)). The *Hubble Space Telescope* (HST) in the 90s showed that the steepness of the inner galaxy profiles also relates to the other galaxy properties ([Section 2.4](#)). HST also revolutionized our understanding of the link between galaxies and BHs evolution (see [Kormendy & Ho 2013](#), for a review).

In parallel to detailed studies of nearby galaxies, deep multi-band photometric galaxy surveys (e.g. GOODS [Giavalisco et al. 2004](#) and COMSOS [Scoville et al. 2007](#)), and multiplexed spectroscopic surveys (e.g. DEEP2 [Newman et al. 2013b](#)) were delivered. These provided the ability to trace galaxy evolution back in time (see [Conselice 2014](#), for a review).

The present review focuses on the progress in our knowledge of the structure of ETGs, and of galaxies in general, brought by the next major technological advance: **integral-field spectroscopy (IFS)**. This brings the ability to obtain a spectrum at every position on a grid of sky coordinates covering the galaxy image. Effective IFS prototypes appeared on the scene in the 90s (e.g. [Bacon et al. 1995](#)), but it took a decade for them to reach maturity. IFS has recently become a standard asset on all major telescopes and an essential tool of astrophysics research.

IFS: Integral-field
spectroscopy

This review summarizes the status of our knowledge before another instrumental revolution. This is the time when the first generation of IFS surveys, which targeted one galaxy at a time ([SAURON de Zeeuw et al. 2002](#), [ATLAS^{3D} Cappellari et al. 2011a](#), [CALIFA Sánchez et al. 2012](#), [DiskMass Bershady et al. 2010](#)) have been completed and a new generation of multiplexed IFS surveys, which can observe multiple galaxies simultaneously, is starting ([SAMI Bryant et al. 2015](#) and [MaNGA Bundy et al. 2015](#) galaxy surveys).

2. STRUCTURE FROM PHOTOMETRY

This section gives a concise summary of the main findings on the structure of ETGs before the publication of the first large set of IFS kinematics for ETGs in [Emsellem et al. \(2004\)](#). Most early developments were based on photometry alone. Extensive reviews were written on the classification ([Sandage 1975, 2005](#)) and photometry ([Kormendy et al. 2009; Kormendy & Bender 2012; Graham 2013](#)) of ETGs. These include a summary of the historic developments. We will not duplicate that material here but rather refer the reader to those publications. We only mention the results and definitions which are essential to understand the findings from two-dimensional spectroscopy, which is the focus of this review.

2.1. Definition of early-type galaxy

The focus of this review are ETGs, although it will be clear in what follows that one cannot understand ETGs without linking their structure to the general galaxy population. ETGs can be broadly characterized by their old population, red colors, small amount of gas and dust, and lack of spiral arms. These characteristics however are not equivalent. In fact applying different selection criteria for ETGs leads to quite different sets of galaxies (Strateva et al. 2001; Conselice 2006; van den Bergh 2007; Bernardi et al. 2010).

Here we adopt the standard definition of ETGs, as consisting the galaxies in the handle of Hubble (1936) empirical tuning-fork diagram. In the *revised* Hubble classification system (Sandage 1961), the separation between ETGs and spiral galaxies is entirely based on the presence of spiral arms (or extended dust lanes for edge-on galaxies). This separation was adopted unchanged by de Vaucouleurs (1959, 1963) and in the very popular Third Reference Catalogue of Bright Galaxies (de Vaucouleurs et al. 1991, hereafter RC3). The same criterion was used in the RC3 follow-up HyperLeda (Paturel et al. 2003). This nearly universal definition of ETGs is also adopted in this review.

ETG: Early-Type Galaxy: E or S0. Defined by the lack of spiral arms in optical images

2.2. Global galaxy profiles

For a number of years elliptical galaxies were thought to be well described by the de Vaucouleurs (1948) $R^{1/4}$ profile. The work by Caon et al. (1993) discovered that the profiles of many Es require the more general parametrization proposed by Sersic (1968):

$$I(R) = I_e \exp \left\{ -b(n) \left[\left(\frac{R}{R_e} \right)^{1/n} - 1 \right] \right\}, \quad (1)$$

where $b(n) \approx 2n - 0.327$ (Capaccioli 1989). Most importantly, it was found that the Sersic index n , related to the galaxy concentration, increases with increasing total galaxy luminosity. This result was confirmed by a number of authors (e.g. D'Onofrio et al. 1994; Bertin et al. 2002; Graham & Guzmán 2003; Ferrarese et al. 2006; Kormendy et al. 2009).

Sersic index n :
Increases with the galaxy concentration

The reported correlations were interpreted as due to a systematic change in the intrinsic properties of elliptical galaxies with luminosity. However it can also be partially explained by a systematic variation in the fraction of hidden disks in ellipticals. Most likely both effects play a role. In fact the Sersic index of bulges of spiral galaxies and S0s tends to be different from that of massive E (e.g. Kormendy et al. 2009; Krajnović et al. 2013a) and systematic variations in the Sersic index of spiral bulges also exist (Andredakis et al. 1995).

2.3. Isophotal shape

The shape of Es isophotes is quantified by finding the best-fitting ellipse, which provides a good first-order approximation, and then measuring the deviations from that ellipse. In the standard algorithm (Carter 1978; Jedrzejewski 1987; Bender et al. 1988; Franx et al. 1989; Peletier et al. 1990), the galaxy surface brightness, sampled along the ellipse, is fitted by the truncated Fourier expansion via linear least squares minimization

$$\Sigma(\psi) = \Sigma_0 + A_1 \sin(\psi) + B_1 \cos(\psi) + A_2 \sin(2\psi) + B_2 \cos(2\psi), \quad (2)$$

a_4 : Isophotal shape parameter. $a_4 > 0$ is “boxy” and $a_4 < 0$ is “disky”

where ψ is the eccentric anomaly, so that the angles are equally spaced when the ellipse is projected onto a circle. The best-fitting ellipse is *defined* as the one for which A_1, B_1, A_2, B_2

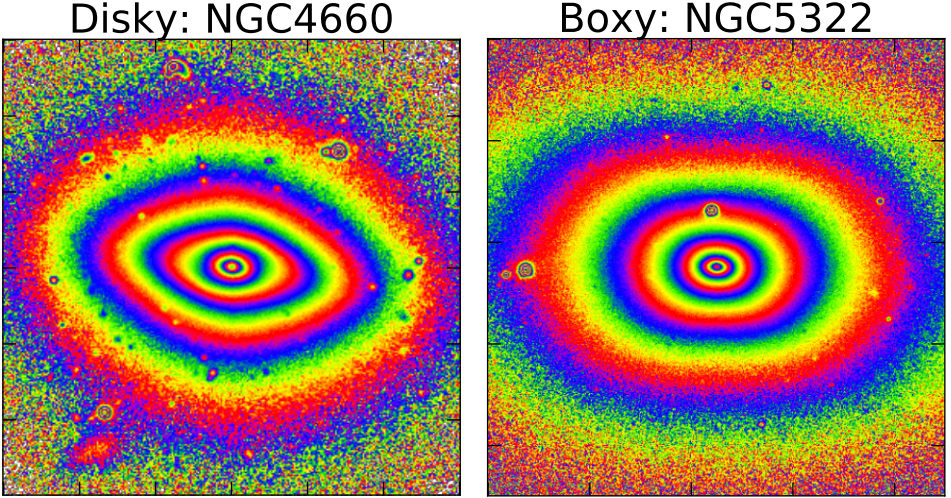


Figure 1

Disky versus boxy isophotes. *Left:* NGC 4660 has disky isophotes with $a_4 \approx 3\%$. *Right:* NGC 5322 has boxy isophotes with $a_4 \approx -1\%$. The photometry is taken from the SDSS. These galaxies were chosen as representative of the two classes in Bender et al. (1988).

are zero within numerical accuracy. Once the best-fitting ellipse has been determined, the surface brightness along that ellipse is parametrized by the next higher term in the Fourier expansion:

$$\Sigma(\psi) = \Sigma_0 + A_3 \sin(3\psi) + B_3 \cos(3\psi) + A_4 \sin(4\psi) + B_4 \cos(4\psi), \quad (3)$$

When the profile is properly sampled, the higher terms are mathematically orthogonal to the lower order ones. The amplitude of the axially-symmetric fourth Fourier coefficient $a_4 \equiv \sqrt{A_4^2 + B_4^2}$ measures whether an isophote is “boxy” ($a_4 > 0$) or “disky” ($a_4 < 0$; Figure 1). For physical interpretation, the quantity a_4 is typically divided by $(a d\Sigma / da)$, where a is the ellipse semi-major axis, in such a way that a_4 represents fractional deviations of the isophote from the best fitting ellipse.

These studies led to the discovery that disky Es appeared to rotate faster than non-disky or boxy Es (Bender 1988). Moreover radio-loud E were found to only be present in E without disky isophotes, showing that isophotal shape was an intrinsic parameter in galaxy structure (Bender et al. 1989). Ultimately, the realization of the important connection of isophotal shape and other global galaxy properties led to the proposal of a new classification scheme for Es (Kormendy & Bender 1996).

Disky elliptical E(d):
Intermediate between E and S0. The disk dominates the central regions, while the spheroid dominates at large radii

2.4. Nuclear galaxy profiles

The launch of the *Hubble Space Telescope* (HST) in 1990 revolutionized the study of inner profiles in Es by firmly establishing that the centers of Es do not possess flat “cores” (Crane et al. 1993). Additionally it was found that the profiles of Es could be broadly separated into two classes. The “core galaxies” showed clear breaks in the surface brightness, with a steeper outer profile followed by a more shallow inner one. While the “power-law galaxies” showed modest changes in profile slope (Figure 2; Ferrarese et al. 1994; Lauer et al. 1995).

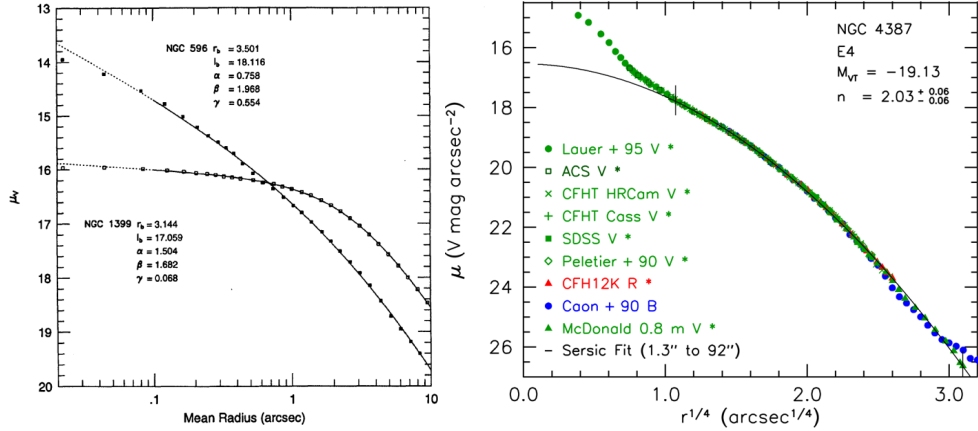


Figure 2

Nuclear profiles of ETGs. *Left:* The break in the surface brightness profile of a core galaxy is contrasted to the smooth steep rise of a power-law one (from Lauer et al. 1995). Both are fitted by Equation 4; *Right:* “extra light” in the inner surface brightness profile, with respect to a Sersic profile fit. This figure is taken from Kormendy et al. (2009), where these are interpreted as the extra light components that are produced by gas accretions or mergers, when cold gas dissipates and falls to the center producing a starburst.

A popular parametrization which was used to quantify the surface brightness profile shapes is the following double power-law (informally dubbed “Nuker law” by its proposers Lauer et al. 1995)

$$\Sigma(R) = \Sigma_b \left(\frac{R_b}{R} \right)^\gamma \left[\frac{1}{2} + \frac{1}{2} \left(\frac{R}{R_b} \right)^\alpha \right]^{(\gamma-\beta)/\alpha}, \quad (4)$$

where γ and β represent the (positive) asymptotic slope for radii respectively smaller and larger than the break radius R_b , where the surface brightness is Σ_b , while α determines the sharpness of the transition. From this relation the slope γ' is typically determined as the analytic value inferred from Equation 4 at HST resolution limit $R_0 \approx 0''.1$. According to this definition, core galaxies are those with $\gamma' \leq 0.3$ (Lauer et al. 1995, 2007b).

Alternative ways of quantifying inner profiles is by measuring either “extra light” or a “deficit” with respect to a global Sersic fit to the outer profile (e.g. Ferrarese et al. 2006; Kormendy et al. 2009), or using the “Core-Sersic” parametrization (Graham et al. 2003; Trujillo et al. 2004b). Reassuringly, the different profile classifications agree with each other with good accuracy (Krajnović et al. 2013b).

Some studies have emphasized a bi-modality, or dichotomy, in the distribution of the profile slopes within the general galaxy population (Lauer et al. 1995; Byun et al. 1996; Lauer et al. 2005, 2007b), while others find a smooth continuity (Carollo et al. 1997; Ferrarese et al. 2006; Côté et al. 2007). However, the key and remarkable result on which all studies agree is that the inner slope is closely related to the global galaxy properties measured spatial scales more than one order of magnitude larger (Faber et al. 1997; Lauer et al. 2005, 2007a; Ferrarese et al. 2006; Kormendy et al. 2009). This shows that nuclear slopes provide key physical insight on galaxy structure.

ELLIPTICALS DICHOTOMY BEFORE INTEGRAL-FIELD SPECTROSCOPY

To define our knowledge of the structure of ETGs before the advent of IFS, we consider papers published before the two companion **SAURON** papers introducing a *kinematic* classification (Emsellem et al. 2007; Cappellari et al. 2007). Key was the recognition of two classes, and possibly a dichotomy, among Es:

Giant Ellipticals ($M_V \lesssim -21.5$): (i) Have Sersic function outer profiles with $n \gtrsim 4$ (Caon et al. 1993); (ii) have cores in their nuclear profiles (Ferrarese et al. 1994; Lauer et al. 1995); (iii) rotate slowly (Illingworth 1977); (iv) are anisotropic and triaxial (Binney 1978); (v) tend to be rounder (Tremblay & Merritt 1996); (vi) can have boxy isophotes (Bender 1988); (vii) contain X-ray emitting gas (Bender et al. 1989); (viii) have old and α -elements enhanced stellar population (Thomas et al. 2005).

Normal-luminosity Ellipticals ($M_V \gtrsim -21.5$): (i) Have Sersic profiles with $n \lesssim 3$ (Graham & Guzmán 2003); (ii) are core-less (Faber et al. 1997); (iii) rotate rapidly (Davies et al. 1983); (iv) are nearly isotropic and oblate (Kormendy & Bender 1996); (v) can be quite flat; (vi) can have disky isophotes; (vii) rarely contain X-ray gas; (viii) can have young population and are not α enhanced.

The physical relevance of this possible dichotomy was summarized in Kormendy & Bender (1996), who proposed a revision to Hubble's classification of Es based on isophotal shapes, and by Faber et al. (1997); but see Ferrarese et al. (2006) for a different view. More recent, post-IFS, reviews of the dichotomy are given in Kormendy & Bender (2012); Kormendy (2016).

3. STRUCTURE FROM KINEMATICS

3.1. Visual classification of kinematic maps

The photometric approaches to recognize different types of Es, described in Section 2, suffer from two limitations: (i) measuring nuclear profiles require sub-arcsec spatial resolution; (ii) deviations from elliptical isophotes are only visible near edge-on orientations. This prevents the applicability of either technique to the large galaxy samples at significant distances.

A solution to both limitations is provided by IFS. In fact IFS observations of the stellar kinematics provide the long-sought ability to recognize the presence of stellar disks at virtually any inclination. This is illustrated in Figure 3, which predicts, using dynamical models (Cappellari 2008), how two nearly edge-on galaxies, the disky E (as classified by Bender et al. 1994) NGC 821 and the S0 galaxy NGC 5308, would appear when seen close to face on. The justification for the adopted models will be given in Section 3.4.3. The plot shows that both the centrally concentrated disk of a disky E, and the extended disk of an S0 galaxy, produce clear observable signatures in the kinematics at nearly all inclinations. In both cases the velocity fields display extended ordered rotation, with the kinematic position angle PA_{kin} aligned with the photometric major axis PA_{phot} . In contrast, the measurable effects on the isophote shape are hidden in the noise for inclinations $i \lesssim 60^\circ$. This is quantified in figure 8 of Krajnović et al. (2013a), which shows that even the strong disk of an edge-on S0 galaxy produces nearly elliptical isophotes ($a_4/a_0 \lesssim 2\%$).

The earliest IFS observations of the stellar kinematics used a simple but very time-consuming *y*-scanning approach, where a long slit is moved across the field to map a two dimensional field of the nearest E, Centaurus A (Wilkinson et al. 1986). This was followed by proof-of-concept large-scale observations of the stellar kinematics of individual ETGs with real IFS units like the TIGER integral-field unit (Bacon et al. 1995) on the CFHT

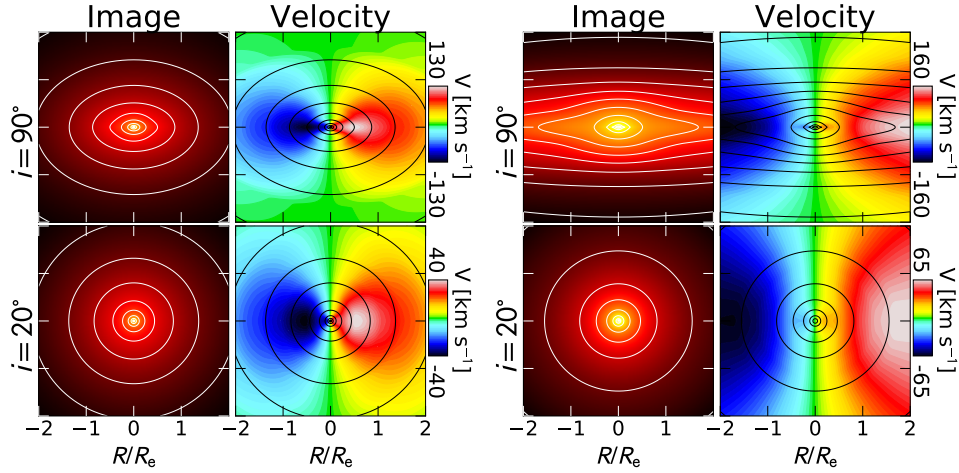


Figure 3

Recognizing face-on stellar disks. *Left:* photometric models for the disk E galaxy NGC 821, projected at two inclinations. The rainbow-colored panels show the corresponding stellar velocity predicted by the models. *Right:* as in the left plot, for the S0 galaxy NGC 5308. The presence of a disk can be visually recognized from the kinematics even near face-on inclination, while the photometric evidence disappears below $i \lesssim 60^\circ$. The input MGE surface brightness was taken from Cappellari et al. (2006) and Scott et al. (2009) respectively, while the adopted model parameters from Cappellari (2008). Note the different behavior of the velocity in the two types of galaxies. In the disk E the stellar disk dominates the surface brightness only out to $R \lesssim R_e$ and the velocity sharply drops beyond that radius. In the S0 the disk extends to the edge of the galaxy and the velocity is still rising at $R \gtrsim 2R_e$. This difference is encoded in the photometry and is not due to differences in the galaxies anisotropy, which is here assumed constant throughout the galaxy. Importantly, in both cases, the rotation is *not* limited to the disks, however the spheroids rotate more slowly due to their rounder shapes.

(Emsellem et al. 1996, 1999) or the MPFS integral-field unit (Sil’chenko et al. 1997) on the 6m telescope of the Special Astrophysical Observatory (Sil’chenko 1999).

A breakthrough came with the introduction of the **SAURON** (Bacon et al. 2001) IFS, due to the dramatic improvement of the instrument data quality with respect to previous prototypes. The **SAURON** survey (de Zeeuw et al. 2002) was the first project to map the two-dimensional stellar kinematics, ionized gas and stellar population of a significant sample of 48 nearby ETGs with total absolute magnitudes $M_B < -18$.

A striking feature which became immediately apparent at a simple visual inspection of the kinematic maps of the sample galaxies (Emsellem et al. 2004) was the qualitative separation between two classes of ETGs: on one side were galaxies consistent with the models of Figure 3, namely with what one would expect for disks seen at various inclinations (Figure 4e), while on the other side were galaxies clearly inconsistent with simple disks (Figure 4a–d). In two companion papers from the survey, this initial insight led to the proposal of a quantitative kinematic classification of ETGs, which is virtually independent on inclination effects (Emsellem et al. 2007; Cappellari et al. 2007).

The **SAURON** survey was followed by the ATLAS^{3D} project (Cappellari et al. 2011a), which, rather than being focused on IFS alone, was a multiwavelength survey combined with a theoretical modeling effort. It targeted a complete sample of 260 ETGs, extracted

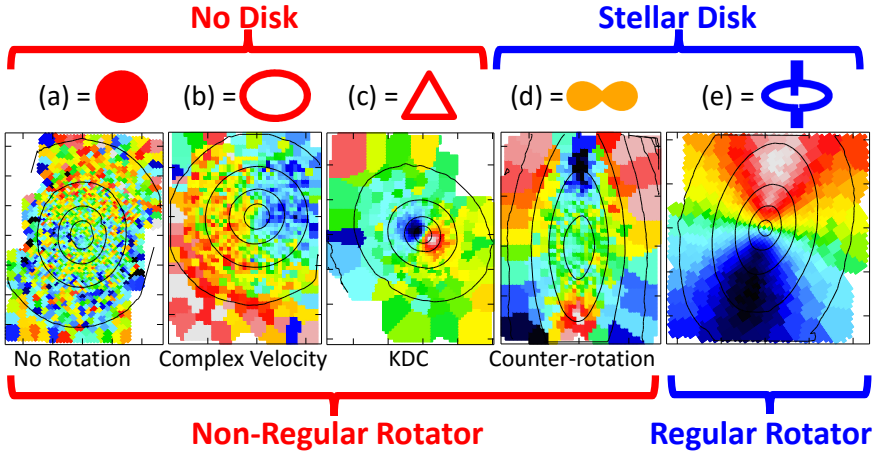


Figure 4

Morphological classification of stellar kinematic. The features in large samples of ETGs can all be qualitatively described by five classes. (a) No clearly detectable rotation (NGC 4374); (b) Clear but not regular rotation (NGC 4552); (c) kinematically distinct core (KDC; NGC 5813); (d) Counter rotating disks (NGC 4550); (e) Regular extended disk-like rotation (NGC 2974). The five classes were introduced by Krajnović et al. (2011). The Voronoi binned (Cappellari & Copin 2003) kinematics were taken from Emsellem et al. (2004). The symbols above the maps are used consistently throughout this review.

from a volume-limited sample of 871 galaxies brighter than $M_{K_s} < -21.5$, within $D \lesssim 42$ Mpc. The observations of the sample spanned from the radio to the millimeter and optical. The survey includes galaxies with a minimum stellar mass of $M_* \gtrsim 6 \times 10^9$.

ATLAS^{3D} confirmed the striking visual distinction between the kinematics of “regular rotator” or “non-regular rotator” (Krajnović et al. 2011). It additionally defined four subclasses of the non-regular class as illustrated in Figure 4. Non-regular rotators were found to (a) either not rotate at all, (b) to show clear but not bi-symmetric or irregular rotation, (c) to present a kinematically decoupled cores (KDCs, these features were discovered by Bender 1988; Jedrzejewski & Schechter 1988; Franx & Illingworth 1988; Franx et al. 1989) or (d) to indicate the presence of two counter-rotating disks (like the prototypical S0 NGC4550 discovered by Rubin et al. 1992; Rix et al. 1992).

LOSVD:

Line-of-sight velocity distribution

3.2. Generalizing photometry to kinematics maps

A galaxy image is only the 0th moment of the line-of-sight stellar velocity distribution (LOSVD). This suggests one may use an approach similar to that described in Section 2.3 to measure the shape of the higher moments of the LOSVD, and in particular the mean velocity field, which is the best measured quantity. Like in the photometric case, the approach will work as long as one can find a good zero-order description of the velocity along the best-fitting ellipse.

In the case of photometry, the zero-order approximation along a best-fitting ellipse is a constant. Krajnović et al. (2006, 2008) discovered that the velocity field of ETGs along the best-fitting ellipse, is approximated by a cosine law $V(\psi) = V_0 + B_1 \cos(\psi)$ with better than 2% accuracy. This is the same form one would expect if the kinematics was the one of an

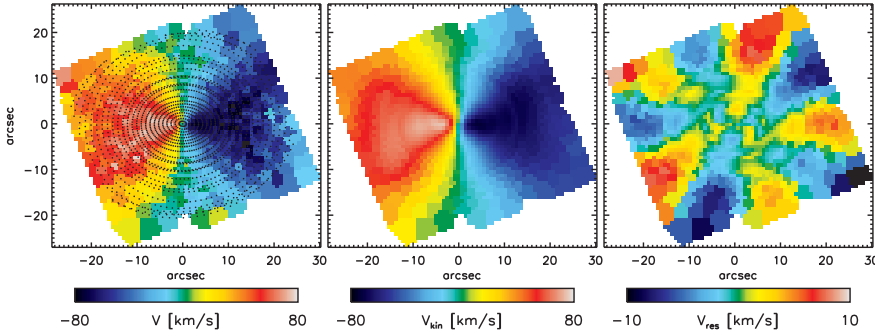


Figure 5

Applying kinemetry to stellar velocity maps. (a) Data with best-fitting ellipses overlaid. (b) Reconstructed velocity field adopting a pure cosine law along every ellipse. (c) Residuals between the observed and reconstructed velocity field. Note the 5-fold symmetry, which implies a significant k_5 term, indicative of a secondary kinematic component (from Krajnović et al. 2006).

infinitesimally thin disk. The fact that this law is able to describe the stellar kinematics of ETGs was thus unexpected. This finding motivated the extension of photometry to velocity fields (and other velocity moments) called KINEMETRY (Krajnović et al. 2006).

A popular, so called tilted-ring method, to perform ellipse fitting to gas velocity fields existed well before KINEMETRY and was implemented in the ROTCUR program (Begeman 1989). Schoenmakers et al. (1997) used ROTCUR to fit ellipses to the gas velocity field of spiral galaxies. The observed velocity along those ellipses was subsequently measured and interpreted using a Fourier expansion like in KINEMETRY. However, the key difference is that ROTCUR defines the best-fitting ellipse as the one which minimizes the squared deviations between the cosine law and the observed velocity samples along the ellipse, while KINEMETRY makes the low-order Fourier coefficient equal to zero. This makes KINEMETRY more robust and ensures that the low-order Fourier terms cannot affect the higher ones.

In practice, KINEMETRY was designed to be a direct generalization of the Fourier approach used for photometry. In close analogy to Equation 2 and Equation 3, KINEMETRY samples the galaxy velocity (or other odd moments of the velocity) along an ellipse using the truncated Fourier expansion

$$V(\psi) = V_0 + A_1 \sin(\psi) + B_1 \cos(\psi) + A_2 \sin(2\psi) + B_2 \cos(2\psi) + A_3 \sin(3\psi) + B_3 \cos(3\psi), \quad (5)$$

where ψ is the eccentric anomaly. Now the best-fitting ellipse is *defined* as the one for which A_1, A_2, B_2, A_3, B_3 are zero within numerical accuracy, while B_1 is allowed to be non-zero. Once the best-fitting ellipse has been determined, the velocity along that ellipse is again parametrized by the next higher term in the Fourier expansion

$$V(\psi) = V_0 + A_4 \sin(4\psi) + B_4 \cos(4\psi) + A_5 \sin(5\psi) + B_5 \cos(5\psi). \quad (6)$$

In this case the deviations of the ellipse from the pure $V(\psi) = V_0 + B_1 \cos(\psi)$ curve are quantified by the $k_5 \equiv \sqrt{A_5^2 + B_5^2}$ term. Similarly to the photometric a_4 parameter, which is sensitive to hidden disks, also k_5 is useful to determine the presence of multiple kinematic components. An application of the method to the E galaxy NGC 4473, which is known from dynamical modelling to contain two counter-rotating disks (Cappellari et al. 2007), is illustrated in Figure 5.

Kinemetry:
Generalizes
photometry to IFS
kinematics

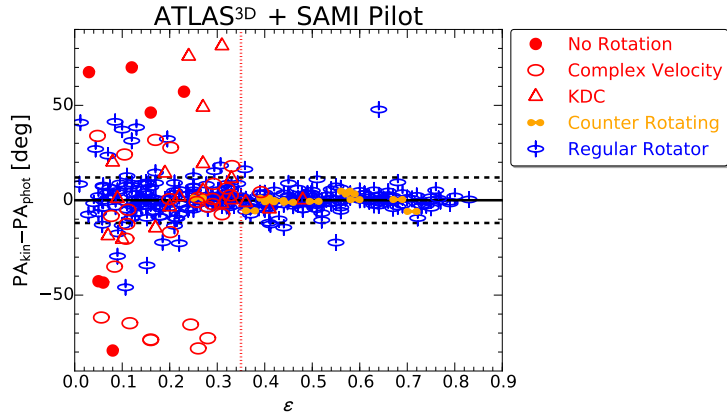


Figure 6

Kinematic misalignment. Difference between the photometric major axis PA_{phot} , measured around $R \approx 3R_e$, and the kinematic major axis PA_{kin} , measured around $R \approx R_e$. The plot includes data for 340 ETGs of which 260 were taken from Krajnović et al. (2011) and 80 from Fogarty et al. (2015). The meaning of the symbols is illustrated in Figure 4.

KINEMTRY was used to describe all velocity maps from the ATLAS^{3D} survey. Krajnović et al. (2011) found that the regular rotators are characterized by having residuals from the cosine law, quantified by the radially-averaged ratio $k_5/B_1 \lesssim 0.04$. This ratio measures the fractional amplitude of the 5th Fourier term, with respect to the peak velocity amplitude along the same ellipse.

3.3. Intrinsic shapes of early-type galaxies

Following the first study of the intrinsic shape of E galaxies by Hubble (1926), a large number of papers have investigated the intrinsic shape of E and S0 galaxies by statistical inversion of their apparent shape distribution (e.g. Sandage et al. 1970; Binney & de Vaucouleurs 1981; Fasano & Vio 1991; Lambas et al. 1992; Ryden 1992). An intrinsic limitation of these studies, is that the recovery of a generally triaxial shape distribution (a 2-dimensional function of the two axial ratios) from the distribution of the observed apparent ellipticity (a 1-dimensional function) is non unique. This remains true even when stellar kinematics is available (Franx et al. 1991).

Luckily, the vast majority of ETGs turns out to be much simpler than the purely dynamical consideration would permit them to be. This allows one to measure their shape, even in the presence of degeneracies. In fact IFS data showed that *all* regular rotators have kinematic axes PA_{kin} (measured for $R \approx R_e$) essentially aligned with the photometric one PA_{phot} (at much larger radii $R \approx 3R_e$) (Cappellari et al. 2007; Krajnović et al. 2011; Fogarty et al. 2015). This is illustrated in Figure 6 for a combined sample of 340 ETGs. The 1σ rms (biweight) scatter of 4° is almost at the level of the combined measurement errors of PA_{kin} and PA_{phot} . The few deviant objects appear to be either interacting systems or strongly barred.

The *only* way to observe such a tight alignment, for such a large sample of ETGs, is if regular rotators are axisymmetric out to their stellar halos, up to about $3R_e$. This is

PA_{kin}: Position angle of the axis where the projected velocities reach the maximum absolute values

PA_{phot}: Position angle of the axis along which the surface brightness reaches the maximum values

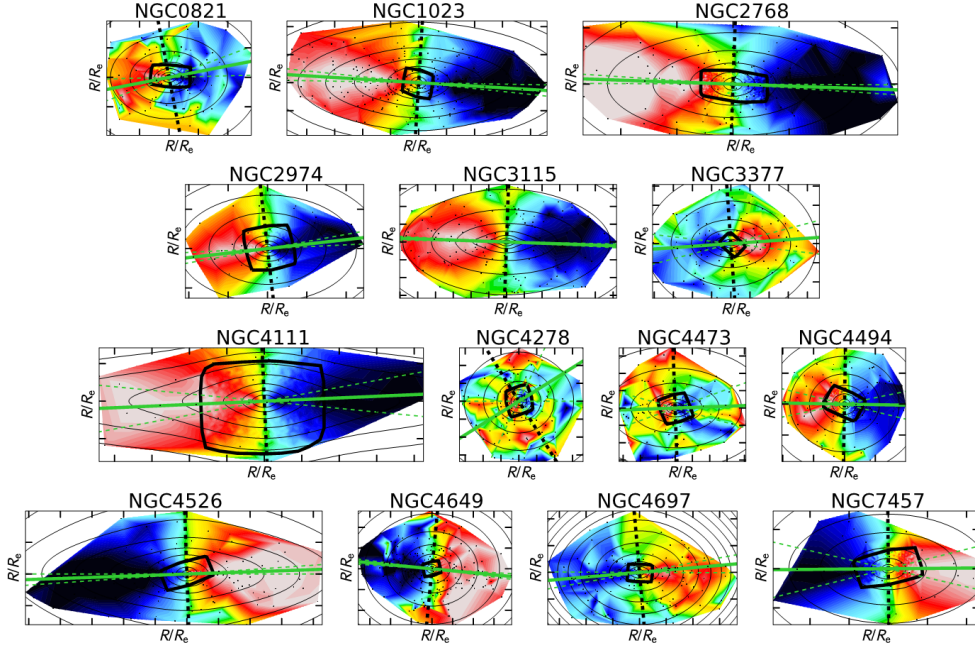


Figure 7

Kinematic misalignment at large radii. The maps show mean stellar velocity fields of regular rotators and one 2σ galaxy (NGC 4473) measured by the SLUGGS survey and taken from Arnold et al. (2014). The data are linearly interpolated from the measured positions, which are indicated by the small black dots. The SAURON IFS velocity at smaller radii are enclosed by the solid thick black line (from Emsellem et al. 2004 and Cappellari et al. 2011a). The fields are oriented in such a way that PA_{phot} , measured around $3R_e$ in Krajnović et al. (2011), is horizontal. The solid green line is the best fitting global kinematic PA_{kin} , fitted only to the SLUGGS data, and the dashed line indicate the measurement uncertainties. Isophotes of the galaxy surface brightness are overlaid, in 1 mag intervals. Tick marks are separated by $1R_e$, from Cappellari et al. (2011a).

because in triaxial systems: (i) the intrinsic symmetry axes need not be aligned with the projected photometric major axis (Contopoulos 1956; Stark 1977) and (ii) the intrinsic angular momentum need not be aligned with the intrinsic symmetry axes (e.g. Statler 1987). This implies that, in triaxial galaxies, kinematic misalignments are unavoidable, except in very special configurations. The lack of misalignment for a large sample then unambiguously implies axisymmetry for the whole class.

The alignment between the kinematics and photometry of regular rotators, out to a median radius of $4R_e$, can be seen directly, albeit for a much smaller sample, from the stellar kinematics obtained by the SLUGGS survey (Brodie et al. 2014). The data were presented in Arnold et al. (2014) and are reproduced in Figure 7 together with the SAURON kinematics in the central parts. The kinematics were oriented in such a way that the PA_{phot} from Krajnović et al. (2011) are horizontal. Overlaid are the kinematic axes, and errors, measured with the procedure `FIT_KINEMATIC_PA`¹ described in Krajnović et al. (2006). Although the

¹ Available from <http://purl.org/cappellari/software>

SLUGGS data are in some cases rather noisy, the plot shows that in all cases where it can be measured, the kinematic major axis agrees within the errors with the photometric one, consistently with the global axisymmetry of the stellar halos of regular rotators.

The ability of the stellar kinematics to separate the class of axisymmetric regular rotators from the rest, allows one to revisit the statistical inversion of the observed shape distribution. This is motivated by the fact that, once a family of objects has been proven to be axisymmetric, then the photometric statistical inversion procedure *does* provide a unique and well defined solution. This study of the intrinsic shape of regular rotators was performed using the volume-limited ATLAS^{3D} sample by [Weijmans et al. \(2014\)](#). They found that the intrinsic axial ratio of regular rotators, in their outer disks, can be described by a nearly Gaussian distribution with mean axial ratio $\langle q \rangle = 0.25$ and dispersion $\sigma_q = 0.14$. This distribution is consistent with that of spiral galaxies (e.g. [Lambas et al. 1992](#); [Padilla & Strauss 2008](#)). One should note that this flattening mainly refers to the outer parts where disks dominate, but ETGs have larger bulges than spirals as will be discussed later.

The shape inversion remains non unique for the non-regular rotators, which show evidence of kinematic misalignment, implying triaxiality. However the kinematic data show that the intrinsic ratio between the smallest and largest axis of the triaxial ellipsoid, measured around $3R_e$, must be $c/a \gtrsim 0.65$. This is demonstrated by the fact that no kinematic misalignment are observed for the 38 non-regular rotators with $\varepsilon \lesssim 0.35$ ([Figure 6](#)). Even ignoring the extra information provided by the misalignment, which is not always well defined for non-regular rotators, a stringent limit is placed by the fact that all non-regular rotators have $\varepsilon \lesssim 0.4$ (also see [Section 3.6.3](#)). The small ellipticity of slow rotating galaxies is also confirmed using VIMOS kinematic observations of 7 additional slow rotator BCGs ([Jimmy et al. 2013](#)), using the Mitchell Spectrograph (formerly VIRUS-P) for 11 more massive slow rotators ([Raskutti et al. 2014](#)). Overall, out of the 73 slow rotators observed so far, *all* are rounder than $\varepsilon \lesssim 0.4$. This shows that non-regular rotators as a class are quite close to spherical and only weakly triaxial.

3.4. Dynamical modeling of stellar kinematics

3.4.1. Techniques and degeneracies. A complementary way of quantifying the information content of kinematic maps is via dynamical modeling of the stellar kinematics. A key assumption of the models is that the galaxies are in a steady state. The models also generally assume simple spherical, axisymmetric or triaxial shapes. Under the steady state assumption, the galaxy dynamics is fully specified by (i) the six-dimensional stellar distribution function (DF), which describes the distribution of the positions and velocities of stars in the galaxy, and (ii) by the gravitational potential, or equivalently the total mass distribution, which may include the stellar contribution, as well as a dark matter halo and supermassive black hole. A recent review of this topic was given by [Courteau et al. \(2014\)](#). Here we focus on results specific to IFS observations.

Three major methods have been used in the past three decades: (i) The equations of stellar hydrodynamics, first applied to galaxies by [Jeans \(1922\)](#); (ii) The numerical orbit-superposition method by [Schwarzschild \(1979\)](#); and (iii) the made-to-measure N-body models by [Syer & Tremaine \(1996\)](#). The first has the advantage that it has predictive power and that one can compute reproducible results to numerical accuracy. While the latter two methods have the advantage of generality, which is required for unbiased results. However these two methods cannot make predictions, and depend on implementation details.

DF: Stellar distribution function. Describes the orbital distribution in a galaxy

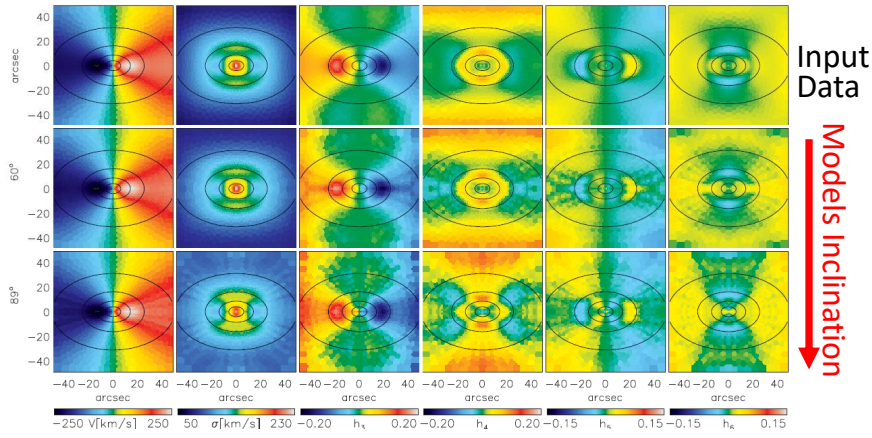


Figure 8

Inclination degeneracy. The top row shows the mean stellar velocity, the velocity dispersion σ and the higher Gauss-Hermite moments of the velocity, for the input simulated data, for an axisymmetric galaxy seen at an inclination $i = 60^\circ$. These data were fitted by Schwarzschild models at different inclinations. At every inclination the models surface brightness is constrained to agree with the input one. To eliminate the effect of the intrinsic degeneracy in the deprojection, the surface brightness is deprojected in such a way that at the correct inclination the intrinsic density is the same as the input one. Even in these idealized conditions the differences in the model fits at different inclinations are at the level of the systematic errors affecting real kinematic observations. (taken from [Krajnović et al. 2005](#))

The recovery of the DF and the mass distribution using only line-of-sight quantities, is an intrinsically degenerate and non-unique problem. This is because the DF is a function of the three isolating integrals of motion ([Jeans 1915](#)) and one cannot expect to uniquely constrain *both* the 3-dim DF and the 3-dim mass distribution using only a 3-dim observable, as provided by the LOSVD at every spatial location (e.g. [Valluri et al. 2004](#), section 3).

Moreover, already the deprojection of the stellar surface brightness into an intrinsic stellar luminosity density is known to be mathematically non unique, even when assuming axisymmetry, unless the galaxy is known to be edge-on ([Rybicki 1987](#)). This degeneracy increases rapidly at lower inclinations ([Gerhard & Binney 1996](#); [van den Bosch 1997](#); [Romanowsky & Kochanek 1997](#)) and represents a fundamental barrier to detailed models of external galaxies. Relaxing the axisymmetry assumption further changes the dimension of the problem, and vastly increase the room for degeneracies ([Gerhard 1996](#)), making the recovery of general triaxial stellar densities impossible without strong assumptions.

Empirical explorations of the model degeneracies using IFS data have revealed that in practice, even in an ideal case in which (i) one uses simulated noiseless 2-dim data, (ii) one artificially removes the deprojection degeneracy and (iii) one assumes there is no dark matter and the gravitational potential is produced by the stars alone, still, also a basic parameter like the galaxy inclination, or equivalently its shape, is virtually unconstrained by the IFS data ([Krajnović et al. 2005](#); [van den Bosch & van de Ven 2009](#); Figure 8). Tests on the ability of the models to constrain the mass profiles have also revealed ample room for degeneracies in the model parameters even with excellent data ([Gerhard et al. 1998](#); [de Lorenzi et al. 2009](#)).

3.4.2. Results from integral-field data using general models. With the previous caveats in mind, key results were obtained using dynamical models fitted to stellar kinematics. Schwarzschild (1979) models, generalized to fit kinematic data (Richstone & Tremaine 1988; Rix et al. 1997; van der Marel et al. 1998) have provided most of the mass determinations of supermassive black holes in galaxies (e.g., some examples from different groups are van der Marel et al. 1998; Gebhardt et al. 2000b; Cappellari et al. 2002; Valluri et al. 2005; McConnell et al. 2011; van den Bosch et al. 2012; Rusli et al. 2013). These measurements have driven much of our understanding of the connection between supermassive black holes and galaxy evolution. The important topic was reviewed by Kormendy & Ho (2013) and will not be addressed here.

Other significant results are the determination of stellar mass-to-light ratios and of total mass profiles. According to these studies, dark matter appears to play a minor role within $1R_e$ (Section 4.2.2), which implies that, at those radii, the shape of the total mass density is close to that of the luminous density (Section 4.2.3). Under this assumption, the availability of the first set of IFS data from the SAURON survey (de Zeeuw et al. 2002), opened up the possibility for a unique inversion of the datacube into the DF. This was attempted by Cappellari et al. (2007), using the axisymmetric Schwarzschild (1979) implementation, optimized for IFS data, described in Cappellari et al. (2006). The dynamical models provide the stellar mass orbiting along the half a million orbits which approximate the whole galaxy. To quantify this large amount of information, three anisotropy parameters were defined (Cappellari et al. 2007; Binney & Tremaine 2008, equation 4.265)

$$\beta_z \equiv 1 - \frac{\Pi_{zz}}{\Pi_{RR}}, \quad \gamma \equiv 1 - \frac{\Pi_{\phi\phi}}{\Pi_{RR}}, \quad \delta \equiv 1 - \frac{\Pi_{zz}}{\Pi_{xx}}, \quad (7)$$

where (R, z, ϕ) are the standard cylindrical coordinates, z coincides with the symmetry axis of an axisymmetric galaxy, and x is any direction orthogonal to it. Here

$$\Pi_{kk} = \int \nu \sigma_k^2 d^3x, \quad (8)$$

with σ_k the velocity dispersion along the direction k at a given location inside the galaxy and ν the stellar density. The numerical integral extends to the region covered by the IFS observations. β_z describes the global shape of the velocity dispersion tensor in the (v_R, v_z) plane. If the anisotropy is spatially constant then $\beta_z = 1 - (\sigma_z/\sigma_R)^2$. The anisotropy γ describes the global shape of the velocity dispersion tensor in a plane orthogonal to v_z . If the anisotropy is spatially constant then $\gamma = 1 - (\sigma_\phi/\sigma_R)^2$. For an isotropic system (spherical velocity ellipsoid) one has $\beta_z = \gamma = \delta = 0$. Integrating over the azimuthal angle one finds that the three anisotropy parameters are related by $\delta = (2\beta_z - \gamma)/(2 - \gamma)$. In the case $\gamma = 0$ the simple relation $\beta_z = \delta$ applies.

The anisotropy parameters β_z , γ and δ converge to zero in the spherical non-rotating limit, for symmetry. For this reason, to quantify the anisotropy of nearly spherical galaxies a complementary anisotropy parameter was defined, in spherical coordinates:

$$\beta_r \equiv 1 - \frac{\Pi_{tt}}{\Pi_{rr}} = 1 - \frac{\Pi_{\theta\theta} + \Pi_{\phi\phi}}{2\Pi_{rr}}, \quad (9)$$

where (r, θ, ϕ) are the standard spherical coordinates. In the spherical limit, assuming the galaxy is non rotating, $\Pi_{\theta\theta} = \Pi_{\phi\phi}$ by symmetry. The parameter is $\beta_r = 0$ for an isotropic galaxy and is positive (negative) when the luminosity-weighted average dispersion

along the radial direction is larger (smaller) than the average dispersion along any direction orthogonal to it.

The result of the calculation of the four anisotropy parameters for 25 galaxies from the SAURON sample consistent with axisymmetry, showed that *on average*: (i) regular rotators have significant anisotropy δ ; (ii) the velocity ellipsoid is *oblate* with $\delta \sim \beta_z$ and $\gamma \sim 0$; (iii) $\beta_z \gtrsim 0$ even though no limits are enforced by the models on this parameter (Cappellari et al. 2007). This picture was independently confirmed using long-slit kinematics of a different galaxy sample and a different modeling code (Thomas et al. 2009).

The two galaxies NGC 4550 and NGC 4473 stood out for a significant tangential anisotropy ($\gamma < 0$). In both cases the IFS data shows a characteristic and peculiar enhancement of the stellar velocity dispersion σ along the galaxy major axis, with two symmetric peaks in σ along the major axis, qualitatively suggesting the presence of counter-rotating disks (for NGC 4550 it confirms the result by Rubin et al. 1992 and Rix et al. 1992). This interpretation was quantitatively confirmed by the dynamical models which recovered two clearly distinct population of stars rotating in opposite direction (Cappellari et al. 2007). The strong tangential anisotropy is precisely what one would have expected given the fact that the two counter-rotating stellar disks strongly increase the random motions in the tangential direction. These two well-studied prototypes of counter-rotating disks motivated the definition of a more general class of qualitatively similar galaxies, which Krajnović et al. (2011) named 2σ galaxies, because of their distinctive double peaks in σ along the major axis. They were found to constitute 4% of the ATLAS^{3D} sample (Krajnović et al. 2011).

The situation is different for the rounder non-regular rotators. They were found to span a smaller range of anisotropies than the regular rotators and their anisotropy scatters around zero, implying that on average they are close to isotropic. They cannot be precisely so, given their triaxial shapes but, adopting either cylindrical or spherical coordinates, the global anisotropy parameters indicate deviations $\lesssim 10\%$ of their velocity ellipsoid from a sphere. This agrees with results obtained using long-slit kinematics of nearly round Es (Gerhard et al. 2001; Gebhardt et al. 2003).

An interesting class of non-regular rotators are those with central KDC. Detailed Schwarzschild dynamical models using SAURON data for NGC 4365 (van den Bosch et al. 2008) revealed that the KDC is not spatially distinct in terms of orbital distribution. The “apparent” KDC arises because of the superposition of two populations of counter-rotating large-scale tube orbits, with mean velocities canceling out over most of the field, except near the center. The large extent of the stellar orbits producing the KDC, is consistent with the observed homogeneity in the stellar population of the KDC in this galaxy (Davies et al. 2001), and of the large KDCs of non-regular rotators in general (McDermid et al. 2006). A similar example of Schwarzschild modeling of a KDC in the non-regular rotator NGC 5813 was presented by Krajnović et al. (2015) using very high-quality MUSE (Bacon et al. 2010) observations. The study confirmed the “apparent” nature of the KDC in this other non-regular rotator. The similarity in the density distribution of the two counter-rotating orbits, which is needed to produce the observed negligible mean stellar velocity outside the KDC, is reminiscent of the “Separatrix crossing” mechanism proposed by Evans & Collett (1994). Krajnović et al. (2015) summarizes possible KDCs formation mechanisms.

The anisotropy β_z , namely the z -flattening of the velocity ellipsoid, of regular rotators was found to be related to their intrinsic axial ratios $\varepsilon_{\text{intr}}$. This is illustrated in the left panel of Figure 9. Here the flattening is the intrinsic one, deprojected from the observed

KDC: Kinematically decoupled core

2σ galaxies:: Contain two counter-rotating stellar disks

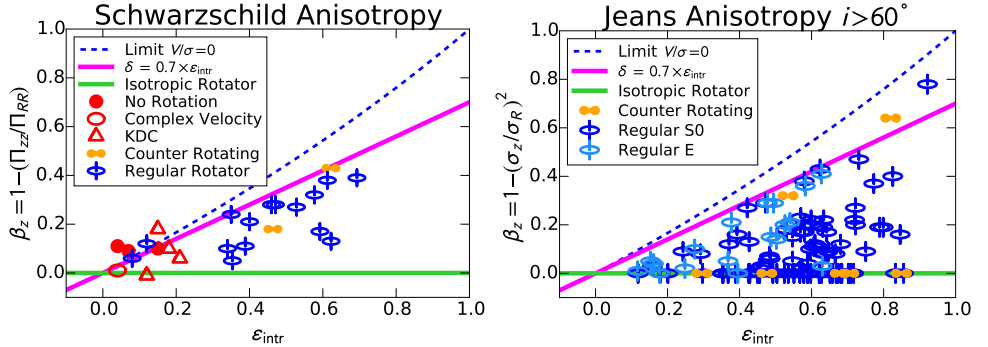


Figure 9

Anisotropy versus intrinsic flattening. *Left:* The anisotropy derived via Schwarzschild models is plotted against the deprojected intrinsic ellipticity of the galaxies around $1R_e$. Non-regular rotators tend to be close to isotropic in their central regions. While regular rotators span a range of anisotropies, but appear bounded by a relation of the form $\beta_z \approx 0.7 \times \epsilon_{\text{intr}}$ (magenta line). The green line indicates $\sigma_z = \sigma_R$, while the dashed line is the limit $\beta_z = 1 - 1/\Omega(e)$ (see Equation 15) set by the tensor virial equations for objects with oblate velocity ellipsoid. This plot was adapted from Cappellari et al. (2007). *Right:* As in the left panel, for the anisotropy determined via JAM models. Only galaxies with $i > 60^\circ$ were included to reduce the effect of the inclination-anisotropy degeneracy. The symbols are defined in Figure 4.

one ϵ within an isophote enclosing half of the total light using ($i = 90^\circ$ being edge-on)

$$\epsilon_{\text{intr}} = 1 - \sqrt{1 + \epsilon(\epsilon - 2) / \sin^2 i}. \quad (10)$$

Regular rotators are found to span a range of β_z at given ϵ_{intr} , with the range increasing with ϵ_{intr} . For an oblate velocity ellipsoid ($\sigma_\phi = \sigma_R$) the tensor virial theorem (Binney & Tremaine 2008) already sets an upper limit $\beta_z < 1 - 1/\Omega(e)$, corresponding to $V/\sigma = 0$ in Equation 14. However the observed values do not span the full space allowed by virial equilibrium, and in particular are found to lie approximately below the linear relation (Cappellari et al. 2007)

$$\delta \approx \beta_z = 0.7 \times \epsilon_{\text{intr}}. \quad (11)$$

In the next section we show that these results, obtained from detailed dynamical models of a small set of galaxies, are fully consistent with what one can infer, on a much larger sample of galaxies, using the very different approach provided by the Jeans (1922) equations.

3.4.3. Results from integral-field data using Jeans models. Motivated by the finding that the anisotropy of fast rotator ETGs is *on average* best approximated as a flattening of the velocity ellipsoid $\sigma_z < \sigma_R$, Cappellari (2008) developed an accurate and efficient method to solve the axisymmetric Jeans equations allowing for a cylindrically-aligned velocity ellipsoid with general axial ratios $\sigma_R \neq \sigma_z \neq \sigma_\phi$. As discussed in detail in the paper, the cylindrical alignment is only an approximation, as it cannot be accurately satisfied in real galaxies. This Jeans Anisotropic Modeling (JAM) formalism is an anisotropic (three-integral) generalization of the semi-isotropic (two-integral) formalism ($\sigma_R = \sigma_z$) presented in Emsellem et al. (1994). It uses the Multi-Gaussian Expansion (MGE; Emsellem et al. 1994; Cappellari 2002) to parametrize the observed galaxy surface brightness. The MGE allows for

an analytic deprojection of the observed surface brightness (Bendinelli 1991; Monnet et al. 1992). One can employ an arbitrary number of Gaussians to reproduce all features of a galaxy image. In particular one can describe in detail multiple photometric components, including bulges, disks, inner disks and general ellipticity variations.

The comparison between the JAM models and real state-of-the-art IFS observations of ETGs confirms the expectations from the Schwarzschild models. It shows that, assuming a constant-anisotropy, cylindrically-aligned velocity ellipsoid, one can “predict” the kinematics with remarkable accuracy. [Figure 10](#) shows that the large variety in the observed shapes of the velocity second moment $V_{\text{rms}} \equiv \sqrt{V^2 + \sigma^2}$ maps of fast rotator ETGs are properly captured by the simple JAM models. Once the photometry of the galaxies is given as input, the models are fully specified by the single physical parameter $\beta_z \equiv 1 - (\sigma_z/\sigma_R)^2$ and by the inclination, as well as by the overall mass scaling, which is parametrized via the total mass-to-light ratio (M/L). Moreover, the distribution of β_z for the regular rotators, as a function of the intrinsic ellipticity $\varepsilon_{\text{intr}}$, is consistent with the one observed from the Schwarzschild models. It shows that real galaxies have $\beta_z \lesssim 0.7 \times \varepsilon_{\text{intr}}$. The JAM models show that this trend is not due to anisotropic disks embedded in isotropic bulges, in fact the best fits to the kinematics are obtained with a constant anisotropy for both components.

Once the JAM models have been fitted to the V_{rms} , the intrinsic velocity second moment $\overline{v_\phi^2}$ in the tangential direction are uniquely defined by the given assumptions. However, to estimate the first velocity moment, the mean stellar velocity V , one needs to make an extra assumption about how the $\overline{v_\phi^2}$ splits into ordered and random motion, as defined by

$$\overline{v_\phi^2} = \overline{v_\phi}^2 + \sigma_\phi^2. \quad (12)$$

The JAM method allows for a general tangential anisotropy $\gamma = 1 - (\sigma_\phi/\sigma_R)^2$, however this generality is not actually needed to describe the kinematics of real galaxies, at least within about $1R_e$, where good data have been obtained for many galaxies. In fact, if one makes the simplest assumption of an oblate velocity ellipsoid $\gamma = 0$ (or $\sigma_\phi = \sigma_R$), the shape of the mean stellar velocity field can also be quite accurately predicted, without the need to invoke extra parameters ([Figure 10](#)).

A remarkable finding is that, if one takes as reference the mean projected velocity field $V(\sigma_\phi = \sigma_R)$ predicted by a JAM model with a perfectly oblate velocity ellipsoid, the overall scaling κ required to best fit the observed velocity V_{obs} is close to $\kappa \approx 1$ with an observed rms scatter of only 7% ([Figure 11](#)). This already small observed scatter also includes the effect of measurement errors in β_z , the inclination and M/L , which are independently fitted to the V_{rms} and used as input to predict the $V(\sigma_\phi = \sigma_R)$. This result confirms that an oblate velocity ellipsoid provides a good approximation to the observed galaxy dynamics within $1R_e$.

The class of counter-rotating disks ([Figure 4d](#)) necessarily cannot be described by models with oblate velocity dispersion tensor. This is because counter-rotating stars produce strong tangential anisotropy. However, it turns out that these ETGs have similar dynamics to the other regular rotators, once the counter-rotation is taken into account. This is illustrated in [Figure 12](#), where the JAM models are used to describe their kinematics. One can see that their V_{rms} is still reasonably well predicted by the models, once the photometry is given, with a similar range of β_z anisotropy.

In this case however, to fit the velocities, the sense of rotation of the stars enclosed within some of the MGE Gaussians was reversed, by allowing κ to have different signs for different Gaussians, while still being relatively close to unity. The stellar velocity dispersion

MGE:

Multi-Gaussian expansion

JAM: Jeans anisotropic modeling

 κ : Ratio

$V_{\text{obs}}/V(\sigma_\phi = \sigma_R)$ of the observed velocities and a model with oblate velocity ellipsoid

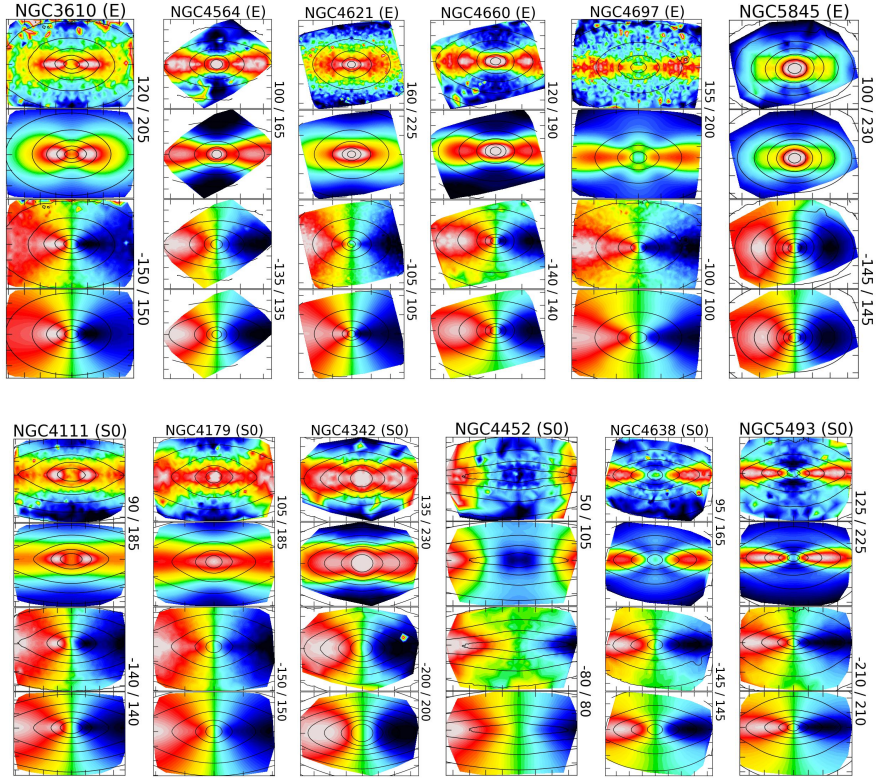


Figure 10

JAM models of regular rotators. The top rows show six Es, while the bottom one six S0s (from RC3). As expected for regular rotators, most Es have disk-like isophotes and are better morphologically classified as E(d). In each plot, the top panel shows the symmetrized SAURON stellar $V_{\text{rms}} \equiv \sqrt{V^2 + \sigma^2}$, the second panel is the best fitting JAM model to the V_{rms} , the third panel is the SAURON mean stellar velocity V and the bottom panel is the best fit to V obtained by keeping the best fitting anisotropy β_z , inclination i and M/L from the previous fit to the V_{rms} . Only an overall scaling of V is done here. The SAURON data come from [Emsellem et al. \(2004\)](#) or [Cappellari et al. \(2011a\)](#). The MGE surface brightness is from [Scott et al. \(2013a\)](#). Once an accurate description of the surface brightness is given, the observed shape of the kinematics of each galaxy can be predicted with remarkable accuracy by varying the single physical parameter β_z , and by choosing an inclination. This illustrates the homogeneity in the dynamics of the regular rotators family. Given that these models assume a mass distribution following the light, the good predictive power suggests this assumption should also be nearly correct.

was then given by $\sigma = \sqrt{V_{\text{rms}}^2 - V^2}$. Using this simple approach one can naturally describe the observations of the counter-rotating disks. This shows that these 2σ galaxies form a physically homogeneous family with the rest regular rotators.

However, not all galaxies are well described by JAM models with oblate velocity ellipsoid. This is only true for the ETGs with evidence for stellar disks (Figure 4d–e). The situation is dramatically different for the non-regular rotators (Figure 4a–c). The V_{rms} of these objects can generally still be well approximated by JAM, however the shape of the predicted $V(\sigma_\phi = \sigma_R)$ is, even qualitatively, *very* different from the observed velocity field.

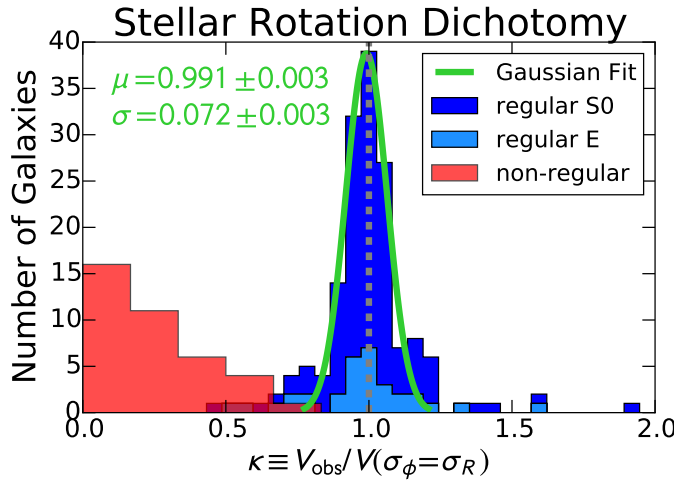


Figure 11

Stellar rotation dichotomy. Histogram of the ratio κ between the observed velocity V_{obs} and the velocity $V(\sigma_\phi = \sigma_R)$ predicted by a JAM model with an oblate velocity ellipsoid. The values are extracted from models (A) of Cappellari et al. (2013b). More specifically this ratio is determined by linearly fitting the full JAM velocity field to the observed one. The green line is a Gaussian fit to the histogram, for the regular rotators only. The distribution peaks with high accuracy at the value $\kappa \approx 1$, which corresponds to an oblate velocity ellipsoid on average. No statistically significant difference is observed (via K-S test), in the distribution of the E and S0 regular rotators. However the non-regular rotators have a completely different distribution, which peaks at $k \approx 0$, with a broad tail. The regular and non-regular rotators are well separated in this diagram around $k \approx 0.65$, the transition region being due to counter-rotation in disk galaxies. Only non-regular rotators have $\kappa \lesssim 0.5$ and only regular ones have $\kappa \gtrsim 0.75$. This diagram demonstrates a clean dichotomy, rather than a continuity between the two classes of ETGs.

A simple way to quantify the difference between the dynamics of the regular versus the non-regular rotators is to look at the distribution of their measured κ parameters (Figure 11). This shows that, while the regular rotators show a nearly Gaussian distribution with average $\kappa \approx 1$, the non-regular rotators are clearly distinct. Importantly, the kinematics shows a real dichotomy, not a smooth transition, between these two classes of galaxies, suggesting that they must follow different formation channels in their evolution.

3.5. Understanding the $(V/\sigma, \varepsilon)$ diagram

3.5.1. Before integral-field kinematics. Before observations of the stellar kinematics of ETGs became possible, these objects were thought to constitute a class of homogeneous systems, with an isotropic velocity dispersion tensor. A revolution was started by the first observations of the stellar kinematics in ETGs (Bertola & Capaccioli 1975), which found much lower velocities than predicted by isotropic models (Illingworth 1977; Schechter & Gunn 1979). To quantify this discrepancy, the now-classic $(V/\sigma, \varepsilon)$ diagram was proposed (Binney 1978). It quantifies the ratio between the ordered rotation and the random motion in a stellar system, as a function of the observed (i.e. apparent) ellipticity ε of a galaxy.

When the observations could be extended to galaxy bulges (Kormendy & Illingworth

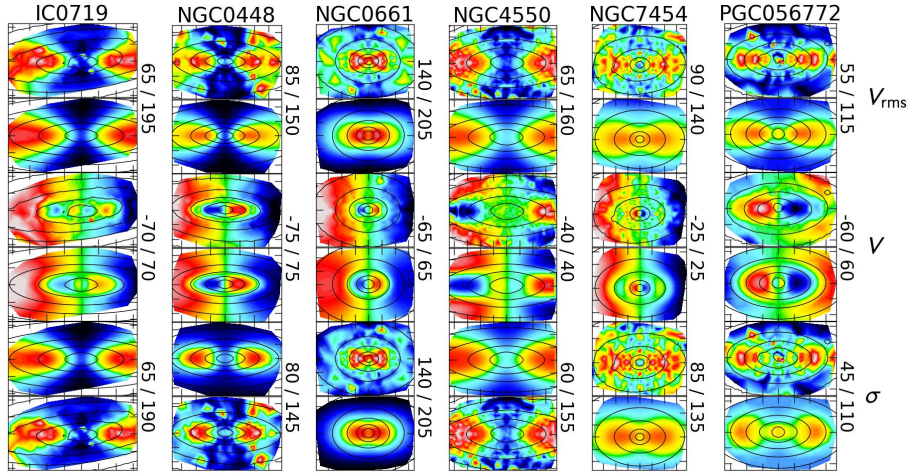


Figure 12

JAM models of counter-rotating disks. These are classified as 2σ by Krajnović et al. (2011). In each plot, the top panel shows the symmetrized SAURON stellar $V_{\text{rms}} \equiv \sqrt{V^2 + \sigma^2}$, the second panel is the best fitting JAM model to the V_{rms} , the third panel is the SAURON mean stellar velocity V , the fourth panel is the best fit to V obtained by keeping the best fitting anisotropy β_z , inclination i and M/L from the previous fit to the V_{rms} . The penultimate panel is the velocity dispersion σ , which is characterized by two maxima at the opposite sides of the nucleus, along the major axis. The bottom panel is the JAM model $\sigma = \sqrt{V_{\text{rms}}^2 - V^2}$. The SAURON data come from Cappellari et al. (2011a), except for NGC 4550, which comes from Emsellem et al. (2004). The MGE surface brightness comes from Scott et al. (2013a). The only difference from what was done in Figure 10, is that the fit to V allows for opposite sense of rotation for different Gaussians in the MGE. This reversal leaves the model V_{rms} rigorously unchanged. According to the models, the amount of mass that is affected by the counter-rotation ranges from about 10% for NGC 661 to about 50% for NGC 4550. This plot illustrates the physical continuity between the regular rotators and the counter-rotating disks.

1982; Kormendy 1982b,a) and fainter E ($M_B \gtrsim -21$, Davies et al. 1983), it was found these were instead more consistent isotropic rotators. A separation around $M_B \approx -20.5$ was suggested between (i) brighter ellipticals, with slow rotation and triaxial shapes, and (ii) fainter ellipticals with faster rotation. The former were thought to be significantly anisotropic and likely triaxial, while the latter were interpreted as nearly isotropic stellar systems “flattened by rotation”. The subsequent discoveries of a connection between E stellar rotation, isophotal shape (Section 2.3) and nuclear profile slopes (Section 2.4) significantly strengthened the case for two different types of E (Kormendy & Bender 1996; Faber et al. 1997).

The theoretical interpretation of the $(V/\sigma, \varepsilon)$ diagram is based on the tensor virial theorem, which relates the kinetic and potential-energy tensors in a stellar system (Binney & Tremaine 2008, section 4.8.3). The tensors are formally integrated over the full extent of the galaxies. However, for decades the V/σ could only be measured in galaxies using long slit kinematics, which provide only a crude approximation of the global galaxy kinematics.

3.5.2. Formalism for integral-field kinematics. The advent of IFS motivated a more rigorous and robust formulation of the theoretical diagram in which the V and σ are luminosity-weighted quantities integrated over the full extend of the system (Binney 2005). The first ap-

plication of Binney's revised $(V/\sigma, \varepsilon)$ formalism, performed the luminosity-weighting within an ellipse which encloses half of the projected total galaxy light (Cappellari et al. 2007). In this case the observed quantity becomes

$$\frac{\langle V^2 \rangle}{\langle \sigma^2 \rangle} \approx \left(\frac{V}{\sigma} \right)_e^2 \equiv \frac{\sum_{n=1}^N F_n V_n^2}{\sum_{n=1}^N F_n \sigma_n^2}, \quad (13)$$

where V_n and σ_n are the mean stellar velocity and dispersion within a given spatial bin, F_n is the flux enclosed within that bin, and the sum is performed over all bins falling within the half-light ellipse. One can verify using theoretical models that, by limiting the sum to $1R_e$, the measured values are no more than $\Delta(V/\sigma) \lesssim 0.1$ lower than the theoretical ones, extended to infinite radii (Cappellari et al. 2007; Emsellem et al. 2011).

As shown by Binney (2005), for oblate galaxies with different anisotropies δ (Equation 7) and intrinsic ellipticity $\varepsilon_{\text{intr}}$, the theoretical prediction for an edge-on view is

$$\frac{\langle V^2 \rangle}{\langle \sigma^2 \rangle} = \frac{(1 - \delta)\Omega(e) - 1}{\alpha(1 - \delta)\Omega(e) + 1} \quad (14)$$

with

$$\Omega(e) = \frac{0.5 \left[(\arcsin e)/\sqrt{1 - e^2} - e \right]}{e - (\arcsin e)\sqrt{1 - e^2}}, \quad e = \sqrt{1 - (1 - \varepsilon_{\text{intr}})^2} \quad (15)$$

i: Galaxy inclination, with $i = 90^\circ$ being edge-on

and α is a parameter which depends on the shape, but not the amplitude, of the galaxy's intrinsic rotation curve, and its radial luminosity profile. A fixed value $\alpha \approx 0.15$ was found to provide a good representation of real galaxies (Cappellari et al. 2007) and will be adopted in what follows. The edge-on isotropic line and the corresponding edge-on relations for different anisotropies, are shown in the $(V/\sigma, \varepsilon)$ diagram of Figure 13. Given the edge-on ($i = 90^\circ$) values of $(V/\sigma, \varepsilon_{\text{intr}})$, their projection at different inclinations are

$$\left(\frac{V}{\sigma} \right)_e^{\text{obs}} = \left(\frac{V}{\sigma} \right)_e \frac{\sin i}{\sqrt{1 - \delta \cos^2 i}}, \quad \varepsilon = 1 - \sqrt{1 + \varepsilon_{\text{intr}}(\varepsilon_{\text{intr}} - 2) \sin^2 i}. \quad (16)$$

3.5.3. Results from integral-field data. The first application of this formalism to 66 galaxies with SAURON IFS revealed that, galaxies with the kinematic morphology of non-regular rotators (Figure 4a–d), tend to lie well below the isotropic line in the $(V/\sigma, \varepsilon)$ diagram (Cappellari et al. 2007). With the exception of the special class of counter-rotating disks (d), these slow rotating ETGs were generally bright (Emsellem et al. 2007) and consistent with the triaxial class of E galaxies found by the previous long-slit studies. However they were found to be only weakly triaxial and actually close to spherical and isotropic within $1R_e$ (Cappellari et al. 2007). Their intrinsic ellipticity was found to be smaller than $\varepsilon \lesssim 0.4$, as evidenced by the fact that all slow rotating galaxies had observed ε smaller than that value. The only significantly flattened slow rotating galaxies were found to be the counter-rotating disks (d). The regular rotators (e) showed a completely different distribution on the $(V/\sigma, \varepsilon)$. They were found to be broadly consistent with a population of randomly oriented axisymmetric galaxies, with oblate velocity ellipsoids ($\gamma \approx 0$), satisfying the anisotropy condition $\beta_z \lesssim 0.7 \times \varepsilon_{\text{intr}}$ of Equation 11, suggested by the detailed dynamical models (Section 3.4.2, Section 3.4.3). In fact the regular rotators on the $(V/\sigma, \varepsilon)$ diagram were found to be broadly distributed within the envelope defined by the edge-on relation of Equation 11 and its projection at different inclinations (Cappellari et al. 2007). These relations are shown in Figure 13. The anisotropy of regular rotators, within $1R_e$, was found

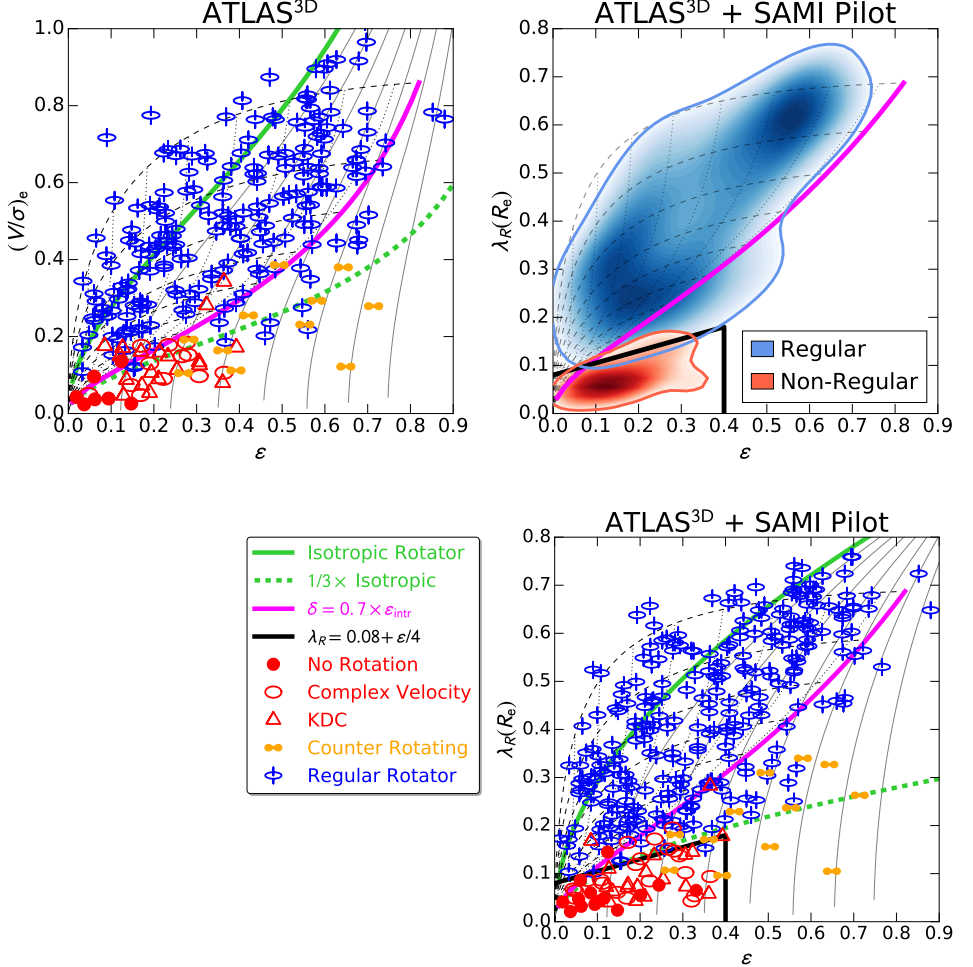


Figure 13

The $(V/\sigma, \varepsilon)$ and $(\lambda_{R_e}, \varepsilon)$ diagrams. *Top Left:* The symbols are the $(V/\sigma, \varepsilon)$ values for 260 ETGs from Emsellem et al. (2011), classified as in Figure 4. The green line is the prediction for an edge-on isotropic rotator, while the thin lines are separated by $\Delta\delta = 0.1$ in anisotropy, using Equation 14 (Binney 2005). The magenta line is the edge-on relation of Equation 11 (Cappellari et al. 2007), while the dotted lines indicate how this relation transforms at different inclinations using Equation 16. The distribution of regular rotators is broadly consistent with a family of axisymmetric systems following the anisotropy trends of Figure 9, seen at random orientations. Instead, the non-regular rotators tend to lie well below the magenta line. The two classes can be approximately separated by the line $(V/\sigma)^* = 1/3$ (dashed green line). *Bottom Right:* The symbols are the $(\lambda_{R_e}, \varepsilon)$ values for 340 ETGs from Emsellem et al. (2011) and Fogarty et al. (2015). The lines are the same as in the left panel, with the projected V/σ values transformed into λ_{R_e} using Equation 18 (Emsellem et al. 2007). The black line is the best empirical separation between regular and non-regular rotators of Equation 19. The black line nearly overlaps with the $(V/\sigma)^* = 1/3$ line on this diagram. *Top Right:* same as in the bottom panel, but using kernel density estimates for the regular/non-regular distributions. For each class, the thick solid lines enclose 80% of the total probability.

to span a larger range than that of the non-regular rotators. They are generally not close to isotropic, but often fall close to the edge-on isotropic line due to projection effects. This explains previous observations suggesting the fast rotating galaxies are more isotropic than the slow rotating ones. In practice, starting from a range of ε values, the edge-on magenta relation can be plotted on the $(V/\sigma, \varepsilon)$ diagram using [Equation 14](#) and [Equation 15](#), and then the different projections are obtained from [Equation 16](#).

Also shown in [Figure 13](#) is the relation $(V/\sigma)^* = 1/3$, where $(V/\sigma)^* \equiv (V/\sigma)/(V/\sigma)_{\text{iso}}$ is the ratio between V/σ and the corresponding theoretical value for an isotropic galaxy with the same ε . This parameter was called “anisotropy parameter” (e.g. [Kormendy & Illingworth 1982](#); [Davies et al. 1983](#); [Bender 1988](#); [Bender et al. 1992, 1994](#); [Naab & Burkert 2003](#)) although it is clear from [Figure 13](#), that galaxies with the same $(V/\sigma)^*$ can span the full range of anisotropies. Nonetheless, $(V/\sigma)^*$ is still a very useful to quantify the global dynamics of ETGs. In fact, [Cappellari et al. \(2007\)](#) noted that a value of $(V/\sigma)^* \approx 0.4$ approximately separates the fast/regular and slow/non-regular rotating classes indicated by the IFS kinematics ([Emsellem et al. 2007](#); [Cappellari et al. 2007](#)). This fact confirms and explains the early results, based on long-slit spectroscopy, reporting a connection between $(V/\sigma)^*$ and galaxy properties (e.g., [Davies et al. 1983](#); [Kormendy & Bender 1996](#)).

All these results about the $(V/\sigma, \varepsilon)$ diagram found by the SAURON survey ([de Zeeuw et al. 2002](#)), were confirmed and strengthened, with the volume-limited sample of 260 galaxies, by the ATLAS^{3D} survey ([Cappellari et al. 2011a](#)), which also provided a reliable census of the different classes of ETGs. The results were presented by [Emsellem et al. \(2011\)](#) and are reproduced, on top of the theoretical relations, in [Figure 13](#). The figure shows that the magenta line and its projections envelope, still broadly describes the location of regular rotators on the $(V/\sigma, \varepsilon)$ diagram. Again a fixed $(V/\sigma)^*$ value provides a rough separation of the two main kinematic classes, and the larger sample allows one to more accurately define the dividing line around $(V/\sigma)^* \approx 1/3$.

The ATLAS^{3D} survey uncovered 11 counter-rotating disks ([Figure 12](#)), which constitute 4% of the volume-limited ETG sample ([Krajnović et al. 2011](#)). They can appear quite flat, as expected due to their disk-like nature. However, unlike the regular rotators, they all lie below the magenta line in the $(V/\sigma, \varepsilon)$ diagram, because they do not have oblate velocity ellipsoids, but are instead dominated by tangential anisotropy ($\sigma_\phi > \sigma_R$ or $\gamma < 0$). Below the magenta line one also finds some galaxies which are classified as regular rotators by [Krajnović et al. \(2011\)](#). These are likely transition objects containing an amount of counter-rotating stars which is too small to produce clear evidence for counter-rotation in the σ field, but sufficiently large to produce a detectable decrease of their global rotation. There is in fact no reason to expect a sharp transition between the regular rotators and the counter-rotating disks. The classification into one class or the other will simply depend on the amount of externally-acquired counter-rotating gas ([Bois et al. 2011](#)).

3.6. Quantitative kinematic classification

3.6.1. Early-type galaxies. It is useful to define a quantitative measure which approximately encodes the visual distinction between the two classes of regular and non-regular rotators illustrated in [Figure 4](#). A physically-motivated and clean separation can be obtained using dynamical models ([Figure 11](#)). And this approach can be used when maximum accuracy is desired. However it may be possible to define a more economical approach.

Another alternative is to use the dividing line $(V/\sigma)^* \approx 1/3$ on the $(V/\sigma, \varepsilon)$ diagram

(Section 3.5.3). However the V/σ quantity has one major limitation: it makes no use of the spatial distribution in the kinematic maps. For this reason a galaxy with a KDC like NGC 5813 (Figure 4c) can overlap on the $(V/\sigma, \varepsilon)$ diagram with inclined regular rotators (e.g. NGC 3379) which have dramatically different kinematic appearance, as noted by Emsellem et al. (2007). This was the motivation to develop a new physical parameter which retains the useful characteristics of the classic V/σ quantity, but also includes spatial information. A natural replacement for V is the magnitude of the luminosity-weighted averaged projected angular momentum $\langle \mathbf{L} \rangle = \langle \mathbf{R} \times \mathbf{V} \rangle$. To remove the need to determine vector directions and make a more easily computable quantity, this quantity was replaced by the surrogate $\langle R|V| \rangle$, where R is the projected distance from the galaxy center. When this proxy for the angular momentum is made dimensionless and normalized with a quantity like the $V_{\text{rms}} \equiv \sqrt{V^2 + \sigma^2}$, which is proportional to mass, according to the scalar virial theorem (Binney & Tremaine 2008), one obtains the parameter (Emsellem et al. 2007)

$$\lambda_R \equiv \frac{\langle R|V| \rangle}{\langle R\sqrt{V^2 + \sigma^2} \rangle} = \frac{\sum_{n=1}^N F_n R_n |V_n|}{\sum_{n=1}^N F_n R_n \sqrt{V_n^2 + \sigma_n^2}}, \quad (17)$$

where the F_n are the fluxes within the N spatial bins where mean stellar velocities V_n and velocity dispersion σ_n are measured. And the summation is extended out to a certain finite radius R_{max} , within a galaxy isophote.

The distribution of the $(\lambda_{R_e}, \varepsilon)$ values for ETGs for ATLAS^{3D} (from Emsellem et al. 2011) and the SAMI Pilot survey (from Fogarty et al. 2015), is shown in Figure 13 (CALIFA is not included here because kinematics is not yet available). Also overlaid are the same lines shown in the $(V/\sigma, \varepsilon)$ diagram, computed with the analytic expression of Equation 14–Equation 16, as well as the anisotropy-shape relation of Equation 11. To calculate those lines, the *projected* location on the $(V/\sigma, \varepsilon)$ diagram were simply converted into the corresponding ones for the $(\lambda_{R_e}, \varepsilon)$ diagram using the empirical calibration below (Emsellem et al. 2007, 2011)

$$\lambda_{R_e} \approx \frac{k(V/\sigma)_e}{\sqrt{1 + k^2(V/\sigma)_e^2}} \quad \text{with} \quad k = 1.1 \quad (18)$$

Given the close relation between V/σ and λ_{R_e} , broadly speaking, the $(\lambda_{R_e}, \varepsilon)$ diagram shows the same information as the $(V/\sigma, \varepsilon)$ diagram. Regular rotators are still generally described by the envelope of the magenta line and its projections, while non-regular rotators are not. The difference between the two diagrams is that, on the $(\lambda_{R_e}, \varepsilon)$ diagram the regular and non-regular rotators of Krajnović et al. (2011) are significantly better separated (Emsellem et al. 2011).

More recently, the SAMI-pilot sample of Fogarty et al. (2015) and the CALIFA one by Falcón-Barroso et al. (2015) increased the number of slow rotators by $2.5\times$. They strongly confirm the ATLAS^{3D} finding that “genuine” disk-less slow rotators are all rounder than $\varepsilon_e < 0.4$. Counter-rotating disks were shown in Section 3.4.3 to be structurally equivalent to regular-rotators and should not be classified as slow rotators. The new data motivate a refinement to the $\lambda_{R_e} = 0.31\sqrt{\varepsilon_e}$ fast/slow rotator division of Emsellem et al. (2011) as follows, to reduce the risk of missing very round non regular rotators (see Figure 13)

$$\lambda_{R_e} < 0.08 + \varepsilon_e/4 \quad \text{with} \quad \varepsilon_e < 0.4. \quad (19)$$

The explicit inclusion of the roundness criterion in the classification allows one to identify ETGs with disks, or fast rotators, without the need for kinematic observations.

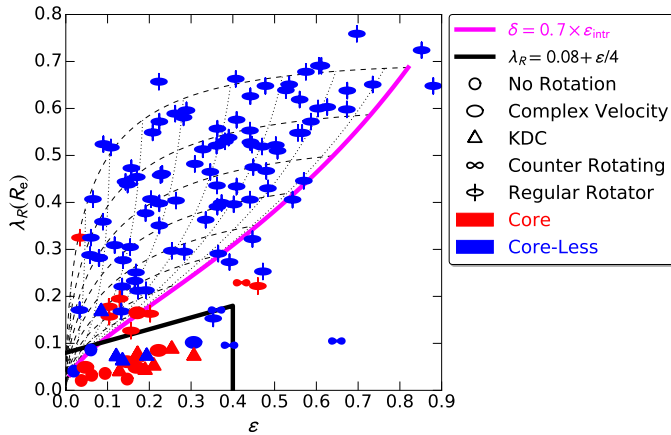


Figure 14

Cusps and cores on the $(\lambda_{R_e}, \varepsilon)$ diagram. The values and symbols are the same as in Figure 13, but only for the galaxies for which a core or core-less classification exists (taken from Krajnović et al. 2013b). The magenta line is the same $\delta = 0.7 \times \varepsilon_{\text{intr}}$ (Cappellari et al. 2007) as in Figure 13, while the brown line is the fast/slow rotator divide of Equation 19. There is a broad agreement between the slow rotators and the core galaxies, but not a full overlap.

The separation between fast and slow rotators was defined by Emsellem et al. (2007, 2011) for λ_{R_e} measured within the half-light isophote. For this reason a galaxy cannot change its class when more extended data become available. In this classification like in most other ones, the *scale* is important! The same is true e.g. for Hubble’s classification: a nuclear dust disk in an E galaxy may resemble a spiral galaxy from HST observations alone (e.g. Young et al. 2008). But this does not make us classify the galaxy a spiral. Similarly, an E which turns out to have extended spiral arms in very deep observations (e.g. Duc et al. 2015), should not be classified as a spiral.

We stress that the classification based on the $(\lambda_{R_e}, \varepsilon)$ diagram only constitutes an automatic and objective proxy for the more detailed classification based on the kinematic morphology of Figure 4. For reliable results it is important to verify that the two agree! This implies that, when the data are of such a low quality that no visual classification is possible, one should avoid using the $(\lambda_{R_e}, \varepsilon)$ alone to kinematically classify ETGs, as this may lead to meaningless results. This is because systematic effects, like spurious fluctuations, on the velocity fields, produce systematic biases in λ_{R_e} , as discussed by Emsellem et al. (2007).

3.6.2. Connection between dynamics and nuclear surface brightness profiles. As discussed in Section 2, the slow/fast rotator classes are expected to trace a similar phenomenon as the core/core-less classes respectively. This hypothesis was tested by Emsellem et al. (2011) using a sample of 56 galaxies with measured central light deficit from either Kormendy et al. (2009) or Glass et al. (2011). They concluded that there is indeed a close connection between being a slow rotator and having a central deficit in the surface brightness, with respect to a Sersic (1968) profile extrapolated from larger radii. However the two classifications were not found to agree in all cases.

The question was revisited by Lauer (2012), using a subset of 63 galaxies in common

between the ATLAS^{3D} sample and the “Nuker” sample of Lauer et al. (2007b). He concluded that the two indicators generally agree, confirming they are both able to recognize dry merger relics. Krajnović et al. (2013b) doubled the size of both samples to 122 galaxies, thanks to new HST photometric determinations. They used a core versus core-less definition based on a “Nuker” profile fit (Equation 4), but they showed that different criteria differ only at the $\sim 3\%$ level. The main figure from that paper is adapted here in Figure 14. In agreement with the previous studies, one can see that the general agreement is very good: Nearly all round and slow rotating ETGs do indeed have a core, and the vast majority of the regular rotator have a steep profile as expected. However core and core-less ETGs do *not* overlap perfectly with the regular versus non-regular rotator classes, and for the same reason they do not separate precisely at the slow/fast rotator divide.

To understand, at least in part, the small disagreements between the core/core-less and slow/fast classifications, it is instructive to consider a few individual examples. Three of the core-less slow rotators are counter-rotating disks (Figure 4d). As these objects have disks and must have formed via gas accretion, the lack of a core makes physical sense and further emphasizes the fact, discussed in Section 3.4.3, that counter-rotating disks are essentially “misclassified” slow rotators, which instead form a continuous sequence with the rest of the fast rotators. One of the counter-rotating disks however has a core. This galaxy is the well-studied E galaxy NGC 4473. The cored nature of its inner profile was studied in detail by Pinkney et al. (2003), who suggested it may be due to a recent merger, which flattened a pre-existing cusp. The dynamics of NGC 4473 was modeled in detail in Cappellari & McDermid (2005) and Cappellari et al. (2007). It was found to consists of two counter-rotating stellar components with approximate mass ratio 1:3. This galaxy was proposed as a prototype of the counter-rotating class. The large-scale stellar counter-rotation, and the “lemniscate” (which motivates the symbol used in this review to represent the kinematic class), or figure-of-eight, or “double σ ” peaks, nature of this galaxy is beautifully illustrated by the combination of the SAURON and SLUGGS kinematics in Foster et al. (2013). In summary, this galaxy does not differ from the other counter-rotating disks, and in this case the “core” classification does not imply the galaxy assembled by dry mergers like the core slow rotators.

Overall, as these few examples already illustrate, it is not surprising that the two core/core-less and slow/fast classifications do not agree in 100% of the cases, although they agree most of the times. A galaxy which formed predominantly via gas accretion and originally posses a steep inner profile, may sometimes acquire a small gas-poor satellite which, in favorable conditions can destroy the inner cusp and nuclear disk (Sarzi et al. 2015), producing a core galaxy. The fact that most fast rotators are core-less indicates that this event is not a common occurrence. The small disagreement between the two classifications shows that, like in any classification, intermediate cases may exist and one should consider different characteristics of a galaxy, before making strong inferences about the formation mechanism of any individual object. The safest choice in this case is to consider as dry merger remnant only galaxies which *both* are classified as slow rotators and have an inner core. But unfortunately this information is not available for many galaxies. However the broad agreement indicates that, on a statistical basis either method is robust and allow one to draw conclusions about the overall galaxy population.

3.6.3. Angular momentum across the Hubble sequence. In the $(V/\sigma, \varepsilon)$ and $(\lambda_{R_e}, \varepsilon)$ diagrams we used a single ε per galaxy. However this quantity is not constant within a galaxy.

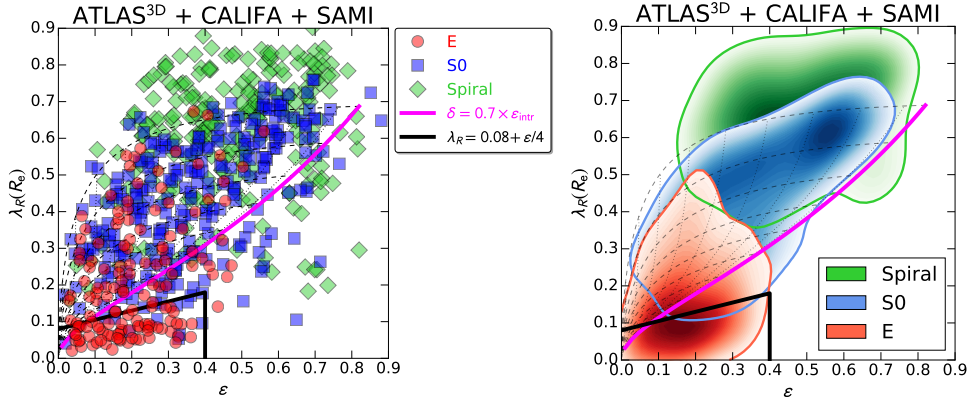


Figure 15

Galaxy morphology on the $(\lambda_{R_e}, \epsilon)$ diagram. *Left Panel:* Shows 666 $(\lambda_{R_e}, \epsilon)$ values, including 260 ETGs in ATLAS^{3D} (from Emsellem et al. 2011), 300 mostly spiral galaxies in CALIFA (from Falcón-Barroso et al. 2015) and 106 galaxies mostly ETGs in SAMI (from Fogarty et al. 2015). The magenta line is the same $\delta = 0.7 \times \epsilon_{\text{intr}}$ relation (Cappellari et al. 2007) as in Figure 13, while the brown line is the fast/slow rotator divide (Equation 19). The CALIFA sample by design lacks very round and very flat spiral galaxies and this explain their apparently different distribution in ϵ from the ETGs. In this extended sample, which has $2.5 \times$ more slow rotators than ATLAS^{3D}, all secure slow rotators (i.e. excluding counter-rotating disks, cuspy ETGs and spirals) have $\epsilon \lesssim 0.4$. *Right Panel:* Shows a kernel density estimate of the distributions of Es, S0s and spirals in the left diagram. For each class, the thick solid line encloses 80% of the probability. The region of slow rotators encloses almost only Es.

In fact fast rotators are galaxies with a bulge and a disk. The flattest ones tend to be the more disk dominated ones. This means that the fast rotators near the top of the $(\lambda_{R_e}, \epsilon)$ diagram are expected to be on average the ETGs with small bulge fractions. This trend of decreasing λ_{R_e} with increasing bulge fraction, or concentration, was shown by Krajnović et al. (2013a). It has a large scatter due to projection effects, which make the observed ellipticity a poor estimator of bulge fraction, and the observed λ_{R_e} an equally poor estimator of the intrinsic angular momentum. In this picture one would expect spiral galaxies, which on average have smaller bulge fractions than S0s (e.g. Simien & de Vaucouleurs 1986; de Jong 1996; Graham 2001; Graham & Worley 2008), to overlap with the fast rotators ETGs with the largest λ_{R_e} values. This was shown by Falcón-Barroso et al. (2015) (see also Querejeta et al. 2015), including IFS kinematics of spiral galaxies from the CALIFA survey (Sánchez et al. 2012). The trend between λ_{R_e} and galaxy concentration was also confirmed using data from the SAMI Pilot Survey by Fogarty et al. (2015). An exception are the latest spiral galaxy types (Sd) which appear to have quite low λ_{R_e} . An explanation for this fact will need to await a more detailed analysis on the kinematics of those objects, which is not yet available.

In Figure 15 we illustrate the trend between galaxy morphology and λ_{R_e} by combining data from the three largest IFS survey for which homogeneously measured parameters were published, for a total sample of 666 galaxies of all morphological types: ATLAS^{3D} (Cappellari et al. 2011a), CALIFA (Sánchez et al. 2012) and SAMI Pilot (Fogarty et al. 2014). We take (i) 260 values for the ETGs of the ATLAS^{3D} survey from Emsellem et al. (2011), (ii) 300 values for all morphological types, but mostly spiral galaxies of the CALIFA

survey from [Falcón-Barroso et al. \(2015\)](#) and Falcón-Barroso et al. in preparation, and (iii) 106 values for all morphological types, but mostly ETGs from SAMI from [Fogarty et al. \(2015\)](#). One should note that, unlike for the ETGs, the distribution for the spiral galaxies, which mostly come from CALIFA, is not randomly oriented by design ([Walcher et al. 2014](#)) and this explains the lack of very flat or very round spiral galaxies. Unlike the ETGs, these galaxies should not be approximately distributed like the envelope of the magenta line.

An interesting result of this plot is that the area of this diagram populated *only* by Es, approximately traces the region defining the slow rotator class ([Equation 19](#)). This shows that, even from images alone, the E classified as slow rotator look different from S0 galaxies and cannot be mistaken for S0s. The same is not true for the E classified as fast rotator, in the same range of ellipticity, which can be classified as either E or S0. This result further confirms the adopted criterion to separate the two classes of fast and slow rotators.

Overall, the plot clearly shows that the classic and still widely used distinction between E and S0 ([Hubble 1936; Sandage 1961; de Vaucouleurs et al. 1991](#)) has little physical meaning, in fact many inclined fast rotators are classified as E. This is mainly due to the obvious difficulty of recognizing an inclined S0 from a genuinely E galaxy. The fact that E always have $\varepsilon \lesssim 0.5$ is essentially a matter of definition. For this reason flat fast rotators are always classified as S0. The misclassification of E is very significant. In the volume-limited ATLAS^{3D} sample, as much as 66% (= 2/3) of E turns out to be a fast rotator, namely an inclined axisymmetric galaxy with a disk ([Emsellem et al. 2011](#)). Similarly, in the combined sample of [Figure 15](#), which has twice as many E galaxies, 60% are actually fast rotators. Most misclassifications can be corrected using other photometric indicators like isophotal shape, for edge on cases, and more in general nuclear slopes ([Kormendy & Bender 1996](#)), but these are currently not applicable to large surveys or at high redshift.

3.7. Two-dimensional Stellar population

Integral field spectroscopy provides spatially-resolved stellar population information together with the stellar kinematics. Using profiles of stellar population parameters averaged over elliptical isophotes, [Kuntschner et al. \(2010\)](#) found a trend of increasing metallicity gradient with increasing galaxy mass for low-mass fast rotators $M_* \lesssim 3 \times 10^{10}$, while the slopes decrease above that critical mass, so that the most massive systems have quite shallow logarithmic gradients. This finding agrees with long-slit observations by [Spolaor et al. \(2009\)](#). The majority of the population was found to have negligible age trends. This is also true for slow rotators with KDCs, which have a population indistinguishable from the rest of the galaxy, in agreement with the SAURON observations of NGC 4365 by [Davies et al. \(2001\)](#) and the OASIS high-resolution observations by [McDermid et al. \(2006\)](#).

It had been suggested that the local escape velocity V_{esc} , derived from dynamical models in which mass follows light, may be a better parameter to study stellar population gradients. The key advantage is that using V_{esc} , instead of radius, one finds local relations within a galaxy in quantitative agreement with global ones, among different galaxies. In particular [Franx & Illingworth \(1990\)](#) found a good correlation between V_{esc} and galaxy color, while [Davies et al. \(1993\)](#) and [Carollo & Danziger \(1994\)](#) found good global and local correlation of V_{esc} with the Mg absorption line strength, for two samples of 8 and 5 ETGs respectively. [Emsellem et al. \(1996\)](#) first investigated the Mg – V_{esc} correlation using IFS data.

The significance of the Mg – V_{esc} correlation was demonstrated by [Scott et al. \(2009\)](#) for the 48 ETGs of the SAURON survey and by [Scott et al. \(2013a\)](#) for the full ATLAS^{3D}

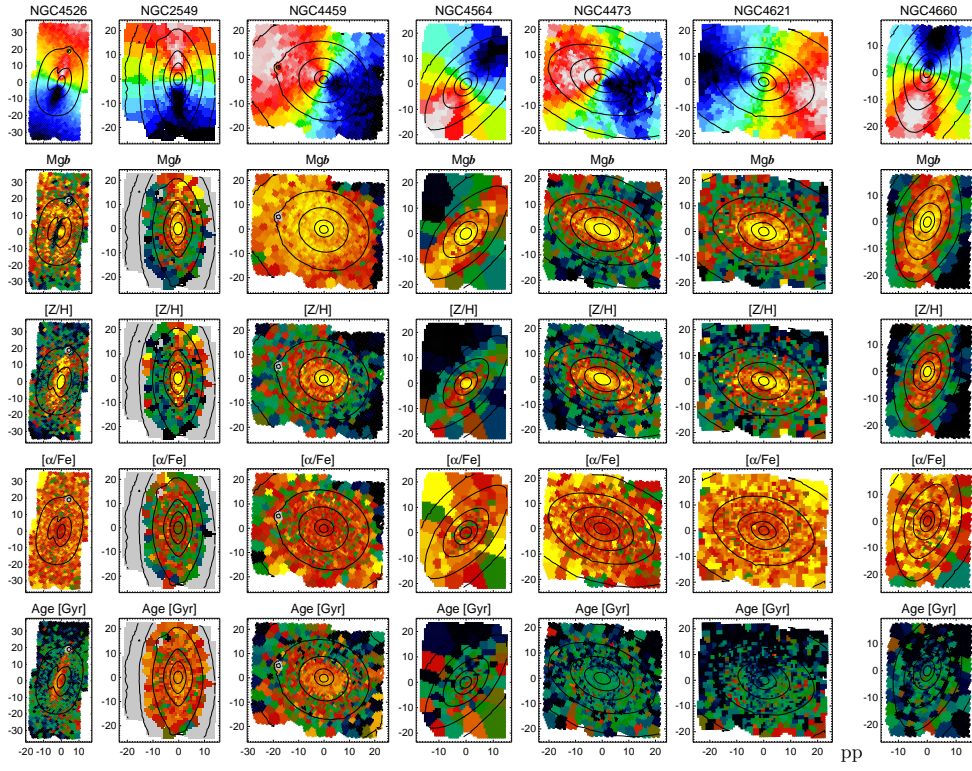


Figure 16

Metallicity enhanced disks in fast rotators. The top panels show the mean stellar velocity of seven fast rotator ETGs. Subsequent panels show the Mg b line strength, the metallicity [Z/H], the elemental abundance [α /Fe] and age. Strong nearly edge-on disks show an enhancement in the measured Mg b or the inferred metallicity, which is flatter than the isophotes, while the age distribution is flat and featureless (taken from Kuntschner et al. 2010). Exceptions are NGC 4526 and NGC 4459, which contain young star forming disks, also rich of molecular gas (Young et al. 2008).

sample of 260 ETGs. The dramatic improvement of these two studies was not only due to the large number of objects, but to the fact that IFS data allowed one to obtain very high quality radial gradient of the stellar population and accurate dynamical models. These studies showed that the Mg – V_{esc} is truly universal in passive ETGs, and constitutes an ideal benchmark for numerical simulations trying to describe in detail the local variations of stellar population in ETGs.

The IFS data not only provided accurate radial gradients, but also fully resolved spatial distributions. This fact revealed an increase of metallicity in fast rotators which is specifically associated with the disk component, rather than being uniformly distributed within the spheroidal or bulge component (Kuntschner et al. 2010; Scott et al. 2013a). This is indicated by the fact that all inclined fast rotators have contours of equal metallicity which are flatter than the galaxy isophotes, and generally consistent with the expected flattening of the disk component. This effect is visualized in Figure 16. The figure also shows that the disk do not stand out in the age maps.

In recent times, thanks to the availability of high-quality stellar population models (see Conroy 2013, for a review) with high spectral resolution based on large empirical spectral libraries (Bruzual & Charlot 2003; Vazdekis et al. 2012; Maraston & Strömbäck 2011; Conroy & van Dokkum 2012a), the studies of the stellar population from integral-field data has moved to the full-spectrum fitting approach (using fitting codes like pPXF Cappellari & Emsellem 2004; STARLIGHT Cid Fernandes et al. 2005; STECKMAP Ocvirk et al. 2006; VESPA Tojeiro et al. 2007). Recent results from the CALIFA (González Delgado et al. 2015), MASSIVE (Greene et al. 2015) and MaNGA surveys (Wilkinson et al. 2015), illustrate the power of IFS studies for stellar population. However a detailed overview of these stellar population studies goes beyond the scope of this review.

4. LOCAL SCALING RELATIONS

Dynamical scaling relations of ETGs relate the size, luminosity (L) and stellar kinematics of galaxies. Sizes are typically described by the half-light radius (R_e), while kinematics is generally quantified by the stellar velocity dispersion (σ) within a given aperture, which in this review is assumed no larger than R_e . Given that luminosity and size depend on distance, while kinematics do not, one of the first key applications of galaxy scaling relations was to infer galaxy distances (Dressler et al. 1987; Djorgovski & Davis 1987).

Nowadays, dynamical scaling relations are a key tool to study galaxy formation. The main reasons are: (i) because they provide a statistical description for easily measurable properties of galaxies as a function of time (redshift), which can be directly compared with numerical simulations (e.g. Robertson et al. 2006; Boylan-Kolchin et al. 2006; Oser et al. 2012; Porter et al. 2014); and (ii) due to the fact that scaling parameters are actually expected to evolve very differently depending on the galaxy formation mechanism (e.g. Naab et al. 2009; Hopkins et al. 2010).

In this section we review the recent development on scaling relations, focusing specifically on the advancements in our understanding of scaling relations made possible by the use of integral-field spectroscopy. Kormendy et al. (2009) and Graham (2013) present two contrasting overviews focused on results derived via photometry or long slit spectroscopy.

4.1. Classic scaling relations

4.1.1. Scaling relations and the Fundamental Plane. The first dynamical scaling relation to be discovered was the one between luminosity and stellar velocity dispersion (Faber & Jackson 1976). The observed relation had the form $L \propto \sigma^4$ and the authors pointed out it also suggests a trend between the mass-to-light ratio (M/L) and galaxy luminosity.

Soon thereafter, a correlation between galaxy surface brightness Σ and galaxy size was also found (Kormendy 1977). When one defines the surface brightness as the mean value within R_e , then $\Sigma_e = L/(2\pi R_e^2)$. This means that the Kormendy relation describes a correlation between galaxy radius and luminosity. The latter form has the advantage that it does not explicitly include galaxy size on both axes of the correlation, reducing the covariance between the measured values. The $L - R_e$ relation (e.g. Shen et al. 2003) has recently become quite popular to study galaxy evolution as a function of redshift (e.g. van der Wel et al. 2014), given that it does not involve any kinematic determination and for this reason is much more “economical” to observe than the Faber-Jackson.

Thanks to larger systematic surveys of ETGs it was later discovered that the Faber-

Fundamental Plane (FP): The distribution of (L, σ, R_e) galaxy parameters

Virial relation:
 $M \propto \sigma^2 R_e$

Jackson and the Kormendy relations are just two special projections of a plane described by galaxies in $(\log L, \log \sigma, \log R_e)$ coordinates (Dressler et al. 1987; Djorgovski & Davis 1987). This plane was aptly named the Fundamental Plane (FP, see Kormendy & Djorgovski 1989 for a review of the initial results). It was found to hold for all ETGs, including S0s and E galaxies, with a scatter smaller than 20% in R_e (e.g. Jorgensen et al. 1996).

The existence of the FP was interpreted as due to galaxies satisfying virial equilibrium $M \propto \sigma^2 R_e$, with M the galaxy mass (Faber et al. 1987). However the exponents of the FP were found to deviate significantly from the virial predictions, as confirmed by all numerous subsequent studies (e.g. Hudson et al. 1997; Scodégio et al. 1998; Pahre et al. 1998; Colless et al. 2001; Bernardi et al. 2003). In particular, a recent determination of the plane with σ_e measured from IFS within R_e , gives $L \propto \sigma_e^{1.25} R_e^{0.96}$ (fig. 12 in Cappellari et al. 2013b). This deviation of the FP from the virial predictions is called the “tilt” of the FP.

4.1.2. Why the Fundamental Plane deviates from the virial relation. The variation of the M/L of the stellar population was immediately recognized as a potential source for the tilt of the FP (Faber et al. 1987). This is because systematic changes in the galaxy population were already known, with galaxies becoming older and more metal rich with increasing mass or σ (e.g. Thomas et al. 2005; McDermid et al. 2015). This variation can potentially explain a major part of the FP tilt and scatter, predicting larger M/L as a function of σ by a factor of a few, as observed (depending on the photometric band) over the full range of galaxy masses (Prugniel & Simien 1996; Forbes et al. 1998).

The surface brightness profiles of ETGs also display systematic variations as a function of their luminosity, with profiles becoming more concentrated in more luminous objects (Section 2.2). At fixed mass, a steeper profile implies a larger σ within the central regions (Ciotti 1991) where the kinematics is observed. The amount of σ variation is again in principle sufficient to explain a major part of the FP tilt (Ciotti et al. 1996; Graham & Colless 1997; Prugniel & Simien 1997; Bertin et al. 2002; Trujillo et al. 2004a).

A third potential cause for the FP tilt is the fraction of dark matter within the region where kinematics is observed. The dark matter fraction is expected to increase systematically with mass, for the range of interest of FP studies (e.g. Moster et al. 2010, 2013; Behroozi et al. 2010; Guo et al. 2010; Leauthaud et al. 2012). This can cause variations in the observed total M/L of an amount again sufficient to produce a significant fraction of the measured tilt (Renzini & Ciotti 1993; Borriello et al. 2003; Tortora et al. 2012).

4.2. Understanding scaling relations via integral-field spectroscopy

4.2.1. The Mass Plane follows the virial relation. Using semi-isotropic Jeans models, and stellar kinematics of 37 galaxies from long-slit observations, it was found that the M/L trend with galaxy mass remains nearly unchanged when one includes the effects of galaxy non-homology (van der Marel 1991; Magorrian et al. 1998). The model accuracy was improved by fitting models to IFS stellar kinematics. Using a sample of 25 galaxies and both the Schwarzschild and Jeans approaches, Cappellari et al. (2006) found that the $(M/L) - \sigma$ relation is extremely tight and “can be included in the remarkable series of tight correlations between σ_e and other galaxy global observables”. The relation was found to account for the entire scatter and tilt of the FP. Independent confirmations of these facts came from strong lensing studies (Bolton et al. 2007; Auger et al. 2010a).

This result was dramatically strengthened by two larger studies using integral-field

Mass Plane (MP):
The distribution of (M, σ, R_e) galaxy parameters

M_*^{dyn} : Dynamically determined total galaxy stellar mass

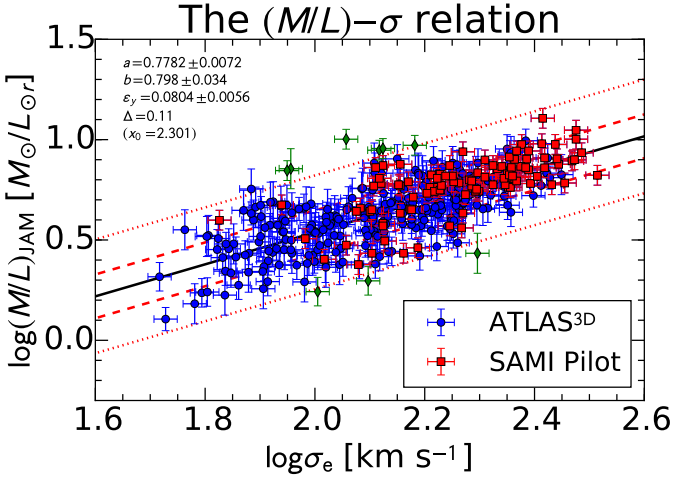


Figure 17

The $(M/L) - \sigma$ relation. The dynamical total r -band mass-to-light ratios and σ_e values for 366 ETGs. 260 ATLAS^{3D} ETGs come from Cappellari et al. (2013b) and 106 from the SAMI Pilot survey from Scott et al. (2015), with an extra correction for surface brightness dimming. In both cases the values were determined from JAM modeling of the IFS stellar kinematics. The two complementary samples agree extremely well. They define a tight relation of the form $(M/L)_r \propto \sigma^{0.80}$, consistent with earlier findings, with an observed scatter of 29%, decreasing to 20% for $\sigma_e > 200 \text{ km s}^{-1}$. The best fitting values of the linear relation $y = a + b(x - x_0)$, the observed rms scatter Δ in dex and the inferred intrinsic one ε_y are written in the top left corner.

stellar kinematics: the modeling the 260 ETGs of the ATLAS^{3D} sample (Cappellari et al. 2013b) and a similar study using 106 galaxies, of generally larger masses, from the SAMI Pilot Survey (Scott et al. 2015). Both studies employed the JAM method, which was shown using simulation to produce unbiased M/L estimates (Lablanche et al. 2012; Li et al. 2016). These modeling studies showed that, when replacing luminosity with mass in the FP (L, σ, R_e), the coefficients of the resulting Mass Plane ($M_{\text{JAM}}, \sigma, R_e$) matched the virial predictions $M \propto \sigma^2 R_e$ within the errors. However, the studies also pointed out the significant dependence of the plane coefficients on the technique used to measure them. This sensitivity explains the apparent contrast between some past studies of the FP tilt.

As demonstrated in detail by Cappellari et al. (2013b), the mass M_{JAM} which appear in the Mass Plane represent the most accurate empirical approximation of the galaxies total stellar mass M_*^{dyn}

$$M_{\text{JAM}} = L \times (M/L)_{\text{JAM}} \approx 2 \times M_{1/2} \approx M_*^{\text{dyn}}, \quad (20)$$

where L is the galaxy total luminosity and $M_{1/2}$ is the total mass contained within a sphere enclosing half of the total galaxy luminosity.

In Figure 17 we show the combined $(M/L) - \sigma$ values taken from both the ATLAS^{3D} survey (Cappellari et al. 2013b) and from the SAMI Pilot survey, in three different clusters (Scott et al. 2015). In both cases the values are computed in the SDSS r -band (AB mag system). Here, the published SAMI (M/L) values were divided by a factor $(1+z)^3$, to account for both the $(1+z)^4$ contribution from cosmological surface brightness dimming

and the $(1+z)^{-1}$ contribution due to the frequency decrease (as we are using AB mag) (e.g. Hogg 1999), at the typical redshift $z \approx 0.06$ of the observations. This correction was not included in the original paper (Scott et al. 2015). The resulting correlation, for a combined sample of 366 galaxies, has an observed scatter of $\Delta = 0.11$ dex (29%), from which we infer an intrinsic scatter of 20%. The scatter further decreases for the subsample of 69 galaxies with $\sigma_e > 200 \text{ km s}^{-1}$, for which the *observed* scatter becomes $\Delta = 0.078$ dex (20%). The best fitting relation was obtained with the Python version of the program `LTS_LINEFIT`² described in Cappellari et al. (2013b), which combines the Least Trimmed Squares robust technique of Rousseeuw & Van Driessen (2006) into a least-squares fitting algorithm which allows for errors in both variables and intrinsic scatter. It is given by

$$\left(\frac{M}{L_r}\right)_{\text{JAM}} = (6.00 \pm 0.10) \times \left(\frac{\sigma_e}{200 \text{ km s}^{-1}}\right)^{0.80 \pm 0.03}. \quad (21)$$

This relation, and its scatter, are consistent within the errors with the one for the ATLAS^{3D} subsample alone (Cappellari et al. 2013b), while the slope is also consistent with the one from Cappellari et al. (2006), albeit with much smaller errors. However both the scatter and the slope in the relation weakly depend on galaxy properties, with the relation being more shallow and having smaller scatter for galaxies in cluster and for slow rotators (Cappellari et al. 2013b), in agreement with previous IFS studies of the FP (Falcón-Barroso et al. 2011).

The M/L_r in r -band can be accurately converted to a different bands B using the color $(B-r)_{\text{gal}}$ of the galaxies and of the Sun $(B-r)_\odot$ as follows

$$M/L_B = (M/L_r) \times 10^{0.4[(B-r)_{\text{gal}} - (B-r)_\odot]}. \quad (22)$$

We used the B (Vega system) magnitudes from RC3 and the K_s (Vega system) magnitudes from 2MASS, which are available for all ATLAS^{3D} galaxies, to fit a tight color- σ relation. This was used, together with the Sun colors from Blanton & Roweis (2007), to provide the $(M/L) - \sigma$ relation in those two bands:

$$\left(\frac{M}{L_B}\right)_{\text{JAM}} = (7.46 \pm 0.12) \times \left(\frac{\sigma_e}{200 \text{ km s}^{-1}}\right)^{0.87 \pm 0.03} \quad (23)$$

$$\left(\frac{M}{L_{K_s}}\right)_{\text{JAM}} = (1.44 \pm 0.02) \times \left(\frac{\sigma_e}{200 \text{ km s}^{-1}}\right)^{0.58 \pm 0.03}. \quad (24)$$

The normalization of Equation 23 agrees within the relative errors with the one derived by van der Marel & van Dokkum (2007), but with a slightly more shallow slope.

A natural question is how much of the observed trend in M/L can be explained by variations in the stellar population, and to first order of its age and metallicity. The study by Gerhard et al. (2001), using detailed dynamical models, found that the dynamically-derived $(M_*/L)_{\text{dyn}}$ was related to the $(M_*/L)_{\text{pop}}$ inferred from stellar population models. This confirmed that at least part of the FP tilt is due to stellar population variations. It agrees with the fact that the scatter around the FP is also linked to variations in the stellar population (Graves et al. 2009; Falcón-Barroso et al. 2011; Springob et al. 2012; Magoulas et al. 2012). However, even improving the accuracy of the models using IFS kinematics, the relation between dynamically-derived *total* M/L and the stellar population $(M_*/L)_{\text{pop}}$ still showed significant systematic deviations (Cappellari et al. 2006). These could only be explained by either dark matter or IMF variations among galaxies.

²Available from <http://purl.org/cappellari/software>

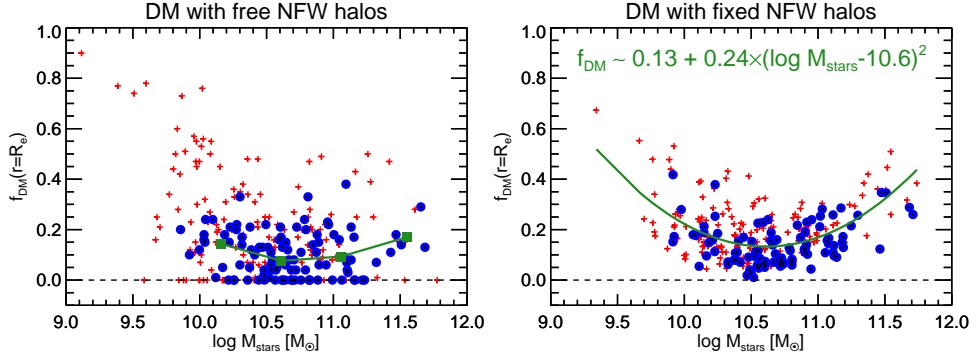


Figure 18

Dark matter from stellar dynamics. Either leaving the halo normalization as a free parameter in the models (left panel), or constraining it to the value predicted by Λ CDM (right panel), the inferred dark matter fractions within R_e must be small, for the models to be able to accurately fit the photometry and the IFS kinematics. Filled disks have better data, while red crosses have lower quality. (Taken from Cappellari et al. 2013b)

4.2.2. Little dark matter and non-universal stellar Initial Mass Function. Using long-slit data and general models for two samples of about 20 galaxies, different studies appeared to agree that dark matter represents a minor fraction of the total, within a sphere of radius $r \sim R_e$ (Gerhard et al. 2001; Thomas et al. 2011). Deviations between accurate determinations of the stellar and total masses were also found by combining the strong lensing technique with VIMOS integral-field observations (e.g. Barnabè et al. 2011) or using multiple long-slit observations (Thomas et al. 2011). The dark matter content within R_e was better quantified with the modeling of the IFS kinematics for the 260 ETGs of the ATLAS^{3D} sample (Cappellari et al. 2013b). A median dark matter fraction $f_{\text{DM}}(r = R_e)$ as low as 13% was measured for the full sample (Figure 18).

IMF: Stellar initial mass function

$(M_*/L)_{\text{pop}}$: Stellar mass-to-light ratio measured via stellar population

$(M_*/L)_{\text{dyn}}$: Stellar mass-to-light ratio measured via dynamical models

$f_{\text{DM}}(R_e)$: Fraction of dark matter within a sphere of radius R_e

Thanks to the large sample and two-dimensional stellar kinematics, the ATLAS^{3D} study was able to show that the systematic trend in the discrepancy between $(M_*/L)_{\text{dyn}}$ and $(M_*/L)_{\text{pop}}$ could not be explained by a variation in the dark matter fraction. The constraining power of the IFS data allowed the JAM dynamical models to explore, with a Bayesian approach, a range in dark matter inner slopes which included both a flat inner dark matter profile, a “standard” Navarro, Frenk & White (1996), and a contracted halos (Gnedin et al. 2004) as special cases. Even with this freedom, the models were unable to reproduce the photometry and IFS kinematics by varying the dark matter alone (see Cappellari et al. 2012, for an illustration). The only remaining option for the discrepancy was then a systematic variation of the stellar initial mass function (IMF) (Cappellari et al. 2012). This was inferred to vary in mass normalization from Milky-Way type (Kroupa 2001; Chabrier 2003) to heavier than Salpeter (1955) type, over the full mass range, with a dependence on the galaxies velocity dispersion (Cappellari et al. 2012, 2013a). The IMF variation contrasted with previous indications of universality (Bastian et al. 2010). However, the IMF for the most massive galaxies in the sample appeared consistent with previous indications of a “heavy” IMF in massive ETGs from either stellar population (van Dokkum & Conroy 2010) or strong gravitational lensing (Auger et al. 2010b). A recent update to the IMF – σ relation by Cappellari et al. (2013a), was obtained by combining $(M_*/L)_{\text{dyn}}$ determination

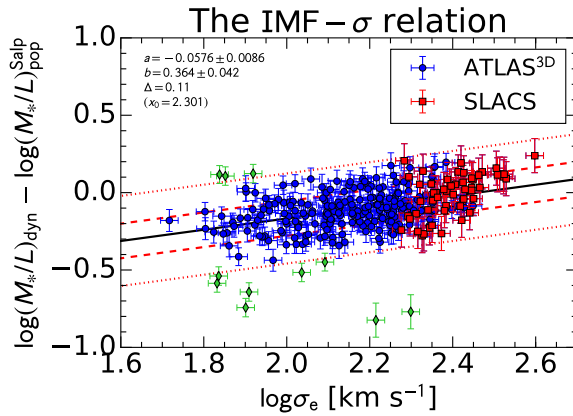


Figure 19

The IMF – σ relation. This is the relation between the ratio $\alpha \equiv (M_*/L)_{\text{dyn}}/(M_*/L)_{\text{pop}}$ between the stellar M/L inferred from mass dynamical or strong lensing modeling, and the same quantity inferred from full-spectrum fitting using stellar population models, assuming as a reference a Salpeter (1955) IMF. The dynamical models of the IFS ATLAS^{3D} data are taken from Cappellari et al. (2013b), while the combined lensing and dynamics models were based on the SLACS lens models of Treu et al. (2010), but were redone using axisymmetric JAM models for maximum consistency between the two sets of determinations. The two sets of data consistently indicate a mass excess that cannot be ascribed to dark matter and can be interpreted as a variation of the IMF (adapted from Posacki et al. 2015).

from ATLAS^{3D} with fully-consistent re-determination of $(M_*/L)_{\text{dyn}}$ from SLACS (Bolton et al. 2006), combining strong lensing masses with JAM models. It is shown in Figure 19, from Posacki et al. (2015). It illustrates the good agreement between the two approaches, and the need for a “heavy” IMF at the largest σ values.

The trend in IMF was found to be most closely related to the bulge mass fraction, as inferred from the galaxy dynamics, rather than to the galaxy mass alone. The heaviest IMF was generally measured for the densest fast rotator galaxies and not for the most massive galaxies (Cappellari et al. 2013a and Figure 22i). This result seems so far confirmed by individual studies of three dense ETGs using long-slit kinematics (Läsker et al. 2013) and IFS data (Yıldırım et al. 2015).

A large number of papers have appeared in recent years on the non-universality of the IMF in ETGs. Most of the studies used IMF sensitive spectral features in combination with stellar population models (e.g. van Dokkum & Conroy 2012; Conroy & van Dokkum 2012b; Spinelli et al. 2012; Smith et al. 2012a; Ferreras et al. 2013; Spinelli et al. 2015; La Barbera et al. 2015; Martín-Navarro et al. 2015b). Others used constraints provided by scaling relations (Dutton et al. 2013) or approximate dynamical models in combination with stellar population information (Tortora et al. 2013; Conroy et al. 2013). There is an encouraging consensus for the need for systematic IMF variations among different galaxies. However there are also clear tensions between different results, with stellar population models being unable to accurately predict the $(M_*/L)_{\text{dyn}}$ observed by dynamical or lensing approaches (Smith 2014), and possible contrast on the parameters driving the IMF variation (e.g. McDermid et al. 2014; Martín-Navarro et al. 2015b).

Initial studies at $z \sim 1$ found a Salpeter-like mass normalization of the IMF for $M_* \gtrsim 10^{11} M_\odot$ (Shetty & Cappellari 2014; Sonnenfeld et al. 2015). This is consistent with the IMF in the centers of massive nearby ETGs, assuming passive evolution. Similar consistency was found for the IMF at $z \sim 1$ from spectral features (Martín-Navarro et al. 2015a).

Integral-field spectroscopy has the potential of revolutionizing this field once more. In particular, the ongoing MaNGA survey (Bundy et al. 2015) combines a large wavelength range, which provides access to the most important IMF-sensitive spectral features (Conroy & van Dokkum 2012a), with good quality IFS data for a sample of 10,000 galaxies. The survey data can be used to try to reach a consensus, if possible, between different approach, and clarify our understanding of IMF trends in galaxies. Progress in this field can also be expected from MUSE observations, thanks to the impressive spectral data quality that the instrument can provide.

4.2.3. Nearly isothermal mass profiles to four half-light radii. In spiral galaxies, circular velocities could be measured decades ago using ionized (Rubin et al. 1980) and neutral gas (Bosma 1978). Observations indicated flat circular rotation curves and consequently nearly-isothermal $\rho_{\text{tot}} \propto r^{-2}$ profiles (see review by Courteau et al. 2014).

Mass profiles of ETGs are much more difficult to infer, as one generally has to use expensive observations of the stellar kinematics and more complex dynamical models. For this reason, until recently, most studies did not extend to radii much larger than R_e . Long-slit observations of two different samples of ≈ 20 ETGs revealed rotation curves to be nearly flat with nearly-isothermal mass profiles, as in spiral galaxies, within the median radius $r \approx 2R_e$ sampled by the kinematics (Gerhard et al. 2001; Thomas et al. 2011). Fully consistent results were independently found using strong gravitational lensing. In particular the SLACS survey (Bolton et al. 2006) found an isothermal slope, with small scatter, for the *total* galaxy density profile of 73 ETGs, at a typical radius of $r \approx R_e/2$ (Koopmans et al. 2009; Auger et al. 2010a).

For comparison, at groups and cluster scales, mass profiles derived using X-ray modeling indicate a trend in the total density profiles varying systematically from $\rho_{\text{tot}} \propto r^{-2}$ for the smallest systems, to $\rho_{\text{tot}} \propto r^{-1}$ for the largest ones (e.g. Humphrey & Buote 2010). A broadly consistent systematic trend was obtained by combining strong and weak lensing for massive galaxy clusters (Newman et al. 2013a, 2015). The stacked weak-lensing approach by Gavazzi et al. (2007) indicated on average isothermal profiles out to very large radii.

A number of studies of individual ETGs exist. They used observations of extended HI disks (Weijmans et al. 2008), deep observations of the stellar kinematics at sparse locations (Weijmans et al. 2009; Forestell & Gebhardt 2010; Murphy et al. 2011), the discrete kinematics determinations of individual globular cluster (Deason et al. 2012; Napolitano et al. 2014) and the kinematics of planetary nebulae (Romanowsky et al. 2003; de Lorenzi et al. 2008, 2009; Napolitano et al. 2011; Morganti et al. 2013). But a consistent picture did not emerge, due to inhomogeneity of the targets and observational techniques (see Gerhard 2013, for a review).

Only recently, large scale two-dimensional stellar kinematic data started to become available for statistically significant samples of ETGs (Brodie et al. 2014; Raskutti et al. 2014). Cappellari et al. (2015) combined the two-dimensional stellar kinematics of 14 fast rotator ETGs out to a median radius for the sample of $r \approx 4R_e$ from the SLUGGS survey (Brodie et al. 2014), with IFS within $\lesssim 1R_e$ from ATLAS^{3D} (Cappellari et al. 2011a). The data were modeled using the JAM approach. The study did not try to separate the

ρ_{tot} : Total, luminous plus dark, mass density

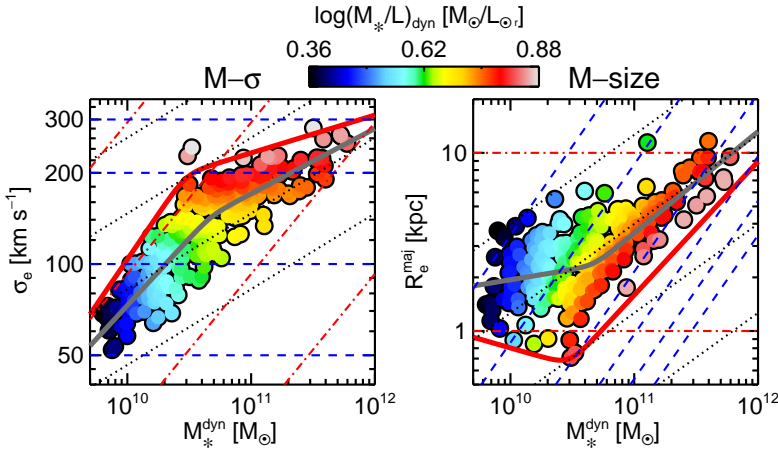


Figure 20

Break in scaling relations. The projections of the MP in the $(M_*^{\text{dyn}}, \sigma_e)$ and $(M_*^{\text{dyn}}, R_e^{\text{maj}})$ coordinates. Overlaid are lines of constant $\sigma_e = 50, 100, 200, 300, 400, 500 \text{ km s}^{-1}$ (dashed blue), constant $R_e^{\text{maj}} = 0.1, 1, 10, 100 \text{ kpc}$ (dot-dashed red) and constant $\Sigma_e = 10^8, 10^9, 10^{10}, 10^{11} \text{ M}_\odot \text{ kpc}^{-2}$ (dotted black) transformed in different panels using the virial relation. In each panel the galaxies are colored according to the (LOESS smoothed) $\log(M/L)_{\text{JAM}}$, as shown in the color bar at the top. In both panels the thick red line shows the same ZOE relation given by Equation 25. The gray line is the same $M_*^{\text{dyn}} - \sigma_e$ relation with trends $M_*^{\text{dyn}} \propto \sigma_e^{4.6}$ for $\sigma_e \gg 140 \text{ km s}^{-1}$ and $M_*^{\text{dyn}} \propto \sigma_e^{2.3}$ for $\sigma_e \ll 140 \text{ km s}^{-1}$. (Taken from Cappellari et al. 2013a)

luminous/dark matter components, as this generally requires making restrictive assumptions, but only focused on the *total* density, using a quite general parametrization. The resulting *total* density profiles were found well described by a nearly-isothermal power law $\rho_{\text{tot}}(r) \propto r^{-\gamma}$ from $R_e/10$ to at least $4R_e$, the largest average deviation being 11%. The average logarithmic slope is $\langle \gamma \rangle = 2.19 \pm 0.03$ with *observed* rms scatter of just $\sigma_\gamma = 0.11$. This scatter out to large radii, where dark matter dominates, is as small as previously reported by lensing studies at $r \approx R_e/2$, where the stars dominate.

The apparent profile universality seems part of a more general trend in the total density slopes. In fact the slopes within $r \lesssim R_e$, where models using IFS were constructed for large numbers of galaxies, already indicate (Figure 22c) that the total mass profiles become more shallow for galaxies with $\sigma_e \lesssim 100 \text{ km s}^{-1}$, while the profile remains indeed universal with high accuracy for larger σ_e , with just a small decrease in the absolute slope above the critical mass $M_{\text{crit}} \approx 2 \times 10^{11} \text{ M}_\odot$. However, larger samples of homogeneously modeled galaxies, are needed to understand whether these central trend persist at larger radii, where dark matter dominates. Profile slopes place important constraints to galaxy formation models (e.g. Remus et al. 2013; Dutton & Treu 2014).

4.3. The mass-size and mass- σ distributions

4.3.1. Results from integral-field spectroscopy. In Figure 20 we show two projections of the MP. As expected, from the thinness of the plane, both projections provide essentially the same information, simply transformed into a different coordinate system. The key novelties of this plot, made possible by the use of IFS data, are (i) that the stellar σ are not central

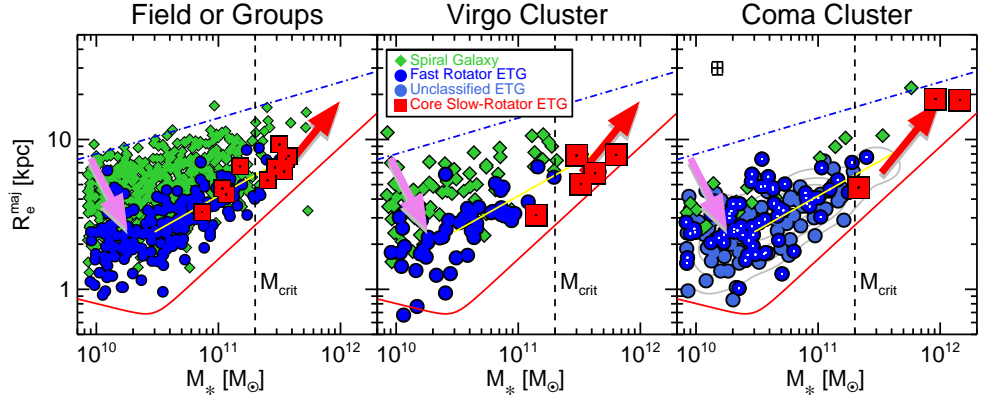


Figure 21

Mass-Size versus environment. The *Left Panel* shows the (M_*, R_e) distribution for a sample of galaxies belonging to either the field or to small groups. The *Middle Panel* is for a sample in the moderately-dense Virgo cluster and the *Right Panel* for a sample in the Coma cluster, which is one of the densest environments in the Universe. The plots visualize the two main channels for the formation of ETGs. The magenta arrow qualitatively indicates the evolutionary channel starting from star forming spiral galaxies and producing fast rotators via gas accretion and bulge growth followed by quenching. The red arrow shows the dry merging and halo quenching channel, producing massive slow rotators with central cores in their surface brightness profiles (the left and right panels are from Cappellari 2013).

values, but are integrated within an ellipse enclosing half of the total galaxy light, and thus more closely related to the galaxy mass appearing in the virial relation; (ii) the x-axis is not the commonly used luminosity or the stellar mass determined from stellar population models, but a dynamically-determined stellar mass $M_{\text{JAM}} \approx M_*^{\text{dyn}}$ (Equation 20), which includes possible variations in the stellar initial mass function (IMF). The accurate masses and σ allowed one to infer the following results (Cappellari et al. 2013a):

1. The distribution of galaxy properties on both projections is characterized by the same zone of exclusion (ZOE), which can be accurately converted from one projection to the other with the virial relation; The ZOE can be roughly approximated by a double power-law, with a break, or a minimum radius and maximum density, at a characteristic mass $M_b \approx 3 \times 10^{10} M_\odot$:

$$R_e^{\text{maj}} = R_b \left(\frac{M_*^{\text{dyn}}}{M_b} \right)^\gamma \left[\frac{1}{2} + \frac{1}{2} \left(\frac{M_*^{\text{dyn}}}{M_b} \right)^\alpha \right]^{(\beta-\gamma)/\alpha} \quad (25)$$

with $R_b = 0.7$ kpc, $\alpha = 8$, $\beta = 0.75$, $\gamma = -0.20$. The relation has an asymptotic trend $R_e^{\text{maj}} \propto (M_*^{\text{dyn}})^{0.75}$ above M_b , and a sharp transition into $R_e^{\text{maj}} \propto (M_*^{\text{dyn}})^{-0.20}$ below this break.

2. The ZOE produces a clear bend in both the *mean* $M - \sigma$ and $M - R_e$ relations, with trends $M_*^{\text{dyn}} \propto \sigma_e^{2.3}$ [correspondingly $R_e^{\text{maj}} \propto (M_*^{\text{dyn}})^{0.12}$] at small masses and $M_*^{\text{dyn}} \propto \sigma_e^{4.7}$ [correspondingly $R_e^{\text{maj}} \propto (M_*^{\text{dyn}})^{0.57}$] at large masses.
3. A second characteristic mass, at $M_{\text{crit}} \approx 2 \times 10^{11} M_\odot$, separates the axisymmetric fast rotators with disks, and the spiral galaxies, at lower masses, from the rounder slow rotators with inner cores in their stellar surface brightness, the robustly-determined

ZOE: Zone of exclusion

M_{crit} : Critical mass of about $2 \times 10^{11} M_\odot$, above which passive slow rotators with cores dominate

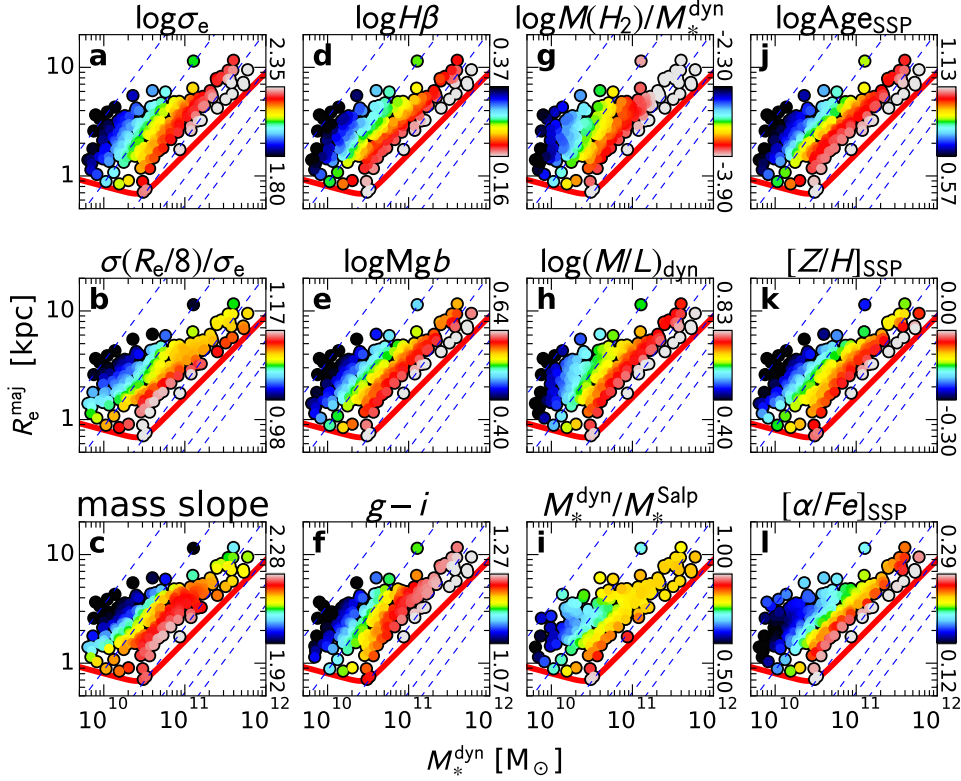


Figure 22

ETGs properties on the mass-size diagram. (a) Effective velocity dispersion σ_e (from Cappellari et al. 2013b); (b) Ratio between the central dispersion within $R_e/8$ and σ_e , which is related to the steepens of the mass profile (from Cappellari et al. 2013a); (c) Average logarithmic slope $\langle \gamma \rangle_r = \Delta \log \rho_{\text{tot}} / \Delta \log r$ in the interval $0.1-1R_e$, measured from models B of Cappellari et al. (2013b); (d) $H\beta$ line strength index within $R_e/2$; (e) Mgb line strength index within $R_e/2$ from McDermid et al. (2015); (f) $g - i$ color from SDSS (from Aihara et al. 2011); (g) Ratio of the molecular hydrogen H_2 from Young et al. (2011) and $M_*^{\text{dyn}} \equiv M_{\text{JAM}}$ from Cappellari et al. (2013b); (h) Total (luminous plus dark) dynamical $(M/L)_{\text{dyn}} \equiv (M/L)_{\text{JAM}}$ from Cappellari et al. (2013b); (i) Ratio $\alpha \equiv (M_* / L)_{\text{dyn}} / (M_* / L)_{\text{pop}}$ between the stellar M/L inferred from dynamical modeling, with the dark matter removed, and the same quantity inferred from full-spectrum fitting using stellar population models, assuming as a reference a Salpeter (1955) IMF (from Cappellari et al. 2013a); (j) Means SSP age (k) metallicity $[Z/H]$ and (l) elemental abundance $[\alpha/\text{Fe}]$ within $R_e/2$ (from McDermid et al. 2015); Panels b, d, f-i were presented in Cappellari et al. (2013a), and panels j-l in McDermid et al. (2015).

- dry merger relics (Section 3.6.2), at larger masses (Figure 21). The near absence of spiral galaxies above M_{crit} produces a sudden drop in the overall specific star formation of galaxies (Brinchmann et al. 2004; Salim et al. 2007). This steep decrease in the fraction of star forming systems is well approximated by a simple model in which the quenching rate is proportional to a galaxy star formation rate (Peng et al. 2010).
4. Below M_{crit} , galaxy properties closely follow lines of constant velocity dispersion (dashed in Figure 22). These lines trace (b) equal mass concentration or (c) equal

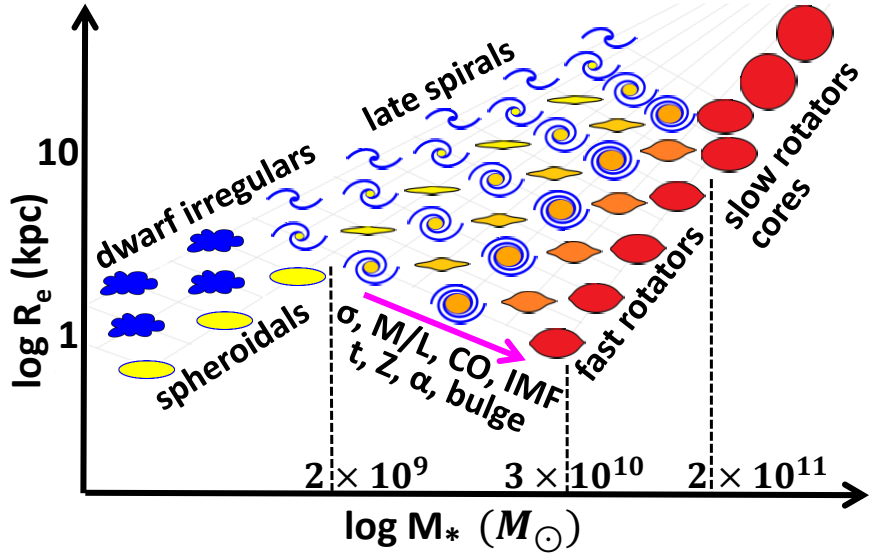


Figure 23

Galaxy properties on the mass-size diagram. All ETGs properties related to the stellar population or gas content tend to vary along lines of nearly constant σ_e , which traces the bulge mass fraction, or the steepness of the mass density profile. This sequence of ETGs properties merges smoothly with the one of spiral galaxies, with little overlap between late spirals (Sc-Irr) and ETGs, a significant overlap between early spirals (Sa-Sb) and fast-rotator ETGs with low M/L and no overlaps between spirals and fast-rotators with high M/L . Three characteristic masses are emphasized in this diagram: (i) below $M_* \approx 2 \times 10^9 M_\odot$ there are no regular ETGs and the mass-size lower boundary is increasing; (ii) $M_* \approx 3 \times 10^{10} M_\odot$ is the mass at which ETGs reach their minimum size (or maximum stellar density), before a sudden change in slope $R_e \propto M^{0.75}$ at larger masses; (iii) Below $M_* \approx 2 \times 10^{11} M_\odot$ ETGs are dominated by flat fast rotators, showing evidence for disks. Above this mass there are no spirals and the population is dominated by round or weakly triaxial slow rotators with flat (core/deficit) central surface brightness profiles. (adapted from Cappellari et al. 2013a)

steepness of the dynamically-determined mass density profile, or bulge mass fraction. Remarkably, this trend is true for nearly every galaxy parameter related to their stellar population, like (d) H β and (e) Mg b line strength, (f) optical color, (g) molecular gas fraction, (h) $(M_*/L)_{\text{dyn}}$, (i) IMF mass normalization, (j) age, (k) metallicity and (l) α -elements enhancement. *This show that galaxy formation model need to reproduce this crucial dependence on the central mass density if they want to describe reality.*

5. The sequence of ETGs properties, as a function of bulge fraction, merges smoothly with the sequence of spiral galaxies, which lie above the ETGs on the (M, R_e) diagram (Figure 21) (Cappellari et al. 2011a, 2013a; Kormendy & Bender 2012). Late spiral galaxies (Sc) lie near the top of the diagram at any given mass and do not overlap with the ETGs, while early spirals (Sa), which have smaller R_e , largely overlap with fast rotators with small σ_e . The densest and most spheroidal dominated fast rotators (including a number of disk E, Kormendy & Bender 1996) occupy the bottom of the diagram and do not overlap with the spiral galaxies.
6. At stellar masses below the ATLAS^{3D} selection limits, the sequence of spiral galaxies

SCALING RELATIONS FOR BULGES AND DISKS?

In the scaling relations presented in this paper (Figure 20–Figure 23) we treat galaxies as single entities and do not try to show separate scaling relations for bulges and disks. We prefer our global approach as it leads to more reproducible quantities. But this should not be interpreted as implying that the bulge/disk distinction is not physically meaningful. Instead, the popular photometric bulge/disk decompositions is a complementary way to approach the problems we study, which we did not have space to cover. These works reach conclusions that are remarkably consistent with the overall picture we infer from IFS observations, strengthening both conclusions (see Kormendy & Bender 2012; Kormendy 2016, for reviews). In the near future we envision an approach where photometric and IFS kinematic information are combined to bring bulge/disk decompositions to the next level. This will (i) reduce the inclination degeneracies that affect photometry alone and (ii) allow to quantify the kinematically-determined bulge/disk contributions.

and bulge-less fast rotators, smoothly continues with a sequence of dwarf spheroidals (see fig. 20 of Kormendy & Bender 2012 or fig. 9 of Cappellari et al. 2013a). Interestingly, the stellar mass $M_* \approx 2 \times 10^9 M_\odot$ where there is a sharp bend in the M -size relation of dwarf galaxies and the sequence of increasing bulge fraction starts, corresponds to the threshold for quenching of field galaxies discovered by Geha et al. (2012). They found that below that mass only the cluster or group environment can strip galaxies of their gas. Bulges growth cannot happen below that mass: star formation cannot be quenched by internal processes, but only by environmental ones.

All these empirical observations are graphically summarized in Figure 23. These results were interpreted by Cappellari et al. (2013a) as due to the build-up of ETGs happening via two separate routes: (a) in situ star formation: growth via gas accretion or minor gas rich mergers, which sinks towards the center and builds a bulge, which is associated with the quenching of star formation and disk fading (e.g. Cheung et al. 2012; Fang et al. 2013). This moves galaxies from left to right while crossing lines of constant σ_e . (b) external accretion: dry merging, increasing R_e by moving galaxies along lines of roughly constant σ_e (or steeper), while leaving the population unchanged (e.g. Bezanson et al. 2009; Naab et al. 2009; Hopkins et al. 2010).

4.3.2. Connection to previous results. The observed break in the $M - \sigma$ relation is consistent with previous reports of a change in the slope of the $L - \sigma$ relation of elliptical galaxies at low luminosities, where the relation was reported to become $L \propto \sigma^2$. An initial “marginally significant difference” in slope was noted by Davies et al. (1983). But it took a couple of decades for statistically significant results (Matković & Guzmán 2005; de Rijcke et al. 2005; Lauer et al. 2007a; Forbes et al. 2008; Tortora et al. 2009). However there is still some debate in the literature about the location and interpretation of the break. A break in the $M_* - \sigma$ at $M_* \approx 2 \times 10^{11} M_\odot$ was reported by large SDSS studies, but no break was observed at lower masses (Hyde & Bernardi 2009; Bernardi et al. 2011). In the review by Graham (2013), the break in the $L - \sigma$ is also reported at $M_B \approx -20.5$, which corresponds to the same $M_* \approx 2 \times 10^{11} M_\odot$.

Thanks to the quantitative consistency between the (M, σ) and the (M, R_e) projections, and the link to other observables, Figure 20 demonstrates that the break in $L - \sigma$ reported

in the earliest studies actually reflects the break in the ZOE around $M_* \approx 3 \times 10^{10} M_\odot$, and not around $M_* \approx 2 \times 10^{11} M_\odot$, where core slow rotators start dominating. In fact the break in the $M_* - \sigma$ relation persists even when all slow rotators with core are removed. However, it is also clear from Figure 21 that core slow rotators approximately follow the relation defined by fast rotators with $M_* \gtrsim 3 \times 10^{10} M_\odot$. However, the relation for core slow rotators is slightly steeper, producing a second break at $M_* \approx 2 \times 10^{11} M_\odot$ reported by SDSS. A more detailed picture above this interesting mass regime is expected from the MASSIVE IFS survey (Ma et al. 2014), but no kinematics was published yet.

A proper understanding of the break in the $M_* - \sigma$ relations is important for studies of supermassive BHs scaling relations. The existence of a break implies that the $M_{\text{bulge}} - M_{\text{BH}}$ (Marconi & Hunt 2003; Häring & Rix 2004) and $\sigma - M_{\text{BH}}$ (Gebhardt et al. 2000a; Ferrarese & Merritt 2000) cannot both be equally good predictors of BH masses (Lauer et al. 2007a; Graham 2012; Scott et al. 2013b). The break provides insight into the mechanism by which BH grow. This very interesting aspect was beautifully reviewed in Kormendy & Ho (2013) and it will not be further addressed here.

The sequence defined by the most passive (old, high metallicity, heavy IMF, CO poor,...) and bulge-dominated (large σ_e) galaxies in the (M, R_e) diagram is another view of the Kormendy (1977) relation between galaxy luminosity and effective surface brightness. However here the relation uses mass in place of luminosity. It is the end point of a continuous sequence, which starts from the bulge-less spirals and ends up at the ZOE. The existence of the ZOE at large stellar densities was noted before (Bender et al. 1992; Burstein et al. 1997). Importantly, the power-law $M - R_e$ relation defined by the most passive ETGs (red color in Figure 22) stops around the break in the ZOE at the characteristic mass $M_* \approx 3 \times 10^{10} M_\odot$. This mass was recognized by Kauffmann et al. (2003) as the divide between “two distinct families” of galaxies: star forming and disk-like below this mass, while passive and spheroidal-like above. Figure 22 and Figure 23 confirm and explain this result, but they also illustrate that mass, unlike σ_e , is actually *not* a good predictor of galaxy properties (also see Cappellari et al. 2006; Franx et al. 2008; Graves et al. 2009).

Unlike the bend in the $L - \sigma$ relation, the corresponding one in the more easily observable $L - R_e$ relation has been known for a long time. It was noted by Binggeli et al. (1984, their fig. 7) and further illustrated by a number of authors (e.g. Kormendy 1985; Graham & Guzmán 2003; Kormendy et al. 2009; Misgeld & Hilker 2011). Kormendy (1985) and Kormendy et al. (2009) see dwarf spheroidal as distinct from E galaxies, but rather constituting a separate family, of gas-stripped dwarf spirals/irregulars, while Graham & Guzmán (2003) and Graham & Worley (2008) interpret the curvature in the $L - R_e$ relation as a due to a smooth variation of the Sersic (1968) index with luminosity (e.g. Young & Currie 1994; Graham & Guzmán 2003) in an otherwise homogeneous class of E galaxies. Kormendy & Bender 2012 and Graham 2013 illustrate two different views on this subject. The ATLAS^{3D} results agree with the former interpretation, with the key difference that the class of fast rotator ETGs is now bridging the previous apparent gap between genuine E and dwarf spheroidals (Cappellari et al. 2013a).

The important link between bulge growth and quenching has also been observed using photometric data alone, both for local galaxies (Fang et al. 2013) and as a function of redshift (Bell et al. 2012; Cheung et al. 2012). The advantage of using dynamically-determined masses and density slopes is that it allows one to exclude population gradients (e.g. disk fading) as the only driver of the observed trend (e.g. Carollo et al. 2013).

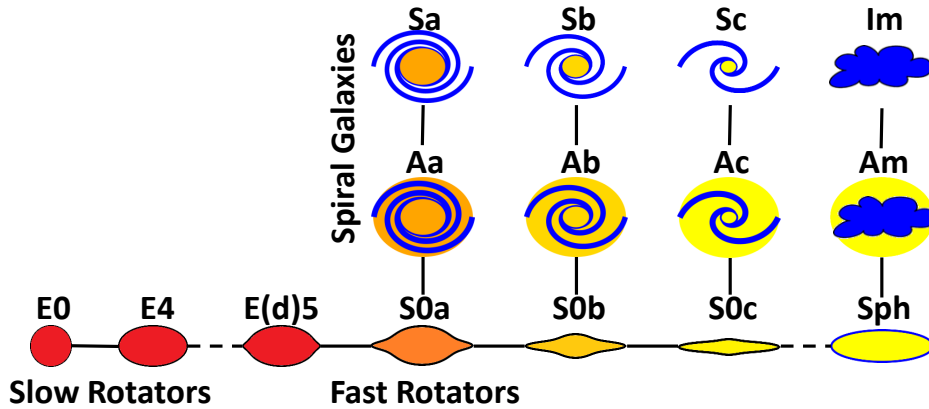


Figure 24

The “comb” morphology diagram. If all fast rotators could be seen edge-on, they would appear morphologically with a range of spheroid fractions ranging from thin S0s, to flat ellipticals with disky isophotes E(d) (Kormendy & Bender 1996), as here illustrated. The fast rotators ETGs form a parallel sequence to spiral galaxies as already emphasized, for the subset of S0 galaxies, by van den Bergh (1976), who proposed the above distinction into S0a–S0c. Fast rotators are intrinsically flatter than $\epsilon \gtrsim 0.4$ and span the same full range of shapes as spiral galaxies, including very thin disks. However very few Sa have spheroids as large as those of E(d) galaxies, indicating that bulges must grow in the transformation. The slow rotators are always rounder than $\epsilon \lesssim 0.4$ and have central cores in their surface brightness. On the right-hand side of the diagram we included spheroidal Sph galaxies, following Kormendy & Bender (2012). These are bulge-less dwarf galaxies, but are significantly rounder than S0c disks. The black solid lines connecting the galaxy images indicate an empirical continuity, while the dashed one emphasizes the dichotomy between the fast and slow rotator ETGs. (Adapted from Cappellari et al. 2011b, with the addition of Sph galaxies from Kormendy & Bender 2012).

4.4. Parallel sequencing of ETGs and spirals

The fast rotators are morphologically classified either E or S0 galaxies. All ETGs with photometric evidence for disks, including both the S0s and all galaxies classified as disky ellipticals E(d) by Bender et al. (1994), belong to the fast rotator, or counter-rotating disks class. The reverse is not true, because disks cannot be seen in the photometry at low inclination. However the dynamical models show that all apparently round and non disky fast rotators are inclined disks, and are intrinsically still quite flat (Cappellari et al. 2013a). This is also confirmed by statistical inversion of the observed shape distribution of the fast rotator class (Weijmans et al. 2014) (Section 3.3). This indicates that *all* fast rotators have disks and would be classified as either S0 or disky elliptical E(d) if they could be observed edge-on. The fast rotators, like S0 galaxies (Laurikainen et al. 2010; Kormendy & Bender 2012), span the full range of bulge fraction as spiral galaxies (Krajnović et al. 2013a), and include some extremely flat disks. They form a parallel sequence to spiral galaxies on scaling relations (Figure 23).

The slow rotators (or equivalently the non-regular rotators) are clearly different. They are never intrinsically flatter than $\epsilon \approx 0.4$ (Section 3.6.3). As a class, they are inconsistent with axisymmetry, as evidenced by kinematic twists (Section 3.3). They have cores or light deficits in their central surface brightness (Section 3.6.2), and their velocity fields are

qualitatively very different from simple JAM models.

All these arguments led [Cappellari et al. \(2011b\)](#) to propose a revision of [Hubble \(1936\)](#) classic tuning fork diagram. The new ATLAS^{3D} “comb” diagram combines elements from two previously proposed revisions to Hubble’s diagram with the new findings from IFS observations: (i) the parallelism between spiral galaxies and S0s in the revised classification diagram by [van den Bergh \(1976\)](#), (ii) the link between S0s and disk ellipticals in the diagram proposed by [Kormendy & Bender \(1996\)](#) and (iii) the distinction between slow and fast rotators, and the link of the latter with S0s, indicated by the IFS observations.

In the revised diagram ([Figure 24](#)) the ETGs are moved from the handle of the tuning fork to a parallel sequence to spiral galaxies. Contrary to previous diagrams, the proposed one is not a symmetric fork or trident, but rather an asymmetric “comb”. This is to emphasize the fact that many of the galaxy properties (e.g. stellar age and gas content) are shared by the two fast/slow families of ETGs, and mostly vary along the spiral sequence. The latter includes [van den Bergh \(1976\)](#) “anemic” spirals, to point out that the distinction between ETGs and spirals is not well defined and includes transition objects of uncertain classification. In some cases faint spiral arms become visible in ETGs with very deep optical ([Duc et al. 2011, 2015](#)) or HI observations ([Serra et al. 2012](#)).

The need for revising Hubble’s tuning-fork diagram, and the parallelism between S0 and spiral galaxies was also pointed out, based on photometric arguments, by [Kormendy & Bender \(2012\)](#). The main conceptual difference is that the ATLAS^{3D} diagram emphasizes the parallelism to spirals of the entire class of kinematically-classified fast rotators, not to S0 alone. Moreover, [Kormendy & Bender \(2012\)](#) extended the S0 sequence to include bulge-less spheroidal Sph galaxies. [Cappellari et al. \(2013a\)](#) reached a similar conclusion regarding Sph. We now also include Sph in [Figure 24](#). The similarity of the analysis and conclusions in the two independent studies is a demonstration of the robustness and relevance of the proposed parallelism.

5. ENVIRONMENTAL TRENDS

Galaxy environmental trends represent a vast subject with a long history. Here we only briefly mention some of the earliest works and again focus specifically on what integral-field spectroscopy specifically adds to this topic. For more general reviews, the reader is referred to [Blanton & Moustakas \(2009\)](#) and [Kormendy & Bender \(2012\)](#) for normal galaxies and to [Boselli & Gavazzi \(2014\)](#), for emphasis on the faint end of the galaxy luminosity.

5.1. Kinematic morphology-density relation

Large optical surveys of galaxy clusters in the 70’, discovered that that galaxy morphology significantly depends on environment ([Oemler 1974; Davis & Geller 1976; Melnick & Sargent 1977](#)). The classic work by [Dressler \(1980\)](#) revealed a nearly universal morphology-density $T - \Sigma$ relation, in which the fraction of spiral galaxies systematically decreases with increasing projected galaxy number density. This general trend was subsequently confirmed with samples of ever increasing size, reaching a peak with the Galaxy Zoo sample of 10^5 galaxies ([Bamford et al. 2009; Skibba et al. 2009](#)). The trend was found to hold over extended density ranges ([Postman & Geller 1984; Giovanelli et al. 1986](#)).

The $T - \Sigma$ relation is partly driven by the fact that galaxies become more massive in dense environments ([Kauffmann et al. 2004](#)), and galaxy mass drives galaxy properties.

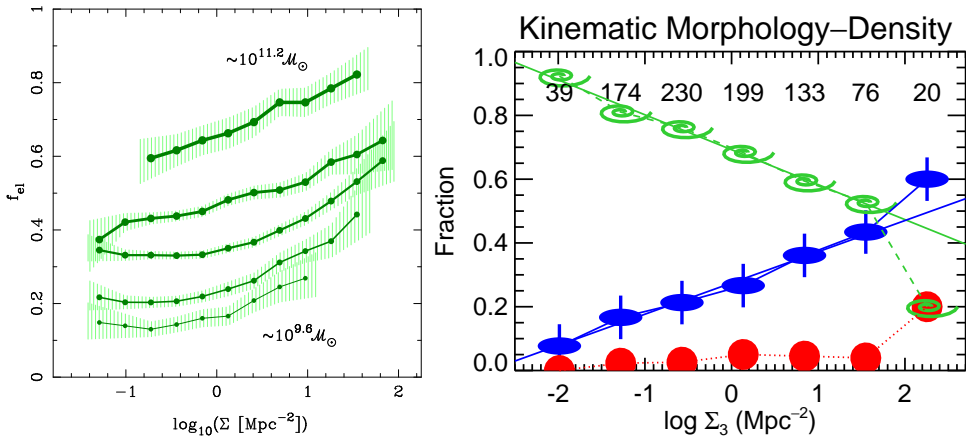


Figure 25

Photometric versus kinematic morphology-density. *Left panel:* The $T - \Sigma$ relation: the early-type fraction is plotted against local galaxy density for galaxies in selected narrow bins of stellar mass (from Bamford et al. 2009). *Right panel:* the $kT - \Sigma$ relation: for fast rotators (blue ellipse with vertical axis), slow rotators (red filled circle) and spiral galaxies (green spiral). The numbers above the symbols indicate the total number of galaxies in each density bin. This panel was adapted from Cappellari et al. (2011b), by including the $\varepsilon > 0.4$ criterion for slow rotators (Equation 19). A key difference between the environmental trends using morphological or kinematic classifications, is that in the former case, even at the lowest densities there is always a fraction $f(E) \gtrsim 10\%$ of (misclassified) elliptical galaxies, however in the latter case, the slow rotators are virtually absent in the lowest density environments $f(SR) \lesssim 2\%$.

However the $T - \Sigma$ relation is also clearly detectable at fixed mass (Bamford et al. 2009; Smith et al. 2012b; left panel of Figure 25) and this shows that purely environmental effects must play a role. In fact Peng et al. (2010) convincingly argued that the effect of mass and environment are separable and act independently in transforming galaxies and this naturally explain the existence of the Schechter (1976) luminosity function.

Studies of the $T - \Sigma$ later extended to larger redshift, thanks to the resolving power of the Hubble Space Telescope, which allowed for morphological classification to performed initially to $z \lesssim 0.5$ (e.g. Dressler et al. 1997; Fasano et al. 2000; Treu et al. 2003; Wilman et al. 2009) and later out to $z \lesssim 1$ (e.g. Stanford et al. 1998; van Dokkum et al. 2000; Smith et al. 2005; Postman et al. 2005; Cooper et al. 2006; Capak et al. 2007; Poggianti et al. 2008). These studies have found that the fraction of S0 galaxies in clusters decreases with redshift, while the fraction of spiral galaxies correspondingly increases. The trend is much reduced in the field (Dressler et al. 1997; Fasano et al. 2000; Postman et al. 2005; Smith et al. 2005). These results indicate that spiral galaxies become passive and transform into S0 due to the cluster environmental effects (Boselli & Gavazzi 2006). The morphological evolution is less significant at the largest galaxy masses, which indicates that these massive ellipticals were already passive from larger redshift and remain so during their evolution (Stanford et al. 1998; Postman et al. 2005; Tasca et al. 2009), while most of the observed evolution consists of a transformation of spirals into S0s (Smith et al. 2005; Moran et al. 2007).

Motivated by the results reviewed in Section 3, Cappellari et al. (2011b) introduced the

$T - \Sigma$: Relation between the morphology and environmental density

$kT - \Sigma$: Relation between the kinematic classification and environmental density

kinematic morphology-density relation $kT - \Sigma$, which uses the physically robust fast/slow rotator classification to replace the strongly inclination-dependent S0/E morphological classification. The key differences ([Figure 25 right](#)) between the kinematic and morphological relations are the following:

1. The genuinely spheroidal system, the slow rotators, namely the galaxies that would be classified as E from any direction, are essentially absent in the field. Considering the lowest three density bins, out of a statistically significant sample of 443 galaxies, only 2% are slow rotators. Slow rotators only play a significant role at the largest environmental density, which correspond to the center of cluster and groups. This contrasts with the fraction $f(E) \gtrsim 10\%$ of (misclassified) E which is inferred from morphological classification even at the lowest densities (e.g. [Dressler 1980](#), [Figure 25 left](#)). Given the small number statistics of slow rotators, it is revealing to see their actual distribution within clusters. [Figure 26](#) visualizes the clear tendency for slow rotators to be found either at the cluster center, or within local overdensities, due to infalling sub-cluster being assembled into the main cluster. This tendency has been seen in most clusters for which IFS data exist and where well-defined overdensities are present ([Cappellari et al. 2011b](#); [Cappellari 2013](#); [Houghton et al. 2013](#); [D'Eugenio et al. 2013](#); [Scott et al. 2014](#); [Fogarty et al. 2014](#)). It explains why the $T - \Sigma$ relation seems to work better than the $T - R$ relation, which uses the cluster-centric radius ([Dressler et al. 1997](#)).
2. Focusing only on the ETGs subset, the ratio $f(SR)/f(FR)$ between slow and fast rotators is *not* a simple or monotonic function of environment. Instead, the ratio is nearly constant outside clusters, while inside clusters it becomes a strong function of the local galaxy number density ([Cappellari et al. 2011b](#); [Houghton et al. 2013](#); [D'Eugenio et al. 2013](#); [Fogarty et al. 2014](#)). This shows that in the field, slow rotators are produced by random events, at an extremely low rate. While clusters are the natural place for the presence of slow rotators. They must form via a different process, which must be linked to the formation of the clusters themselves.

The study of the $kT - \Sigma$ relation has just recently started. The Virgo ([Cappellari et al. 2011b](#)) and Fornax ([Scott et al. 2014](#)) clusters are the only two which have currently been mapped by IFS observations with good completeness. With the currently small and generally incomplete samples, a few misclassified slow rotators (e.g. counter-rotating disks, recent mergers, or uncertain kinematics), can still significantly affect the conclusions. Moreover, ideally one would like to be able to recognize the genuine dry mergers relics: slow rotators with cores. But this is currently only possible with HST, and not much farther than the Coma cluster (100 Mpc). The situation is going to be revolutionized in the near future by IFS observations, thanks to the two large SAMI ([Bryant et al. 2015](#)) and MaNGA ([Bundy et al. 2015](#)) IFS surveys, which are expected to bring the study of the local $kT - \Sigma$ relation at the level of the $T - \Sigma$ one, in terms of number statistics and completeness.

5.2. Mass-size versus environment

In recent times, the $M - R_e$ relation ([Section 4.3](#)) has become one of the most popular observational constraints to galaxy formation models. This is because the variation of galaxy sizes during the hierarchical mass assembly of galaxies, depends sensitively on the detail by which the assembly occurs (e.g. [Nipoti et al. 2003](#); [Naab et al. 2009](#); [Bezanson et al. 2009](#);

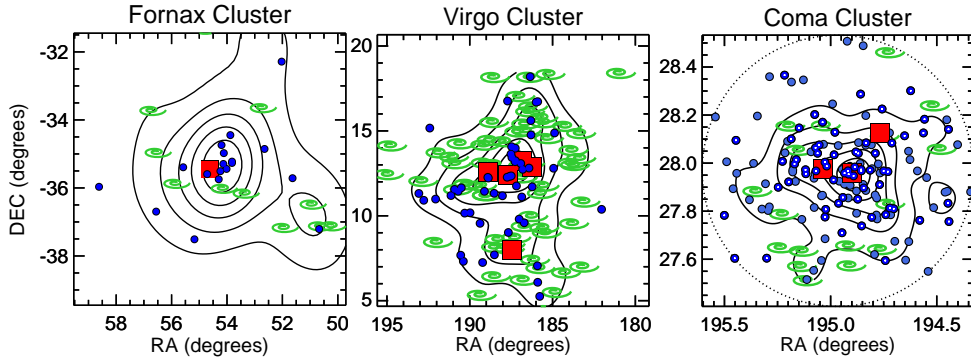


Figure 26

Slow rotators in clusters. *Left panel:* distribution of galaxies in the Fornax cluster of galaxies (Abell S0373). The red squares are the slow rotators with core, the blue circles are the rest of the ETGs and the green spirals are the spiral galaxies. A kernel density estimate for the galaxy distribution is overlaid with linearly spaced contours. This panel was adapted from Scott et al. (2014), with the main difference that the slow rotator NGC 1427 is not plotted in red because it is core-less (Lauer et al. 2007b). The only core slow rotator NGC 1399 sits near the peak of the cluster density. *Middle panel:* Same as in the left panel, for the Virgo cluster. Four core slow rotators are found very near the center of the main cluster A and one is M49 at the center the infalling sub-cluster B at the south of the center. *Right panel:* Same as in the left panel, for the Coma cluster (Abell 1656). The cluster is dominated by two massive core slow rotators near the peak density, while another lies along a slight overdensity. The last two panels are taken from Cappellari (2013). The samples in all three clusters are selected to be accurately complete down to the same luminosity $M_{K_s} < -21.5$ as the ATLAS^{3D} sample.

Hopkins et al. 2010). For example, using simple virial equilibrium arguments (Hausman & Ostriker 1978), one can show that during a gas-free merger of identical spherical galaxies on parabolic orbits, which is the most likely situation (Khochfar & Burkert 2006), the radius grows proportionally to the mass and the galaxy stellar velocity dispersion (integrated over the whole galaxy) remains unchanged (White 1983; Barnes 1992). However, when the mass growth happens via very small gas-poor satellites, then R is predicted to increase as the square of the mass fraction increase, while the σ decreases as the square root of the mass increase (Naab et al. 2009; Bezanson et al. 2009). These predictions properly capture the trends actually observed in detailed numerical simulations (Barnes 1992; Hernquist et al. 1993; Nipoti et al. 2003; Boylan-Kolchin et al. 2006; Naab et al. 2009).

In contrast, when gas is present, it dissipates energy, falls towards the center and forms stars in a compact star burst (Mihos & Hernquist 1994). Due to the shrinkage caused by the gas infall, the size of the remnant will increase more slowly than in the collisionless case, by an amount which is related to the amount of dissipation (e.g. Dekel & Cox 2006; Khochfar & Silk 2006). The galaxy center will be denser and will contain a steep inner profile (cusp or extra light) as observed in many fast rotators (Kormendy et al. 2009).

To test these predictions one would ideally like to be able to follow the redshift evolution of fast rotators and core slow rotators on the (M, R_e) plane. This is unfortunately not yet feasible, with the current generation of instruments. However, examining the environmental dependence is a good proxy to studying the redshift evolution. This is because at high redshift the abundance of massive halos declines and fewer galaxies live in clusters.

The environmental evolution of fast and slow rotators on the (M, R_e) plane was investigated by Cappellari (2013), using two extreme environments for which IFS data were available. The low-density sample was taken from the field/group environment of the ATLAS^{3D} sample, defined as not belonging to the Virgo cluster. The high-density sample used IFS data by Houghton et al. (2013) on the Coma cluster, which is the densest environment for which resolved spectroscopic observations can be currently taken. It has one of the largest, and carefully determined, dark halo virial masses of $M_{200} \approx 1.4 \times 10^{15} M_\odot$ (Lokas & Mamon 2003), that can be expected to be found in the whole Universe (e.g. Springel et al. 2005). Both samples were carefully selected to be nearly 100% complete to $M_{K_s} < -21.5$ ($M_* \gtrsim 6 \times 10^9 M_\odot$) and have fully homogeneous size and luminosity determinations from 2MASS (Skrutskie et al. 2006).

The study found that the mass-size distribution in the dense environment differs from the field/group one in two ways: (i) spiral galaxies are replaced by fast-rotator ETGs, which follow the *same* mass-size relation and have the *same* mass distribution as in the field sample; (ii) the core slow rotator ETGs are segregated in mass from the fast rotators, with their size increasing proportionally to their mass. A transition between the two processes appears around the stellar mass $M_{\text{crit}} \approx 2 \times 10^{11} M_\odot$. This is illustrated in Figure 21, which also includes the distribution of core slow rotators and fast rotators in the Virgo cluster, which has lower density than Coma and a virial halo mass more than 3× smaller of $M_{200} \approx 4 \times 10^{14} M_\odot$ (McLaughlin 1999). The distribution of galaxies on the Virgo (M, R_e) diagram is intermediate between the field/groups and Coma one. The core slow rotators have slightly larger masses than the field/groups ones and 4/5 lie above M_{crit} .

The environmental dependency of the distribution of spiral galaxies, fast rotators and core slow rotators, was interpreted as a direct evidence for the two channel for the build up of ETGs inferred from the distribution of galaxy properties in Section 4.3: (i) The bulge-growth and quenching route, is illustrated by the fact that spiral galaxies are gradually replaced by fast rotator, with smaller sizes and larger σ_e . The latter have the same properties as those in the field, but are simply more numerous in the cluster. (ii) The merger-growth route, is illustrated by the mass increase of the core slow rotators, with M_* increasing proportionally to R_e , broadly following the dry-merging model prediction.

The impressive universality of the mass-size relation for $M_* \lesssim M_{\text{crit}}$ in these two extreme environments is excellent agreement with other studies which used larger samples but lack IFS kinematic information. Differences between the sizes of ETGs in different environments are consistently found to be $\lesssim 10\%$, which is the level of than possible systematic effects in the size determinations or sample selections (Maltby et al. 2010; Huertas-Company et al. 2013; Poggianti et al. 2013; Fernández Lorenzo et al. 2013; Cebrián & Trujillo 2014).

The only significant difference between the low-density and high-density environments was found to be a slight asymmetry of the mass-size distribution. The peak is at the same location in the two environments, but there is a tail towards ETGs with larger sizes in clusters (Cappellari 2013; Delaix et al. 2014). In Coma, where galaxies are well resolved, this appear to be due to the well-known excess of passive disks in clusters (van den Bergh 1976; Wolf et al. 2009; Masters et al. 2010).

6. REDSHIFT EVOLUTION

Only the line emission from the gas-rich star-forming galaxies can be currently spatially resolved with IFS at significant redshift (e.g. Wisnioski et al. 2015; Stott et al. 2016).

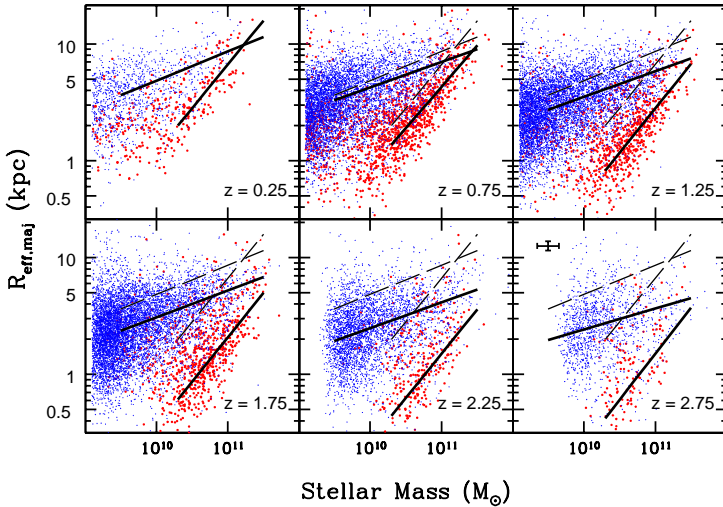


Figure 27

Evolution of the mass-size distribution. (M_*, R_e) distribution of colors-selected star forming and quiescent galaxies. The lines indicate model fits to the passive and star forming galaxies. The dashed lines, which are identical in each panel, represent the model fits to the galaxies in the lowest redshift bin. The solid lines represent fits to the higher-redshift samples. Strong evolution in the intercept of the size-mass relation is seen for passive galaxies and moderate evolution for the star forming ones. (Taken from [van der Wel et al. 2014](#))

This is because at $z \gtrsim 1.3$ most key spectral features are red-shifted to the near infrared, where the strong contribution of the OH atmospheric lines dramatically degrades the data quality. IFS observations of the stellar continuum in ETGs are essentially non-existing at these redshifts. For this reason this section will only include a brief overview of some of the key finding which closely relate to what has been discovered with IFS observations of nearby galaxies. A comprehensive review of the redshift evolution of galaxy structure was recently provided by [Conselice \(2014\)](#), while the evolution of their stellar population was reviewed by [Renzini \(2006\)](#).

6.1. Mass-size evolution

The stellar population of nearby ETGs, the scatter of the color-magnitude relation in clusters and the redshift evolution of their FP clearly indicate that ETGs formed their stars at $z \gtrsim 2$ ([Thomas et al. 2005](#); see review by [Renzini 2006](#)). When samples of spectroscopically-confirmed passive galaxies beyond $z \gtrsim 1.4$ were finally discovered, they appeared to have large masses $M_* \gtrsim 10^{11} M_\odot$, comparable to some of the most massive local ETGs ([Cimatti et al. 2004, 2006; Glazebrook et al. 2004](#)). However their sizes were found to be significantly smaller than their local counterparts ([Daddi et al. 2005; Trujillo et al. 2006a,b, 2007; Zirm et al. 2007; Toft et al. 2007; Longhetti et al. 2007; Cimatti et al. 2008; van Dokkum et al. 2008](#)).

Initial concerns about the possible effect of unresolved nuclear emission from AGNs,

strong stellar population gradients or inaccurate mass estimates, were cleared out via spectroscopic determinations of their velocity dispersion, which showed values broadly consistent (but with non-negligible size bias) with the virial predictions inferred from the given masses and radii (Cappellari et al. 2009; Cenarro & Trujillo 2009; Onodera et al. 2010; van de Sande et al. 2011, 2013; Toft et al. 2012; Bezanson et al. 2013; Belli et al. 2014).

It appears now well established that the *mean* size of ETGs grows significantly from $z \sim 3$ to the present day, while spiral galaxies grow at a smaller rate. The precise amount of this evolution depends sensitively on how ETGs are defined, given the strong dependence of galaxy size on their properties, like color, star formation, Sersic index or morphology (Figure 22, Newman et al. 2012; Cappellari et al. 2013a; Poggianti et al. 2013). The largest and most homogeneous study is currently the analysis of the CANDLES survey with extensive multi-band HST data (Grogan et al. 2011; Koekemoer et al. 2011) by van der Wel et al. (2014), reproduced in Figure 27. The slope of the $M_* - R_e$ relation for ETGs, for $M_* \gtrsim 3 \times 10^{10}$, is found to be consistent with the slope $M_* \propto R_e^{0.75}$ of the ZOE (Equation 25) over the whole redshift range $0 \lesssim z \lesssim 3$. Also apparent at all redshifts is a break in the overall mass-size, due to the minimum size of ETGs around a few $10^{10} M_\odot$, observed locally (see Figure 23).

The evolution of the distribution of galaxies on the (M_*, R_e) plane was interpreted by van Dokkum et al. (2015) using a simple statistical model which tries to capture the dominant mode of growth. They concluded that the population of ETGs progenitors likely followed two main simple evolutionary tracks in the (M_*, R_e) plane: (i) a shallow $\Delta \log R_e \sim 0.3 \Delta \log M_*$ growth dominated by gas accretion. Along these track the originally gas rich and star forming galaxies become denser, increasing their σ , until they reach a threshold at which their stars are quenched. (ii) A steeper track dominated by (mainly dry) mergers, where their size increase proportionally to their mass. An independent analysis of the CANDLES data, reaches quite similar conclusions, and also emphasizes the need for two similar formation channels for ETGs (Huertas-Company et al. 2015).

Although the detailed mechanism is still actively debated, from high-redshift observations, a consensus is emerging that galaxy quenching is linked to the growth of the galaxies *central* density, quantified using either photometrically-predicted σ (Franx et al. 2008; Bell et al. 2012; van Dokkum et al. 2015) or the stellar density Σ_1 within an aperture of radius $R = 1$ kpc (Cheung et al. 2012; Barro et al. 2015). Importantly, *central* density was found to be a much better predictor of quenching than other galaxy parameters and in particular galaxy mass. These findings are fully consistent with the link between bulge growth and quenching reviewed in Section 4.3 from IFS observations of local ETGs.

The two evolutionary channels described by van Dokkum et al. (2015) and Huertas-Company et al. (2015) from direct observations of the (M_*, R_e) redshift evolution and galaxy morphology, are the same that were also proposed to explain galaxy properties on the (M_*, R_e) plane using IFS observations in Section 4.3 and from the environmental dependency in Section 5.2. The remarkable agreement between these two sets of independent observations, based either on the fossil-record in nearby galaxies, or on redshift evolution, strengthens the conclusions of both complementary approaches.

6.2. Profile evolution

Using observations at different redshifts, one can directly trace the variation of the Sersic indices as a function of time. This analysis was performed for the progenitors of ETGs

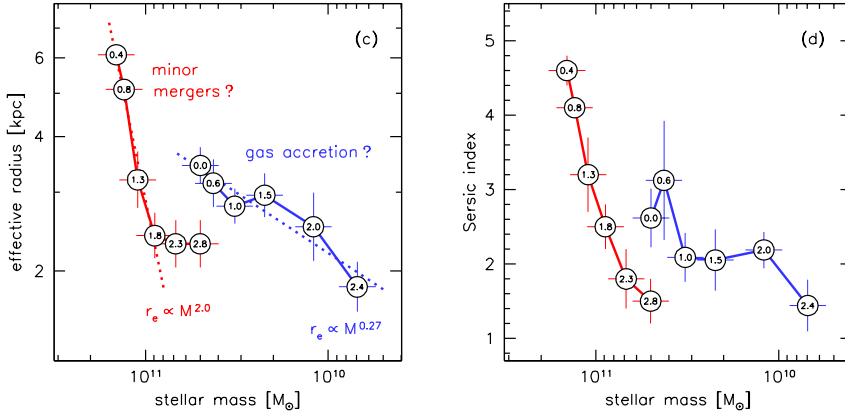


Figure 28

Size and profile evolution. R_e and Sersic index as a function of redshift and M_* . The blue line is for the progenitors of galaxies with present-day masses $M_* \approx 5 \times 10^{10} M_\odot$ while the red one is for present-day masses of $M_* \approx 3 \times 10^{11} M_\odot$. The less massive galaxies have undergone much less structural evolution than the present-day giant elliptical galaxies that populate the high-mass end of the mass function. (Taken from van Dokkum et al. 2013)

with present-day mass $M_* \approx 3 \times 10^{11} M_\odot$ by van Dokkum et al. (2010) and followed up with a consistent approach, but for progenitors with masses $M_* \approx 5 \times 10^{10} M_\odot$, by van Dokkum et al. (2013). The first set of galaxies have present-day masses above the critical mass $M_{\text{crit}} \approx 2 \times 10^{11} M_\odot$, dominated by the core slow rotators, while the second set have present-day masses near the break $M_b \approx 3 \times 10^{10}$ where spiral galaxies and fast rotators overlap, and slow rotators are absent.

The results, summarized in Figure 28, indicate that the progenitors of slow rotators grew rapidly in size, while those of fast rotators remained almost unchanged from $z \approx 2$. Similarly, the progenitors of slow rotators change little in mass from $z \sim 2$, while the progenitors of fast rotators still grow significantly (Muzzin et al. 2013). This mass and size growth difference is accompanied by a strikingly different behavior of the Sersic indices: both classes of galaxies start with disk-like $n \sim 1$, but the slow rotators progenitors rapidly increase their concentration, and reach $n \gtrsim 4$ near $z \sim 0$, while the fast rotators progenitors maintain a more constant Sersic index, with $z \sim 0$ values around 2–3, which is consistent with the typical value for the fast rotators in the ATLAS^{3D} sample (Krajnović et al. 2013a).

7. IMPLICATIONS FOR GALAXY FORMATION

The aim of this review is to provide an overview of the empirical signatures of galaxy formation in ETGs, as they were obtained mainly by IFS observations. Here we sketch ideas on galaxy formation driven by the observations we described. A detailed review of the theoretical models of the formation of ETGs is given by Somerville & Davé (2015) and Naab & Ostriker (ARA&A in preparation). Theoretical studies trying to specifically address the formation of the fast and slow rotator ETGs classes revealed by IFS observations were presented by Bois et al. (2011); Khochfar et al. (2011); Naab et al. (2014).

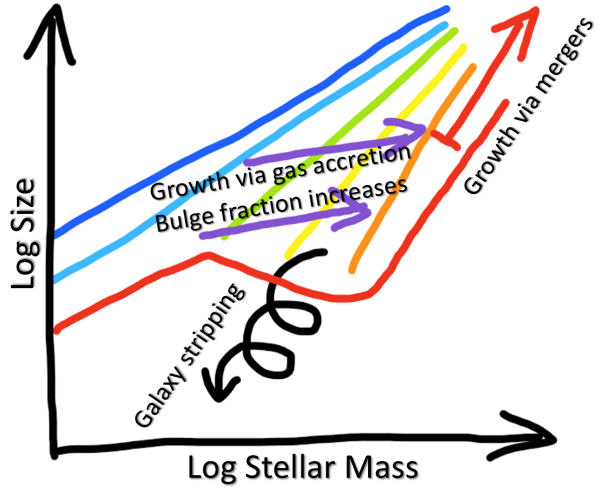


Figure 29

Galaxy evolution on the mass-size plane. Although the evolution of an individual galaxy is a complex combination of events, the observations indicate that the average evolution of ensembles of galaxies can be described by the following simple picture. The progenitors of fast rotators ETGs are star forming disks. They grow their mass, while slowly increasing their sizes, predominantly by gas accretion (purple lines). During this accretion they grow a bulge, which increases the likelihood for the galaxy to have its star formation quenched. They end up as bulge-dominated and passive fast rotators near the ZOE. Slow rotators build up most of their mass rapidly at high-z and subsequently grow mostly by gas poor (dry) merging, while varying their size nearly proportionally to their mass or more (red line). They end up in the top right of this diagram. The region below the ZOE is not empty: it includes ultra compact dwarfs (UCD), which are the likely cores of normal galaxies which had their envelopes stripped by the gravitational field of larger galaxies. (Based on fig. 15 of Cappellari et al. 2013a and fig. 28 of van Dokkum et al. 2015)

7.1. Galaxy evolution on the (M_*, R_e) plane

Consistently, from either the IFS results and from the high-redshift ones, one can describe the build up of ETGs on the (M_*, R_e) diagram as in Figure 29. The *average* growth of the overall ETGs population can be summarized has happening trough two main channels. **The first one is dominated by gas accretion.** Spiral galaxies accrete gas, or experience gas rich minor mergers. The gas sinks towards the center, increases the galaxy mass and at the same time builds a bulge. The presence of a bulge increases the **likelihood** for the galaxy to have its star formation quenched. This makes the progenitor spiral end up as a passive fast rotator ETG, with a stellar disk and, on average, a larger bulge fractions. As a result of this first channel, all galaxy properties related to the star formation history, vary on average along lines of nearly constant σ_e . The fact that, at fixed mass, dense bulges have α -enhanced stellar population (Figure 22) indicates that bulge formation must be a rapid process as expected during intense starbursts. The gas accretion and subsequent star formation leaves the metallicity enhancements of the disks in fast rotators as a fossil record (Figure 16).

The second channel on the (M_*, R_e) diagram is dominated by mostly-dry mergers, which move galaxies by increasing their size roughly proportionally to their mass, while leaving σ_e nearly unchanged. During dry mergers the stellar population evolves passively and varies

little for old systems. For this reason no significant trend is observed in galaxy properties related to the stellar population along this second channel. However dry mergers leave an imprint in the nuclear profiles, when supermassive black holes of the merging galaxies sink towards the center via dynamical friction and eject stars in radial orbits, scouring a nuclear core or deficit (e.g. [Faber et al. 1997](#); [Milosavljević & Merritt 2001](#); [Kormendy & Ho 2013](#)).

Observations indicate that fast and slow rotator predominantly follow either one or the other channel. A key piece of information is provided by the environmental distribution ([Section 5.1](#)). If slow rotators formed by dry merging of fast rotators: (i) they would roughly follow their distribution, like fast rotators follow the spiral distribution. Instead, their distribution in clusters is very different, with the slow rotators near the cluster/group centers and the fast rotators following spiral galaxies ([Figure 26](#)); (ii) moreover one would find core slow rotator along the whole sequence of passive ETGs, starting from $M_* \gtrsim 3 \times 10^{10} M_\odot$, as they are still building-up their mass, especially in the field. Instead they suddenly appear only above $M_* \gtrsim 10^{11} M_\odot$ ([Figure 21](#)).

We mention in passing, that the region of the (M_*, R_e) diagram below the ZOE, but for $M_* \lesssim 3 \times 10^{10} M_\odot$, is not actually devoid of stellar systems. It is populated by objects generally called dwarf ellipticals (dE) and ultra compact dwarfs (UCD) (e.g. [Misgeld & Hilker 2011](#); [Norris et al. 2014](#)). Evidence suggests they may be normal ETGs which fell well into the halo of a larger galaxy and had their outer stellar envelope stripped (e.g. [Drinkwater et al. 2003](#)). Integral-field observations of the kinematics and population of these galaxies have just started and appears to confirm this interpretation ([Ryś et al. 2014](#); [Guérou et al. 2015](#)). According to this picture, dE and UCD do not follow the main route of galaxy formation. This interesting topic will not be discussed in any detail here.

7.2. Hierarchical origins of fast and slow rotators ETGs

To understand how fast and slow rotators can follow separate evolutionary channels, one needs to consider [the hierarchical growth of galaxies and clusters](#) (e.g. [De Lucia et al. 2012](#); [Wilman & Erwin 2012](#)). According to our current understanding of galaxy formation (e.g. [Mo et al. 2010](#)), after the big bang, the primordial dark matter distribution is imprinted with small fluctuations and these inhomogeneities grow by gravitational instability to form dark matter halos. The [primordial gas falls into a nearby halo and loses energy by radiating some of its energy](#). For this reason it sinks towards the halo center and forms a rotating disk. When the gas becomes sufficiently denser that the halo, it collapses into small clumps due to radiative cooling and starts producing stars into stellar clusters.

The largest dark matter overdensities are able to acquire large amount of gas early-on, when they are still at the center of their own halo, dominating the overall gravitational potential. They quickly reach the critical mass above which [the infalling gas is shock heated by the halo gravitational field and have their star formation suppressed](#) ([Kereš et al. 2005](#); [Dekel & Birnboim 2006](#)). These massive galaxies are the progenitors of the slow rotators. The hot gas is actually observed in X-ray in local massive boxy E ([Bender et al. 1989](#)), in core galaxies ([Kormendy et al. 2009](#)) and in slow rotators in particular ([Sarzi et al. 2013](#)). When two groups merge, during the hierarchical build-up of galaxies and clusters, the central galaxies in the two groups, which sit at rest near the center of mass of the halo, will efficiently sink to the center of the resulting larger cluster/group of galaxies via dynamical friction. These massive slow rotator will efficiently merge, due to their large mass and small relative velocities, forming a more massive slow rotator with an inner core

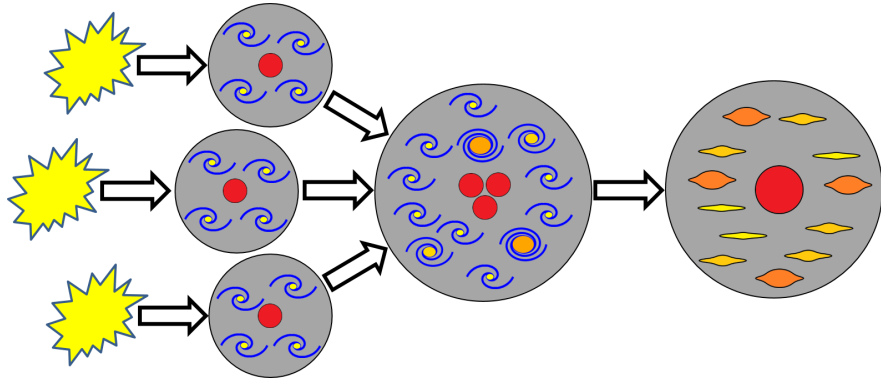


Figure 30

Hierarchical origin of fast and slow rotators. The progenitors of core slow rotators form in the high-redshift universe, at the center of the largest dark matter overdensities. They quickly grow above the critical mass required to be surrounded by a hot gaseous envelope which prevents further accretion. When groups merge to form massive clusters, slow rotators sink toward the center where they merge to form more massive slow rotators. The same cannot happen to fast rotators, which have masses too small to efficiently sink to the center and velocities too fast to merge. They are quenched by the cluster and from then on stop increasing their mass, but are only affected by tidal effects. Not included here is the internal quenching, which appears associated to the bulge growth and can act independently of environment.

scoured by the resulting black hole binary. In this way a typical slow rotator is able to remain as such for the rest of its evolution (Figure 30).

This picture is similar to the one that motivates the separation of “central” (i.e. the most massive) and “satellite” (i.e. the rest) galaxies in dark matter halos, when building theoretical descriptions of galaxy and halo properties (e.g., [Zheng et al. 2005](#); [Zehavi et al. 2005](#); [Conroy et al. 2006](#)). However in the theoretical approaches every halo has a single central galaxy, by definition. While in reality a given cluster, or a given massive dark matter halo, may contain a handful of slow rotators, which were central galaxies of their respective halos when they formed, but have yet to merge into a single object. For this reason the correspondence between central galaxies and slow rotators is only approximately correct.

The regions of lower dark matter density are unable to efficiently acquire gas and grow more slowly and gradually. They form disk galaxies, which at high redshift are observed to have high gas fractions ([Daddi et al. 2010](#); [Tacconi et al. 2010](#)), have large velocity dispersion, are turbulent compared to their local counterparts ([Förster Schreiber et al. 2006, 2009](#); [Genzel et al. 2006, 2008](#); [Law et al. 2012](#); [Kassin et al. 2012](#); [Stott et al. 2016](#)) and appear unstable to clump formation ([Elmegreen et al. 2007](#); [Genzel et al. 2011](#)). These clumps may sink toward the center and start forming the bulge ([Bournaud et al. 2007](#); [Dekel et al. 2009](#)), or the gas may simply spiral toward the nucleus to grow the bulge in starbursts. During the initial stages, when the velocity dispersion of their groups is quite small, gas rich mergers can also happen. Isolated spirals are able to sustain a nearly constant star formation for a long time, possibly with the contribution of the so called “cosmological fountain” effect ([Frernali & Binney 2008](#); [Frernali 2014](#)). During this phase they lie on the so-called star formation main sequence ([Brinchmann et al. 2004](#); [Salim et al. 2007](#)).

However the bulge growth (and σ_e or Σ_1 rise) increases the likelihood for the galaxy

to have its star formation quenched. Some form of feedback is observed to stop the star formation and make the galaxy passive. The link between bulge fraction (or central mass density) and quenching is currently unclear. Outflows from supernovae or from a central AGN (see Fabian 2012; Kormendy & Ho 2013; Heckman & Best 2014, for reviews) must both play a role (Silk & Rees 1998; Granato et al. 2004; Bower et al. 2006; Croton et al. 2006; Hopkins et al. 2006), as may the stabilizing effect of the bulge itself (Martig et al. 2009; Ceverino et al. 2010), which may contribute to the observed decrease of the star formation efficiency in ETGs (Saintonge et al. 2012; Martig et al. 2013; Davis et al. 2014). Evidence of feedback in action within a field fast rotator was presented in Alatalo et al. (2011). These forms of internal feedback are needed to produce fast rotators in the field.

But environment has a more dramatic effect. In fact, as soon as one of these disk galaxies is acquired by a large halo, its gravitational pull will be unable to acquire more gas, because their small halos will be orbiting at high speed within the ambient gas, which is at rest within the main halo. Moreover, at sufficiently high gas densities, their own gas, including their corona and fountain effect, will be stripped entirely (Boselli & Gavazzi 2006). As a result, when disk galaxies enter sufficiently massive clusters, they stop growing, due to both the lack of gas accretion and inability to merge because of the high relative velocities of satellites. The environment will now only act via tidal perturbations due to the high-speed encounters, by puffing up their disks (e.g. Moore et al. 1996). From then on, the galaxies will be ETGs fast rotators. Their masses will stop growing during subsequent mergers of the parent group/cluster, while slow rotators will continue to grow in mass following the first dry-merging channel. This additional growth of slow rotators during the merging of clusters/groups, tends to produce a gap between the mass distribution of the fast and slow rotators. It explains observed know gap in luminosity between the first ranked galaxy in a massive cluster, and the subsequently ranked galaxies (Sandage & Hardy 1973; Lauer et al. 2014), also clearly visible in Figure 21 (right panel).

This picture is broadly consistent will all observational evidences, but Nature is certainly not that simple. For example central galaxies in clusters are not always passive (Liu et al. 2012), however the small fraction of star forming ones is consistent with the general picture. Moreover the channel from star forming spirals to bulge-dominated passive fast rotators does not always progress monotonically in one direction. Rejuvenation events can happen in ETGs (Kaviraj et al. 2007) and specifically in fast rotators (Young et al. 2014). Moreover the gas versus stars misalignment indicates external accretion (Sarzi et al. 2006; Davis et al. 2011). Small fractions of neutral gas are detected in 40% of ETGs in the field, especially at large radii (Morganti et al. 2006; Oosterloo et al. 2010; Serra et al. 2012). And tidal tails are not uncommon also in fast rotators (Duc et al. 2011, 2015). Finally, all trends illustrated in Figure 22 have significant scatter. But the incidence of these events is fully consistent with the general picture we described. In particular, the IFS observations allow one to exclude a scenario in which passive fast rotators can acquire major amounts of gas and become star forming spirals again. These very bulge dominated spirals are extremely rare (e.g. the Sombrero galaxy M104). Moreover, if these events were common, they would erase the clear empirical inverse dependency between bulge fraction (or σ_e) and star formation indicators. Similarly one can exclude a scenario in which the slow rotators acquire a disk and become fast rotators. This is because the dynamics of bulges in fast rotators is well described by the simple axisymmetric JAM models over the whole mass range. This contrast with the strikingly different dynamics and shape of slow rotators, as revealed by the IFS data.

8. CONCLUSIONS

This review was written at an ideal time, when studies of ETGs using the first generation of IFS survey (SAURON [de Zeeuw et al. 2002](#), ATLAS^{3D} [Cappellari et al. 2011a](#) and CALIFA [Sánchez et al. 2012](#)), those targeting one galaxies at a time, were nearly complete. The second generation of IFS surveys (SAMI [Bryant et al. 2015](#) and MaNGA [Bundy et al. 2015](#)) just started but are actively acquiring data. A limited preview of the SAMI results was included in this review. At the same time, the new MUSE IFS ([Bacon et al. 2010](#)), on the 8.2-m Very Large Telescope of ESO, started pushing the envelope of the data quality one can achieve on nearby galaxies ([Emsellem et al. 2014](#); [Krajnović et al. 2015](#)).

For this reason, the goal of this review has been to define the status of our knowledge of the structure, kinematics and scaling relations of ETGs, before the arrival of these new large IFS survey. We aim to set a benchmark for assessing how much we have progressed.

Galaxy evolution can be studied via detailed observations in the nearby Universe or using evolutionary studies as a function of redshift. Too often the groups working in one or the other field are unaware of the results of the other and miss the opportunity of combining the two sets of information to advance our knowledge. This review tried to emphasize and illustrate the importance of a synergy between the two approaches.

In the near future, one will be able to combine our knowledge about ETGs from the upcoming multiplexed IFS survey, with the advances that the James Webb Space Telescope ([Gardner et al. 2006](#)) will bring, thanks to its ability of obtaining deep near-infrared spectra, including IFS (but not multiplexed), targeting the rest-frame optical spectra of ETGs, free of the atmospheric absorptions. This will provide clean kinematics and stellar population for ETGs out to the peak of their assembly epoch around $z \sim 2$.

In the more distant future, with the upcoming class of 40-m telescopes, like the European Extremely Large Telescope (E-ELT) and the Thirty Meter Telescope (TMT), coupled with multiplexed capabilities in the near-infrared it will become possible to perform IFS surveys like the ones we described here, out to $z \sim 2$. We can only be looking forward to witness those new developments.

SUMMARY POINTS

1. Using IFS kinematics, ETGs separate into two structurally homogeneous classes **with/without disks: the fast/slow rotators**. We showed that there is a dichotomy, not a smooth transition, between the two classes.
2. This dichotomy broadly agrees with the previously identified photometric separation into e.g. core/power-law ETGs. But the kinematic classification is nearly independent on inclination and does not require high spatial resolution. This makes it ideal for large IFS surveys.
3. IFS revealed a close link between ETGs and spirals. Below $M_{\text{crit}} \approx 2 \times 10^{11} M_{\odot}$, fast rotator ETGs form a parallel sequence in galaxy properties with spiral galaxies. While core slow rotators dominate above M_{crit} .
4. In the spirals to fast rotators sequence, suppression of star formation and molecular gas fraction are **driven by the central mass density slope, or bulge mass fraction**.
5. ETGs are dominated by stellar mass within R_e and their $(M_*/L)_{\text{dyn}}$ is mainly due to systematic variations in the stellar population, including the IMF.
6. The total mass density is well-described by $\rho_{\text{tot}} \propto r^{-2.2}$, from the center out to at

- least $4R_e$ with small scatter (in the currently explored mass range).
7. Slow rotators with cores are found near the centers of clusters/groups or subgroups within clusters. Fast rotators are distributed like spiral galaxies.
 8. IFS observations, and redshift evolution studies, consistently and independently indicate a scenario where the evolution of fast/slow rotators follows two distinct (i) gas-accretion driven and (ii) dry-merger driven, evolutionary channels.

FUTURE ISSUES

1. What are the trends in population and kinematics at radii well beyond $R \gtrsim 2R_e$? Much information on galaxy assembly is contained in the stellar halos.
2. What is the physical mechanism making galaxies passive? Large IFS surveys, of both spirals and ETGs, can answer this long-standing question by combining spatially-resolved gas and stellar observables with environment.
3. Do we understand stellar population and IMF in galaxies? Can we reliably predict stellar masses from spectra, or are there fundamental unsolved issues?
4. What are the trends in *total* density profiles at large radii where dark matter dominates? How do they relate to spirals? And to detailed model predictions?
5. How do spatially-resolved population and kinematics evolve with redshift? Can we directly trace the assembly of mass and metals over time?
6. Can we follow the dark halo growth as a function of time using resolved IFS of the stars and gas dynamics?

DISCLOSURE STATEMENT

The author is not aware of any affiliations, memberships, funding, or financial holdings that might be perceived as affecting the objectivity of this review.

ACKNOWLEDGMENTS

Many of the ideas presented in this review, originated during more than a decade of enjoyable and productive collaboration, initially with the SAURON team and subsequently with the ATLAS^{3D} collaboration. I acknowledge with gratitude the numerous meetings and enlightening discussions with the members of the two teams. I am most grateful to my Scientific Editor John Kormendy and co-editor Sandy Faber for fruitful discussions and comments. I have been fortunate to be able to benefit from their insights and unique expertise on this subject. It is a particular pleasure to thank Eric Emsellem, Davor Krajnović and Tim de Zeeuw for thoughtful suggestions. I thank Jesús Falcón-Barroso for providing the CALIFA ($\lambda_{R_e}, \varepsilon$) values. I acknowledge support from a Royal Society University Research Fellowship. I warmly thank my wife Christi Warner for making this review possible with her constant support and understanding.

LITERATURE CITED

- Aihara H, Allende Prieto C, An D, et al. 2011. *Ap. J. Suppl.* 193:29
- Alatalo K, Blitz L, Young LM, et al. 2011. *Ap. J.* 735:88
- Andredakis YC, Peletier RF, Balcells M. 1995. *MNRAS* 275:874
- Arnold JA, Romanowsky AJ, Brodie JP, et al. 2014. *Ap. J.* 791:80
- Auger MW, Treu T, Bolton AS, et al. 2010a. *Ap. J.* 724:511–525
- Auger MW, Treu T, Gavazzi R, et al. 2010b. *Ap. J. Let.* 721:L163–L167
- Bacon R, Accardo M, Adjali L, et al. 2010. In *Ground-based and Airborne Instrumentation for Astronomy III*, eds. IS McLean, SK Ramsay, H Takami, 8. vol. 7735 of *SPIE Conference Series*
- Bacon R, Adam G, Baranne A, et al. 1995. *Astron. Astrophys. Suppl.* 113:347
- Bacon R, Copin Y, Monnet G, et al. 2001. *MNRAS* 326:23–35
- Bamford SP, Nichol RC, Baldry IK, et al. 2009. *MNRAS* 393:1324–1352
- Barnabè M, Czoske O, Koopmans LVE, Treu T, Bolton AS. 2011. *MNRAS* 415:2215–2232
- Barnes JE. 1992. *Ap. J.* 393:484–507
- Barro G, Faber SM, Koo DC, et al. 2015. *ApJ submitted (arXiv:1509.00469)*
- Bastian N, Covey KR, Meyer MR. 2010. *Annu. Rev. Astron. Astrophys.* 48:339–389
- Begeman KG. 1989. *Astron. Astrophys.* 223:47–60
- Behroozi PS, Conroy C, Wechsler RH. 2010. *Ap. J.* 717:379–403
- Bell EF, van der Wel A, Papovich C, et al. 2012. *Ap. J.* 753:167
- Belli S, Newman AB, Ellis RS. 2014. *Ap. J.* 783:117
- Bender R. 1988. *Astron. Astrophys.* 193:L7–L10
- Bender R, Burstein D, Faber SM. 1992. *Ap. J.* 399:462–477
- Bender R, Doebeleiner S, Moellenhoff C. 1988. *Astron. Astrophys. Suppl.* 74:385–426
- Bender R, Saglia RP, Gerhard OE. 1994. *MNRAS* 269:785
- Bender R, Surma P, Doebeleiner S, Moellenhoff C, Madejsky R. 1989. *Astron. Astrophys.* 217:35–43
- Bendinelli O. 1991. *Ap. J.* 366:599–604
- Bernardi M, Roche N, Shankar F, Sheth RK. 2011. *MNRAS* 412:L6–L10
- Bernardi M, Shankar F, Hyde JB, et al. 2010. *MNRAS* 404:2087–2122
- Bernardi M, Sheth RK, Annis J, et al. 2003. *Astron. J.* 125:1866–1881
- Bershady MA, Verheijen MAW, Swaters RA, et al. 2010. *Ap. J.* 716:198–233
- Bertin G, Ciotti L, Del Principe M. 2002. *Astron. Astrophys.* 386:149–168
- Bertola F, Capaccioli M. 1975. *Ap. J.* 200:439–445
- Bezanson R, van Dokkum PG, Tal T, et al. 2009. *Ap. J.* 697:1290–1298
- Bezanson R, van Dokkum PG, van de Sande J, et al. 2013. *Ap. J. Let.* 779:L21
- Binggeli B, Sandage A, Tarenghi M. 1984. *Astron. J.* 89:64–82
- Binney J. 1978. *MNRAS* 183:501–514
- Binney J. 2005. *MNRAS* 363:937–942
- Binney J, de Vaucouleurs G. 1981. *MNRAS* 194:679–691
- Binney J, Tremaine S. 2008. *Galactic Dynamics: Second Edition*. Princeton, NJ: Princeton University Press
- Blanton MR, Moustakas J. 2009. *Annu. Rev. Astron. Astrophys.* 47:159–210
- Blanton MR, Roweis S. 2007. *Astron. J.* 133:734–754
- Blumenthal GR, Faber SM, Primack JR, Rees MJ. 1984. *Nature* 311:517–525
- Bois M, Emsellem E, Bournaud F, et al. 2011. *MNRAS* 416:1654
- Bolton AS, Burles S, Koopmans LVE, Treu T, Moustakas LA. 2006. *Ap. J.* 638:703–724
- Bolton AS, Burles S, Treu T, Koopmans LVE, Moustakas LA. 2007. *Ap. J. Let.* 665:L105–L108
- Borriello A, Salucci P, Danese L. 2003. *MNRAS* 341:1109–1120
- Boselli A, Gavazzi G. 2006. *Pub. Astron. Soc. Pac.* 118:517–559
- Boselli A, Gavazzi G. 2014. *Astron. Astrophys. Rev.* 22:74
- Bosma A. 1978. *The distribution and kinematics of neutral hydrogen in spiral galaxies of various morphological types*. Ph.D. thesis, Groningen Univ.

- Bournaud F, Elmegreen BG, Elmegreen DM. 2007. *Ap. J.* 670:237–248
- Bower RG, Benson AJ, Malbon R, et al. 2006. *MNRAS* 370:645–655
- Boylan-Kolchin M, Ma CP, Quataert E. 2006. *MNRAS* 369:1081–1089
- Brinchmann J, Charlot S, White SDM, et al. 2004. *MNRAS* 351:1151–1179
- Brodie JP, Romanowsky AJ, Strader J, et al. 2014. *Ap. J.* 796:52
- Bruzual G, Charlot S. 2003. *MNRAS* 344:1000–1028
- Bryant JJ, Owers MS, Robotham ASG, et al. 2015. *MNRAS* 447:2857–2879
- Bundy K, Bershady MA, Law DR, et al. 2015. *Ap. J.* 798:7
- Burbidge EM, Burbidge GR, Prendergast KH. 1959. *Ap. J.* 130:739
- Burstein D, Bender R, Faber S, Nolthenius R. 1997. *Astron. J.* 114:1365
- Byun YI, Grillmair CJ, Faber SM, et al. 1996. *Astron. J.* 111:1889
- Caon N, Capaccioli M, D’Onofrio M. 1993. *MNRAS* 265:1013
- Capaccioli M. 1989. In *World of Galaxies*, eds. HG Corwin Jr., L Bottinelli, 208–227. New York: Springer-Verlag
- Capak P, Abraham RG, Ellis RS, et al. 2007. *Ap. J. Suppl.* 172:284–294
- Cappellari M. 2002. *MNRAS* 333:400–410
- Cappellari M. 2008. *MNRAS* 390:71–86
- Cappellari M. 2013. *Ap. J. Let.* 778:L2
- Cappellari M, Bacon R, Bureau M, et al. 2006. *MNRAS* 366:1126–1150
- Cappellari M, Copin Y. 2003. *MNRAS* 342:345–354
- Cappellari M, di Serego Alighieri S, Cimatti A, et al. 2009. *Ap. J. Let.* 704:L34–L39
- Cappellari M, Emsellem E. 2004. *Pub. Astron. Soc. Pac.* 116:138–147
- Cappellari M, Emsellem E, Bacon R, et al. 2007. *MNRAS* 379:418–444
- Cappellari M, Emsellem E, Krajnović D, et al. 2011a. *MNRAS* 413:813
- Cappellari M, Emsellem E, Krajnović D, et al. 2011b. *MNRAS* 416:1680
- Cappellari M, McDermid RM. 2005. *Classical and Quantum Gravity* 22:347
- Cappellari M, McDermid RM, Alatalo K, et al. 2012. *Nature* 484:485–488
- Cappellari M, McDermid RM, Alatalo K, et al. 2013a. *MNRAS* 432:1862–1893
- Cappellari M, Romanowsky AJ, Brodie JP, et al. 2015. *Ap. J. Let.* 804:L21
- Cappellari M, Scott N, Alatalo K, et al. 2013b. *MNRAS* 432:1709–1741
- Cappellari M, Verolme EK, van der Marel RP, et al. 2002. *Ap. J.* 578:787–805
- Carollo CM, Schiavon P, Renzini A, et al. 2013. *Ap. J.* 773:112
- Carollo CM, Danziger IJ. 1994. *MNRAS* 270:523
- Carollo CM, Franx M, Illingworth GD, Forbes DA. 1997. *Ap. J.* 481:710–734
- Carter D. 1978. *MNRAS* 182:797
- Cebrián M, Trujillo I. 2014. *MNRAS* 444:682–699
- Cenarro AJ, Trujillo I. 2009. *Ap. J. Let.* 696:L43–L47
- Ceverino D, Dekel A, Bournaud F. 2010. *MNRAS* 404:2151–2169
- Chabrier G. 2003. *Pub. Astron. Soc. Pac.* 115:763–795
- Cheung E, Faber SM, Koo DC, et al. 2012. *Ap. J.* 760:131
- Cid Fernandes R, Mateus A, Sodré L, Stasińska G, Gomes JM. 2005. *MNRAS* 358:363–378
- Cimatti A, Cassata P, Pozzetti L, et al. 2008. *Astron. Astrophys.* 482:21–42
- Cimatti A, Daddi E, Renzini A. 2006. *Astron. Astrophys.* 453:L29–L33
- Cimatti A, Daddi E, Renzini A, et al. 2004. *Nature* 430:184–187
- Ciotti L. 1991. *Astron. Astrophys.* 249:99–106
- Ciotti L, Lanzoni B, Renzini A. 1996. *MNRAS* 282:1–12
- Colless M, Saglia RP, Burstein D, et al. 2001. *MNRAS* 321:277–305
- Conroy C. 2013. *Annu. Rev. Astron. Astrophys.* 51:393–455
- Conroy C, Dutton AA, Graves GJ, Mendel JT, van Dokkum PG. 2013. *Ap. J. Let.* 776:L26
- Conroy C, van Dokkum P. 2012a. *Ap. J.* 747:69
- Conroy C, van Dokkum PG. 2012b. *Ap. J.* 760:71

- Conroy C, Wechsler RH, Kravtsov AV. 2006. *Ap. J.* 647:201–214
- Conselice CJ. 2006. *MNRAS* 373:1389–1408
- Conselice CJ. 2014. *Annu. Rev. Astron. Astrophys.* 52:291–337
- Contopoulos G. 1956. *Zeitschrift für Astrophys.* 39:126
- Cooper MC, Newman JA, Croton DJ, et al. 2006. *MNRAS* 370:198–212
- Côté P, Ferrarese L, Jordán A, et al. 2007. *Ap. J.* 671:1456–1465
- Courteau S, Cappellari M, de Jong RS, et al. 2014. *Reviews of Modern Physics* 86:47–119
- Crane P, Stiavelli M, King IR, et al. 1993. *Astron. J.* 106:1371–1393
- Croton DJ, Springel V, White SDM, et al. 2006. *MNRAS* 365:11–28
- Daddi E, Bournaud F, Walter F, et al. 2010. *Ap. J.* 713:686–707
- Daddi E, Renzini A, Pirzkal N, et al. 2005. *Ap. J.* 626:680–697
- Davies RL, Efstathiou G, Fall SM, Illingworth G, Schechter PL. 1983. *Ap. J.* 266:41–57
- Davies RL, Kuntschner H, Emsellem E, et al. 2001. *Ap. J. Let.* 548:L33–L36
- Davies RL, Sadler EM, Peletier RF. 1993. *MNRAS* 262:650–680
- Davis M, Geller MJ. 1976. *Ap. J.* 208:13–19
- Davis TA, Alatalo K, Sarzi M, et al. 2011. *MNRAS* 417:882
- Davis TA, Young LM, Crocker AF, et al. 2014. *MNRAS* 444:3427–3445
- de Jong RS. 1996. *Astron. Astrophys.* 313:45–64
- de Lorenzi F, Gerhard O, Coccato L, et al. 2009. *MNRAS* 395:76–96
- de Lorenzi F, Gerhard O, Saglia RP, et al. 2008. *MNRAS* 385:1729–1748
- De Lucia G, Weinmann S, Poggianti BM, Aragón-Salamanca A, Zaritsky D. 2012. *MNRAS* 423:1277–1292
- de Rijcke S, Michielsen D, Dejonghe H, Zeilinger WW, Hau GKT. 2005. *Astron. Astrophys.* 438:491–505
- de Vaucouleurs G. 1948. *Annales d’Astrophysique* 11:247
- de Vaucouleurs G. 1959. *Handbuch der Physik* 53:275
- de Vaucouleurs G. 1963. *Ap. J. Suppl.* 8:31
- de Vaucouleurs G, de Vaucouleurs A, Corwin Jr. HG, et al. 1991. *Third Reference Catalogue of Bright Galaxies*. Berlin: Springer-Verlag
- de Zeeuw PT, Bureau M, Emsellem E, et al. 2002. *MNRAS* 329:513–530
- Deason AJ, Belokurov V, Evans NW, McCarthy IG. 2012. *Ap. J.* 748:2
- Dekel A, Birnboim Y. 2006. *MNRAS* 368:2–20
- Dekel A, Cox TJ. 2006. *MNRAS* 370:1445–1453
- Dekel A, Sari R, Ceverino D. 2009. *Ap. J.* 703:785–801
- Delaye L, Huertas-Company M, Mei S, et al. 2014. *MNRAS* 441:203–223
- D’Eugenio F, Houghton RCW, Davies RL, Dalla Bontà E. 2013. *MNRAS* 429:1258–1266
- Djorgovski S, Davis M. 1987. *Ap. J.* 313:59–68
- D’Onofrio M, Capaccioli M, Caon N. 1994. *MNRAS* 271:523
- Dressler A. 1980. *Ap. J.* 236:351–365
- Dressler A, Lynden-Bell D, Burstein D, et al. 1987. *Ap. J.* 313:42–58
- Dressler A, Oemler Jr. A, Couch WJ, et al. 1997. *Ap. J.* 490:577
- Drinkwater MJ, Gregg MD, Hilker M, et al. 2003. *Nature* 423:519–521
- Duc PA, Cuillandre JC, Karabal E, et al. 2015. *MNRAS* 446:120–143
- Duc PA, Cuillandre JC, Serra P, et al. 2011. *MNRAS* 417:863
- Dutton AA, Macciò AV, Mendel JT, Simard L. 2013. *MNRAS* 432:2496–2511
- Dutton AA, Treu T. 2014. *MNRAS* 438:3594–3602
- Elmegreen DM, Elmegreen BG, Ravindranath S, Coe DA. 2007. *Ap. J.* 658:763–777
- Emsellem E, Bacon R, Monnet G, Poulain P. 1996. *Astron. Astrophys.* 312:777–796
- Emsellem E, Cappellari M, Krajnović D, et al. 2011. *MNRAS* 414:888
- Emsellem E, Cappellari M, Krajnović D, et al. 2007. *MNRAS* 379:401–417
- Emsellem E, Cappellari M, Peletier RF, et al. 2004. *MNRAS* 352:721–743

- Emsellem E, Dejonghe H, Bacon R. 1999. *MNRAS* 303:495–514
- Emsellem E, Krajnović D, Sarzi M. 2014. *MNRAS* 445:L79–L83
- Emsellem E, Monnet G, Bacon R. 1994. *Astron. Astrophys.* 285:723–738
- Evans NW, Collett JL. 1994. *Ap. J. Let.* 420:L67–L70
- Faber SM, Dressler A, Davies RL, Burstein D, Lynden-Bell D. 1987. In *Nearly Normal Galaxies. From the Planck Time to the Present*, ed. SM Faber, 175–183. New York: Springer-Verlag
- Faber SM, Jackson RE. 1976. *Ap. J.* 204:668–683
- Faber SM, Tremaine S, Ajhar EA, et al. 1997. *Astron. J.* 114:1771
- Fabian AC. 2012. *Annu. Rev. Astron. Astrophys.* 50:455–489
- Falcón-Barroso J, Lyubenova M, van de Ven G. 2015. In *Galaxy Masses as Constraints of Formation Models*, eds. M Cappellari, S Courteau, 78–81. vol. 311 of *IAU Symposium*, Cambridge: Cambridge Univ. Press
- Falcón-Barroso J, van de Ven G, Peletier RF, et al. 2011. *MNRAS* 417:1787–1816
- Fang JJ, Faber SM, Koo DC, Dekel A. 2013. *Ap. J.* 776:63
- Fasano G, Poggianti BM, Couch WJ, et al. 2000. *Ap. J.* 542:673–683
- Fasano G, Vio R. 1991. *MNRAS* 249:629–633
- Fernández Lorenzo M, Sulentic J, Verdes-Montenegro L, Argudo-Fernández M. 2013. *MNRAS* 434:325–335
- Ferrarese L, Côté P, Jordán A, et al. 2006. *Ap. J. Suppl.* 164:334–434
- Ferrarese L, Merritt D. 2000. *Ap. J. Let.* 539:L9–L12
- Ferrarese L, van den Bosch FC, Ford HC, Jaffe W, O’Connell RW. 1994. *Astron. J.* 108:1598–1609
- Ferreras I, La Barbera F, de la Rosa IG, et al. 2013. *MNRAS* 429:L15–L19
- Fogarty LMR, Scott N, Owers MS, et al. 2014. *MNRAS* 443:485–503
- Fogarty LMR, Scott N, Owers MS, et al. 2015. *MNRAS* 454:2050–2066
- Forbes DA, Lasky P, Graham AW, Spitler L. 2008. *MNRAS* 389:1924–1936
- Forbes DA, Ponman TJ, Brown RJN. 1998. *Ap. J. Let.* 508:L43–L46
- Forestell AD, Gebhardt K. 2010. *Ap. J.* 716:370–383
- Förster Schreiber NM, Genzel R, Bouché N, et al. 2009. *Ap. J.* 706:1364–1428
- Förster Schreiber NM, Genzel R, Lehnert MD, et al. 2006. *Ap. J.* 645:1062–1075
- Foster C, Arnold JA, Forbes DA, et al. 2013. *MNRAS* 435:3587–3591
- Franx M, Illingworth G. 1990. *Ap. J. Let.* 359:L41–L45
- Franx M, Illingworth G, de Zeeuw T. 1991. *Ap. J.* 383:112–134
- Franx M, Illingworth G, Heckman T. 1989. *Astron. J.* 98:538–576
- Franx M, Illingworth GD. 1988. *Ap. J. Let.* 327:L55–L59
- Franx M, van Dokkum PG, Schreiber NMF, et al. 2008. *Ap. J.* 688:770–788
- Fraternali F. 2014. In *Setting the scene for Gaia and LAMOST - the current and next generations of surveys and models*, eds. S Feltzing, G Zhao, NA Walton, P Whitelock, 228–239. vol. 298 of *IAU Symposium*, Cambridge: Cambridge Univ. Press
- Fraternali F, Binney JJ. 2008. *MNRAS* 386:935–944
- Gardner JP, Mather JC, Clampin M, et al. 2006. *Space Sci. Rev.* 123:485–606
- Gavazzi R, Treu T, Rhodes JD, et al. 2007. *Ap. J.* 667:176–190
- Gebhardt K, Bender R, Bower G, et al. 2000a. *Ap. J. Let.* 539:L13–L16
- Gebhardt K, Richstone D, Kormendy J, et al. 2000b. *Astron. J.* 119:1157–1171
- Gebhardt K, Richstone D, Tremaine S, et al. 2003. *Ap. J.* 583:92–115
- Geha M, Blanton MR, Yan R, Tinker JL. 2012. *Ap. J.* 757:85
- Genzel R, Burkert A, Bouché N, et al. 2008. *Ap. J.* 687:59–77
- Genzel R, Newman S, Jones T, et al. 2011. *Ap. J.* 733:101
- Genzel R, Tacconi LJ, Eisenhauer F, et al. 2006. *Nature* 442:786–789
- Gerhard O. 1996. In *Spiral Galaxies in the Near-IR*, eds. D Minniti, HW Rix, 138. Berlin: Springer-Verlag
- Gerhard O. 2013. In *The Intriguing Life of Massive Galaxies*, eds. D Thomas, A Pasquali, I Ferreras,

- 211–220. vol. 295 of *IAU Symp.*, Cambridge: Cambridge Univ. Press
- Gerhard O, Jeske G, Saglia RP, Bender R. 1998. *MNRAS* 295:197
- Gerhard O, Kronawitter A, Saglia RP, Bender R. 2001. *Astron. J.* 121:1936–1951
- Gerhard OE, Binney JJ. 1996. *MNRAS* 279:993
- Giavalisco M, Ferguson HC, Koekemoer AM, et al. 2004. *Ap. J. Let.* 600:L93–L98
- Giovanelli R, Haynes MP, Chincarini GL. 1986. *Ap. J.* 300:77–92
- Glass L, Ferrarese L, Côté P, et al. 2011. *Ap. J.* 726:31
- Glazebrook K, Abraham RG, McCarthy PJ, et al. 2004. *Nature* 430:181–184
- Gnedin OY, Kravtsov AV, Klypin AA, Nagai D. 2004. *Ap. J.* 616:16–26
- González Delgado RM, García-Benito R, Pérez E, et al. 2015. *Astron. Astrophys.* 581:A103
- Graham A, Colless M. 1997. *MNRAS* 287:221–239
- Graham AW. 2001. *Astron. J.* 121:820–840
- Graham AW. 2012. *Ap. J.* 746:113
- Graham AW. 2013. In *Planets, Stars and Stellar Systems. Volume 6: Extragalactic Astronomy and Cosmology*, eds. TD Oswalt, WC Keel, 91. Berlin: Springer
- Graham AW, Erwin P, Trujillo I, Asensio Ramos A. 2003. *Astron. J.* 125:2951–2963
- Graham AW, Guzmán R. 2003. *Astron. J.* 125:2936–2950
- Graham AW, Worley CC. 2008. *MNRAS* 388:1708–1728
- Granato GL, De Zotti G, Silva L, Bressan A, Danese L. 2004. *Ap. J.* 600:580–594
- Graves GJ, Faber SM, Schiavon RP. 2009. *Ap. J.* 698:1590–1608
- Greene JE, Janish R, Ma CP, et al. 2015. *Ap. J.* 807:11
- Grogan NA, Kocevski DD, Faber SM, et al. 2011. *Ap. J. Suppl.* 197:35
- Guérout A, Emsellem E, McDermid RM, et al. 2015. *Ap. J.* 804:70
- Guo Q, White S, Li C, Boylan-Kolchin M. 2010. *MNRAS* 404:1111–1120
- Häring N, Rix HW. 2004. *Ap. J. Let.* 604:L89–L92
- Hausman MA, Ostriker JP. 1978. *Ap. J.* 224:320–336
- Heckman TM, Best PN. 2014. *Annu. Rev. Astron. Astrophys.* 52:589–660
- Hernquist L, Spergel DN, Heyl JS. 1993. *Ap. J.* 416:415
- Hogg DW. 1999. *e-print (astro-ph/9905116)*
- Hopkins PF, Bundy K, Hernquist L, Wuyts S, Cox TJ. 2010. *MNRAS* 401:1099–1117
- Hopkins PF, Hernquist L, Cox TJ, et al. 2006. *Ap. J. Suppl.* 163:1–49
- Houghton RCW, Davies RL, D'Eugenio F, et al. 2013. *MNRAS* 436:19–33
- Hubble EP. 1926. *Ap. J.* 64:321–369
- Hubble EP. 1936. *Realm of the Nebulae*. Yale Univ. Press, New Haven
- Hudson MJ, Lucey JR, Smith RJ, Steel J. 1997. *MNRAS* 291:488
- Huertas-Company M, Mei S, Shankar F, et al. 2013. *MNRAS* 428:1715–1742
- Huertas-Company M, Pérez-González PG, Mei S, et al. 2015. *Ap. J.* 809:95
- Humphrey PJ, Buote DA. 2010. *MNRAS* 403:2143–2151
- Hyde JB, Bernardi M. 2009. *MNRAS* 394:1978–1990
- Illingworth G. 1977. *Ap. J. Let.* 218:L43–L47
- Jeans JH. 1915. *MNRAS* 76:70–84
- Jeans JH. 1922. *MNRAS* 82:122–132
- Jedrzejewski R, Schechter PL. 1988. *Ap. J. Let.* 330:L87–L91
- Jedrzejewski RI. 1987. *MNRAS* 226:747–768
- Jimmy, Tran KV, Brough S, et al. 2013. *Ap. J.* 778:171
- Jorgensen I, Franx M, Kjaergaard P. 1996. *MNRAS* 280:167–185
- Kassin SA, Weiner BJ, Faber SM, et al. 2012. *Ap. J.* 758:106
- Kauffmann G, Heckman TM, White SDM, et al. 2003. *MNRAS* 341:54–69
- Kauffmann G, White SDM, Heckman TM, et al. 2004. *MNRAS* 353:713–731
- Kaviraj S, Schawinski K, Devriendt JEG, et al. 2007. *Ap. J. Suppl.* 173:619–642
- Kereš D, Katz N, Weinberg DH, Davé R. 2005. *MNRAS* 363:2–28

- Khochfar S, Burkert A. 2006. *Astron. Astrophys.* 445:403–412
 Khochfar S, Emsellem E, Serra P, et al. 2011. *MNRAS* 417:845
 Khochfar S, Silk J. 2006. *Ap. J. Let.* 648:L21–L24
 Koekemoer AM, Faber SM, Ferguson HC, et al. 2011. *Ap. J. Suppl.* 197:36
 Koopmans LVE, Bolton A, Treu T, et al. 2009. *Ap. J. Let.* 703:L51–L54
 Kormendy J. 1977. *Ap. J.* 218:333–346
 Kormendy J. 1982a. In *Morphology and Dynamics of Galaxies, 12th Advanced Course of the Swiss Society of Astronomy and Astrophysics*, eds. L Martinet, M Mayor, 113–288. Sauverny: Geneva Obs.
 Kormendy J. 1982b. *Ap. J.* 257:75–88
 Kormendy J. 1985. *Ap. J.* 295:73–79
 Kormendy J. 2016. In *Galactic Bulges*, eds. E Laurikainen, R Peletier, D Gadotti, 431. Berlin: Springer
 Kormendy J, Bender R. 1996. *Ap. J. Let.* 464:L119
 Kormendy J, Bender R. 2012. *Ap. J. Suppl.* 198:2
 Kormendy J, Djorgovski S. 1989. *Annu. Rev. Astron. Astrophys.* 27:235–277
 Kormendy J, Fisher DB, Cornell ME, Bender R. 2009. *Ap. J. Suppl.* 182:216–309
 Kormendy J, Ho LC. 2013. *Annu. Rev. Astron. Astrophys.* 51:511–653
 Kormendy J, Illingworth G. 1982. *Ap. J.* 256:460–480
 Krajnović D, Alatalo K, Blitz L, et al. 2013a. *MNRAS* 432:1768–1795
 Krajnović D, Bacon R, Cappellari M, et al. 2008. *MNRAS* 390:93–117
 Krajnović D, Cappellari M, de Zeeuw PT, Copin Y. 2006. *MNRAS* 366:787–802
 Krajnović D, Cappellari M, Emsellem E, McDermid RM, de Zeeuw PT. 2005. *MNRAS* 357:1113–1133
 Krajnović D, Emsellem E, Cappellari M, et al. 2011. *MNRAS* 414:2923–2949
 Krajnović D, Karick AM, Davies RL, et al. 2013b. *MNRAS* 433:2812–2839
 Krajnović D, Weilbacher PM, Urrutia T, et al. 2015. *MNRAS* 452:2–18
 Kroupa P. 2001. *MNRAS* 322:231–246
 Kuntschner H, Emsellem E, Bacon R, et al. 2010. *MNRAS* 408:97–132
 La Barbera F, Ferreras I, Vazdekis A. 2015. *MNRAS* 449:L137–L141
 Lablanche PY, Cappellari M, Emsellem E, et al. 2012. *MNRAS* 424:1495
 Lambas DG, Maddox SJ, Loveday J. 1992. *MNRAS* 258:404–414
 Läsker R, van den Bosch RCE, van de Ven G, et al. 2013. *MNRAS* 434:L31–L35
 Lauer TR. 2012. *Ap. J.* 759:64
 Lauer TR, Ajhar EA, Byun YI, et al. 1995. *Astron. J.* 110:2622
 Lauer TR, Faber SM, Gebhardt K, et al. 2005. *Astron. J.* 129:2138–2185
 Lauer TR, Faber SM, Richstone D, et al. 2007a. *Ap. J.* 662:808–834
 Lauer TR, Gebhardt K, Faber SM, et al. 2007b. *Ap. J.* 664:226–256
 Lauer TR, Postman M, Strauss MA, Graves GJ, Chisari NE. 2014. *Ap. J.* 797:82
 Laurikainen E, Salo H, Buta R, Knapen JH, Comerón S. 2010. *MNRAS* 405:1089–1118
 Law DR, Shapley AE, Steidel CC, et al. 2012. *Nature* 487:338–340
 Leauthaud A, Tinker J, Bundy K, et al. 2012. *Ap. J.* 744:159
 Li H, Li R, Mao S, et al. 2016. *MNRAS* 455:3680–3692
 Liu FS, Mao S, Meng XM. 2012. *MNRAS* 423:422–436
 Lokas EL, Mamon GA. 2003. *MNRAS* 343:401–412
 Longhetti M, Saracco P, Severgnini P, et al. 2007. *MNRAS* 374:614–626
 Ma CP, Greene JE, McConnell N, et al. 2014. *Ap. J.* 795:158
 Magorrian J, Tremaine S, Richstone D, et al. 1998. *Astron. J.* 115:2285–2305
 Magoulas C, Springob CM, Colless M, et al. 2012. *MNRAS* 427:245–273
 Maltby DT, Aragón-Salamanca A, Gray ME, et al. 2010. *MNRAS* 402:282–294
 Maraston C, Strömbäck G. 2011. *MNRAS* 418:2785–2811

- Marconi A, Hunt LK. 2003. *Ap. J. Let.* 589:L21–L24
- Martig M, Bournaud F, Teyssier R, Dekel A. 2009. *Ap. J.* 707:250–267
- Martig M, Crocker AF, Bournaud F, et al. 2013. *MNRAS* 432:1914–1927
- Martin-Navarro I, Pérez-González PG, Trujillo I, et al. 2015a. *Ap. J. Let.* 798:L4
- Martin-Navarro I, Vazdekis A, La Barbera F, et al. 2015b. *Ap. J. Let.* 806:L31
- Masters KL, Mosleh M, et al. 2010. *MNRAS* 405:783–799
- Matković A, Guzmán R. 2005. *MNRAS* 362:289–300
- McConnell NJ, Ma CP, Gebhardt K, et al. 2011. *Nature* 480:215–218
- McDermid RM, Alatalo K, Blitz L, et al. 2015. *MNRAS* 448:3484–3513
- McDermid RM, Cappellari M, Alatalo K, et al. 2014. *Ap. J. Let.* 792:L37
- McDermid RM, Emsellem E, Shapiro KL, et al. 2006. *MNRAS* 373:906–958
- McLaughlin DE. 1999. *Ap. J. Let.* 512:L9–L12
- Melnick J, Sargent WLW. 1977. *Ap. J.* 215:401–407
- Mihos JC, Hernquist L. 1994. *Ap. J. Let.* 431:L9–L12
- Milosavljević M, Merritt D. 2001. *Ap. J.* 563:34–62
- Misgeld I, Hilker M. 2011. *MNRAS* 414:3699–3710
- Mo H, van den Bosch FC, White S. 2010. *Galaxy Formation and Evolution*. Cambridge, UK: Cambridge University Press
- Monnet G, Bacon R, Emsellem E. 1992. *Astron. Astrophys.* 253:366–373
- Moore B, Katz N, Lake G, Dressler A, Oemler A. 1996. *Nature* 379:613–616
- Moran SM, Ellis RS, Treu T, et al. 2007. *Ap. J.* 671:1503–1522
- Morganti L, Gerhard O, Coccato L, Martínez-Valpuesta I, Arnaboldi M. 2013. *MNRAS* 431:3570–3588
- Morganti R, de Zeeuw PT, et al. 2006. *MNRAS* 371:157–169
- Moster BP, Naab T, White SDM. 2013. *MNRAS* 428:3121–3138
- Moster BP, Somerville RS, Maulbetsch C, et al. 2010. *Ap. J.* 710:903–923
- Murphy JD, Gebhardt K, Adams JJ. 2011. *Ap. J.* 729:129
- Muzzin A, Marchesini D, Stefanon M, et al. 2013. *Ap. J.* 777:18
- Naab T, Burkert A. 2003. *Ap. J.* 597:893–906
- Naab T, Johansson PH, Ostriker JP. 2009. *Ap. J. Let.* 699:L178–L182
- Naab T, Oser L, Emsellem E, et al. 2014. *MNRAS* 444:3357–3387
- Napolitano NR, Pota V, Romanowsky AJ, et al. 2014. *MNRAS* 439:659–672
- Napolitano NR, Romanowsky AJ, Capaccioli M, et al. 2011. *MNRAS* 411:2035–2053
- Navarro JF, Frenk CS, White SDM. 1996. *Ap. J.* 462:563–575
- Newman AB, Ellis RS, Bundy K, Treu T. 2012. *Ap. J.* 746:162
- Newman AB, Ellis RS, Treu T. 2015. *Ap. J.* 814:26
- Newman AB, Treu T, Ellis RS, et al. 2013a. *Ap. J.* 765:24
- Newman JA, Cooper MC, Davis M, et al. 2013b. *Ap. J. Suppl.* 208:5
- Nipoti C, Londrillo P, Ciotti L. 2003. *MNRAS* 342:501–512
- Norris MA, Kannappan SJ, Forbes DA, et al. 2014. *MNRAS* 443:1151–1172
- Ocvirk P, Pichon C, Lançon A, Thiébaut E. 2006. *MNRAS* 365:74–84
- Oemler Jr. A. 1974. *Ap. J.* 194:1–20
- Onodera M, Daddi E, Gobat R, et al. 2010. *Ap. J. Let.* 715:L6–L11
- Oosterloo T, Morganti R, et al. 2010. *MNRAS* 409:500–514
- Oser L, Naab T, Ostriker JP, Johansson PH. 2012. *Ap. J.* 744:63
- Padilla ND, Strauss MA. 2008. *MNRAS* 388:1321–1334
- Pahre MA, Djorgovski SG, de Carvalho RR. 1998. *Astron. J.* 116:1591–1605
- Paturel G, Petit C, Prugniel P, et al. 2003. *Astron. Astrophys.* 412:45–55
- Peletier RF, Davies RL, Illingworth GD, Davis LE, Dawson M. 1990. *Astron. J.* 100:1091–1142
- Peng YJ, Lilly SJ, Kovač K, et al. 2010. *Ap. J.* 721:193–221
- Pinkney J, Gebhardt K, Bender R, et al. 2003. *Ap. J.* 596:903–929

- Poggianti BM, Calvi R, Bindoni D, et al. 2013. *Ap. J.* 762:77
- Poggianti BM, Desai V, Finn R, et al. 2008. *Ap. J.* 684:888–904
- Porter LA, Somerville RS, Primack JR, Johansson PH. 2014. *MNRAS* 444:942–960
- Posacki S, Cappellari M, Treu T, Pellegrini S, Ciotti L. 2015. *MNRAS* 446:493–509
- Postman M, Franx M, Cross NJG, et al. 2005. *Ap. J.* 623:721–741
- Postman M, Geller MJ. 1984. *Ap. J.* 281:95–99
- Prugniel P, Simien F. 1996. *Astron. Astrophys.* 309:749–759
- Prugniel P, Simien F. 1997. *Astron. Astrophys.* 321:111–122
- Querejeta M, Eliche-Moral MC, Tapia T, et al. 2015. *Astron. Astrophys.* 579:L2
- Raskutti S, Greene JE, Murphy JD. 2014. *Ap. J.* 786:23
- Remus RS, Burkert A, Dolag K, et al. 2013. *Ap. J.* 766:71
- Renzini A. 2006. *Annu. Rev. Astron. Astrophys.* 44:141–192
- Renzini A, Ciotti L. 1993. *Ap. J. Let.* 416:L49
- Richstone DO, Tremaine S. 1988. *Ap. J.* 327:82–88
- Rix H, Franx M, Fisher D, Illingworth G. 1992. *Ap. J. Let.* 400:L5–L8
- Rix HW, de Zeeuw PT, Cretton N, van der Marel RP, Carollo CM. 1997. *Ap. J.* 488:702
- Robertson B, Bullock JS, Cox TJ, et al. 2006. *Ap. J.* 645:986–1000
- Romanowsky AJ, Douglas NG, Arnaboldi M, et al. 2003. *Science* 301:1696–1698
- Romanowsky AJ, Kochanek CS. 1997. *MNRAS* 287:35–50
- Rousseeuw P, Van Driesssen K. 2006. *Data Mining and Knowledge Discovery* 12:29–45
- Rubin VC, Ford Jr. WK. 1970. *Ap. J.* 159:379
- Rubin VC, Ford WJK, Thonnard N. 1980. *Ap. J.* 238:471–487
- Rubin VC, Graham JA, Kenney JDP. 1992. *Ap. J. Let.* 394:L9–L12
- Rusli SP, Thomas J, Saglia RP, et al. 2013. *Astron. J.* 146:45
- Rybicki GB. 1987. In *Structure and Dynamics of Elliptical Galaxies*, ed. PT de Zeeuw, 397. vol. 127 of *IAU Symposium*, Dordrecht: D. Reidel
- Ryden B. 1992. *Ap. J.* 396:445–452
- Ryś A, van de Ven G, Falcón-Barroso J. 2014. *MNRAS* 439:284–299
- Saintonge A, Tacconi LJ, Fabello S, et al. 2012. *Ap. J.* 758:73
- Salim S, Rich RM, Charlot S, et al. 2007. *Ap. J. Suppl.* 173:267–292
- Salpeter EE. 1955. *Ap. J.* 121:161–167
- Sánchez SF, Kennicutt RC, Gil de Paz A, et al. 2012. *Astron. Astrophys.* 538:A8
- Sandage A. 1961. *The Hubble Atlas*. Washington, D.C.: Carnegie Institution of Washington
- Sandage A. 1975. In *Galaxies and the Universe*, eds. A Sandage, M Sandage, J Kristian, 1. Chicago, IL: the University of Chicago Press
- Sandage A. 2005. *Annu. Rev. Astron. Astrophys.* 43:581–624
- Sandage A, Freeman KC, Stokes NR. 1970. *Ap. J.* 160:831
- Sandage A, Hardy E. 1973. *Ap. J.* 183:743–758
- Sarzi M, Alatalo K, Blitz L, et al. 2013. *MNRAS* 432:1845–1861
- Sarzi M, Falcón-Barroso J, Davies RL, et al. 2006. *MNRAS* 366:1151–1200
- Sarzi M, Ledo HR, Dotti M. 2015. *MNRAS* 453:1070–1078
- Schechter P. 1976. *Ap. J.* 203:297
- Schechter PL, Gunn JE. 1979. *Ap. J.* 229:472–484
- Schoenmakers RHM, Franx M, de Zeeuw PT. 1997. *MNRAS* 292:349
- Schwarzschild M. 1979. *Ap. J.* 232:236–247
- Scodéglio M, Gavazzi G, Belsole E, Pierini D, Boselli A. 1998. *MNRAS* 301:1001–1018
- Scott N, Cappellari M, Davies RL, et al. 2009. *MNRAS* 398:1835–1857
- Scott N, Cappellari M, Davies RL, et al. 2013a. *MNRAS* 432:1894–1913
- Scott N, Davies RL, Houghton RCW, et al. 2014. *MNRAS* 441:274–288
- Scott N, Fogarty LMR, Owers MS, et al. 2015. *MNRAS* 451:2723–2734
- Scott N, Graham AW, Schombert J. 2013b. *Ap. J.* 768:76

- Scoville N, Abraham RG, Aussel H, et al. 2007. *Ap. J. Suppl.* 172:38–45
- Serra P, Oosterloo T, Morganti R, et al. 2012. *MNRAS* 422:1835–1862
- Sersic JL. 1968. *Atlas de galaxias australes*. Córdoba: Obs. Astron. Univ. Nacional de Córdoba
- Shen S, Mo HJ, White SDM, et al. 2003. *MNRAS* 343:978–994
- Shetty S, Cappellari M. 2014. *Ap. J. Let.* 786:L10
- Sil’chenko OK. 1999. *Astron. J.* 117:2725–2735
- Sil’chenko OK, Vlasyuk VV, Burenkov AN. 1997. *Astron. Astrophys.* 326:941–949
- Silk J, Rees MJ. 1998. *Astron. Astrophys.* 331:L1–L4
- Simien F, de Vaucouleurs G. 1986. *Ap. J.* 302:564–578
- Skibba RA, Bamford SP, et al. 2009. *MNRAS* 399:966–982
- Skrutskie MF, Cutri RM, Stiening R, et al. 2006. *Astron. J.* 131:1163–1183
- Smith GP, Treu T, Ellis RS, Moran SM, Dressler A. 2005. *Ap. J.* 620:78–87
- Smith RJ. 2014. *MNRAS* 443:L69–L73
- Smith RJ, Lucey JR, Carter D. 2012a. *MNRAS* 426:2994–3007
- Smith RJ, Lucey JR, Price J, Hudson MJ, Phillipps S. 2012b. *MNRAS* 419:3167–3180
- Somerville RS, Davé R. 2015. *Annu. Rev. Astron. Astrophys.* 53:51–113
- Sonnenfeld A, Treu T, Marshall PJ, et al. 2015. *Ap. J.* 800:94
- Spinelli C, Trager SC, Koopmans LVE. 2015. *Ap. J.* 803:87
- Spinelli C, Trager SC, Koopmans LVE, Chen YP. 2012. *Ap. J. Let.* 753:L32
- Spolaor M, Proctor RN, Forbes DA, Couch WJ. 2009. *Ap. J. Let.* 691:L138–L141
- Springel V, White SDM, Jenkins A, et al. 2005. *Nature* 435:629–636
- Springob CM, Magoulas C, Proctor R, et al. 2012. *MNRAS* 420:2773–2784
- Stanford SA, Eisenhardt PR, Dickinson M. 1998. *Ap. J.* 492:461
- Stark AA. 1977. *Ap. J.* 213:368–373
- Statler TS. 1987. *Ap. J.* 321:113–152
- Stott JP, Swinbank AM, Johnson HL, et al. 2016. *MNRAS* 457:1888–1904
- Strateva I, Ivezić Ž, Knapp GR, et al. 2001. *Astron. J.* 122:1861–1874
- Syer D, Tremaine S. 1996. *MNRAS* 282:223–233
- Tacconi LJ, Genzel R, Neri R, et al. 2010. *Nature* 463:781–784
- Tasca LAM, Kneib J, Iovino A, et al. 2009. *Astron. Astrophys.* 503:379–398
- Thomas D, Maraston C, Bender R, Mendes de Oliveira C. 2005. *Ap. J.* 621:673–694
- Thomas J, Jesseit R, Saglia RP, et al. 2009. *MNRAS* 393:641–652
- Thomas J, Saglia RP, Bender R, et al. 2011. *MNRAS* 415:545–562
- Toft S, Gallazzi A, Zirm A, et al. 2012. *Ap. J.* 754:3
- Toft S, van Dokkum P, Franx M, et al. 2007. *Ap. J.* 671:285–302
- Tojeiro R, Heavens AF, Jimenez R, Panter B. 2007. *MNRAS* 381:1252–1266
- Tortora C, La Barbera F, Napolitano NR, de Carvalho RR, Romanowsky AJ. 2012. *MNRAS* 425:577–594
- Tortora C, Napolitano NR, Romanowsky AJ, Capaccioli M, Covone G. 2009. *MNRAS* 396:1132–1150
- Tortora C, Romanowsky AJ, Napolitano NR. 2013. *Ap. J.* 765:8
- Tremblay B, Merritt D. 1996. *Astron. J.* 111:2243
- Treu T, Auger MW, Koopmans LVE, et al. 2010. *Ap. J.* 709:1195–1202
- Treu T, Ellis RS, Kneib J, et al. 2003. *Ap. J.* 591:53–78
- Trujillo I, Burkert A, Bell EF. 2004a. *Ap. J. Let.* 600:L39–L42
- Trujillo I, Conselice CJ, Bundy K, et al. 2007. *MNRAS* 382:109–120
- Trujillo I, Erwin P, Asensio Ramos A, Graham AW. 2004b. *Astron. J.* 127:1917–1942
- Trujillo I, Feulner G, Goranova Y, et al. 2006a. *MNRAS* 373:L36–L40
- Trujillo I, Förster Schreiber NM, Rudnick G, et al. 2006b. *Ap. J.* 650:18–41
- Valluri M, Ferrarese L, Merritt D, Joseph CL. 2005. *Ap. J.* 628:137–152
- Valluri M, Merritt D, Emsellem E. 2004. *Ap. J.* 602:66–92

- van de Sande J, Kriek M, Franx M, et al. 2011. *Ap. J. Let.* 736:L9
- van de Sande J, Kriek M, Franx M, et al. 2013. *Ap. J.* 771:85
- van den Bergh S. 1976. *Ap. J.* 206:883–887
- van den Bergh S. 2007. *Astron. J.* 134:1508
- van den Bosch FC. 1997. *MNRAS* 287:543–555
- van den Bosch RCE, Gebhardt K, Gültekin K, et al. 2012. *Nature* 491:729–731
- van den Bosch RCE, van de Ven G. 2009. *MNRAS* 398:1117–1128
- van den Bosch RCE, van de Ven G, Verolme EK, Cappellari M, de Zeeuw PT. 2008. *MNRAS* 385:647–666
- van der Marel RP. 1991. *MNRAS* 253:710–726
- van der Marel RP, Cretton N, de Zeeuw PT, Rix HW. 1998. *Ap. J.* 493:613
- van der Marel RP, van Dokkum PG. 2007. *Ap. J.* 668:756–771
- van der Wel A, Franx M, van Dokkum PG, et al. 2014. *Ap. J.* 788:28
- van Dokkum PG, Conroy C. 2010. *Nature* 468:940–942
- van Dokkum PG, Conroy C. 2012. *Ap. J.* 760:70
- van Dokkum PG, Fabricant D, Illingworth GD, Kelson DD. 2000. *Ap. J.* 541:95–111
- van Dokkum PG, Franx M, Kriek M, et al. 2008. *Ap. J. Let.* 677:L5–L8
- van Dokkum PG, Leja J, Nelson EJ, et al. 2013. *Ap. J. Let.* 771:L35
- van Dokkum PG, Nelson EJ, Franx M, et al. 2015. *Ap. J.* 813:23
- van Dokkum PG, Whitaker KE, Brammer G, et al. 2010. *Ap. J.* 709:1018–1041
- Vazdekis A, Ricciardelli E, Cenarro AJ, et al. 2012. *MNRAS* 424:157–171
- Walcher CJ, Wisotzki L, Bekeraïté S, et al. 2014. *Astron. Astrophys.* 569:A1
- Weijmans AM, Cappellari M, Bacon R, et al. 2009. *MNRAS* 398:561–574
- Weijmans AM, de Zeeuw PT, Emsellem E, et al. 2014. *MNRAS* 444:3340–3356
- Weijmans AM, Krajnović D, van de Ven G, et al. 2008. *MNRAS* 383:1343–1358
- White SDM. 1983. In *Internal Kinematics and Dynamics of Galaxies*, ed. E Athanassoula, 337–344. vol. 100 of *IAU Symposium*
- White SDM, Rees MJ. 1978. *MNRAS* 183:341–358
- Wilkinson A, Sharples RM, Fosbury RAE, Wallace PT. 1986. *MNRAS* 218:297–329
- Wilkinson DM, Maraston C, Thomas D, et al. 2015. *MNRAS* 449:328–360
- Wilman DJ, Erwin P. 2012. *Ap. J.* 746:160
- Wilman DJ, Oemler A, Mulchaey JS, et al. 2009. *Ap. J.* 692:298–308
- Wisnioski E, Förster Schreiber NM, Wuyts S, et al. 2015. *Ap. J.* 799:209
- Wolf C, Aragón-Salamanca A, Balogh M, et al. 2009. *MNRAS* 393:1302–1323
- Yıldırım A, van den Bosch RCE, van de Ven G, et al. 2015. *MNRAS* 452:1792–1816
- Young CK, Currie MJ. 1994. *MNRAS* 268:L11
- Young LM, Bureau M, Cappellari M. 2008. *Ap. J.* 676:317–334
- Young LM, Bureau M, Davis TA, et al. 2011. *MNRAS* 414:940
- Young LM, Scott N, Serra P, et al. 2014. *MNRAS* 444:3408–3426
- Zehavi I, Zheng Z, Weinberg DH, et al. 2005. *Ap. J.* 630:1–27
- Zheng Z, Berlind AA, Weinberg DH, et al. 2005. *Ap. J.* 633:791–809
- Zirm AW, van der Wel A, Franx M, et al. 2007. *Ap. J.* 656:66–72